SISSA

Scuola
Internazionale
Superiore di
Studi Avanzati

Engineering neuronal networks with nanomaterials: graphene shaping of synaptic activity

CANDIDATE

Nicola Secomandi

SUPERVISOR

Laura Ballerini

CONTENTS

ABSTRACT

Graphene is a single atomic plane material consisting of sp^2-hybridized carbon atoms with a hexagonal structural organization and characterized by unique properties such as high electrical conductivity, mechanical flexibility and optical transparency. Due to their peculiar features, graphene and its derivates have attracted an increasing interest for biomedical applications including drug and gene delivery, imaging and diagnostic or tissue engineering. However, using graphene-based nanomaterials (GBNs) in modern medicine, in particular neurology, needs a greater and deeper understanding of the cell-nanomaterial interactions. In this framework we focus on studying the impact of GBNs on the neuronal network and their ability in shaping synaptic transmission.

First, we exploited 3D elastomeric scaffolds enriched with graphene to better understand the effects of this nanomaterial on the neural activity when interfacing neurons and synapses in the third dimension. Our results, using imaging techniques, show the ability of graphene to modulate the neuronal network formation in a 3D environment which might be due to modulations in the excitatory/inhibitory ratio.

Afterwards we investigated the interactions between graphene oxide flakes with small lateral size (s-GO) and isolated amygdala neurons and synapses. Thus, we developed and characterized an *in vitro* model of amygdala network using immunofluorescence and electrophysiological techniques. When we acutely applied s-GO to these cultures, the nanomaterial was capable to selectively alter the glutamatergic excitatory activity. This peculiar interaction may be taken into account for exploiting s-GO as a novel tool to target central nervous system (CNS) synapses.

INTRODUCTION

1. Nanotechnology, Nanomaterials and Biology

NANOTECHNOLOGY. The term "nanotechnology" was adopted the first time, within a scientific publication, by Norio Taniguchi in 1974. Today we refer to nanotechnology as technology and science that work with engineered devices or nanomaterials which have a functional organization on the nanometer scale, normally from 1 to 100 nm, at least in one dimension (Silva, 2006). Since most of biological entities and cellular components are in the sub-micrometric and nanometric range, nanotechnology has been more and more used in biomedical issues (Fig.1); in fact, for example, the diameter of the DNA double helix is around 2 nm, hemoglobin's diameter is around 5 nm and lipid bilayer surrounding cells has a thickness between 6 and 10 nm. The application of nanotechnology into biology and medicine is called bionanotechnology or nanobiotechnology.

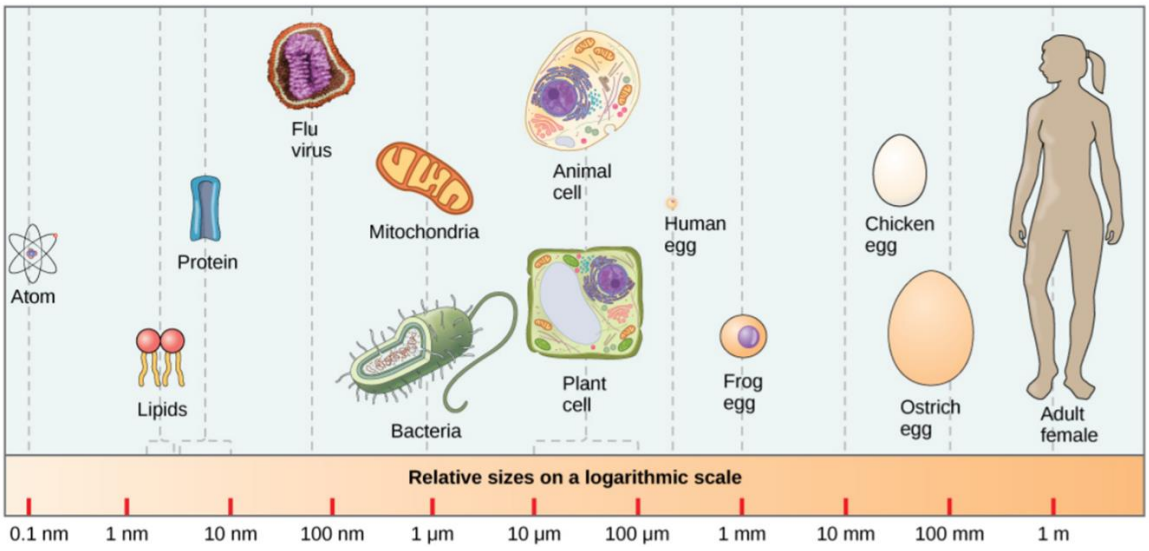

Figure 1. *Relative sizes of different cells and biological components. Notice that several cell elements show nanometric and micrometric dimensions.*

NANOMATERIALS are described as low-dimensional structures with at least one dimension <100 nm (Biswas and Wu, 2005). Due to their unique electronic, optical and mechanical features, nanomaterials are nowadays more and more used in several application fields like electronics (Kang et al., 2015) , cosmetic (Borowska and Brzóska, 2015; Patil et al., 2015) and medicine (Chen et al., 2013; Oyefusi et al., 2014; Simões et al., 2015). Moreover, nanomaterials present high surface area to volume ratio, site-specific delivery or targeting

and flexibility in allowing surface functionalization (Garbayo et al., 2014; Kumar et al., 2017). In medicine, for instance, functionalized nanoparticles like nanoliposomes can be used for drug delivery (Kumar et al., 2017; Maurer et al., 2001). Nanoparticles offer the ability to pass biological barriers, such as the blood-brain or intestinal barriers (Lockman et al., 2003; Russell-Jones, 1999; Vinogradov et al., 2004), reach their designed target and act as therapeutic and imaging agents. The ability to engineer nanomaterials to reach targeted therapy is probably one of the most important features of nanotechnology. Also in neuroscience, the improvement in designing and synthesizing nanomaterials has been used in basic and applied research (Giugliano et al., 2008; Veloz-Castillo et al., 2016).

2. Carbon-Based Nanomaterials and Biomedical Applications

2.1 Carbon-Based Nanomaterials (CBNs): General Features

In the periodic table, carbon is one of the most abundant and versatile elements; it forms different compounds that present completely distinct properties depending on the variety of its allotropes and structures. In fact, the valence orbitals of Carbon are able to hybridize in three different configurations: sp, sp^2 and sp^3. Moreover, a full range of dimensionally different allotropes can be obtained from Carbon; depending on its hybridization it is possible to have stable structure like nano-sized balls, 0 dimensions (0D), long thin tubes, 1 dimension (1D), single layers, 2 dimensions (2D) and crystal, 3 dimensions (3D) (Fig.2).

Diamond and graphite are common examples, with amorphous carbon, of naturally occurring carbon allotropes, while carbon nanotubes, fullerenes, nanodiamonds and graphene are obtained from synesthetic process. Diamond for example, is characterized by carbon atoms hybridized purely in sp^3 configurations whereas in graphite the hybridization is sp^2. Synthetic carbon-based materials like carbon nanotubes or graphene, present carbon atoms hybridized with sp^2 bonds. In this last case, the fourth electron in p_z orbital, which is not taking part in the sp^2 hybridization, will form a delocalized π bond able to move between carbon atoms. This free electron led to one of the most important hallmarks of these materials, the high electrical conductivity (Littlejohn, 2014).

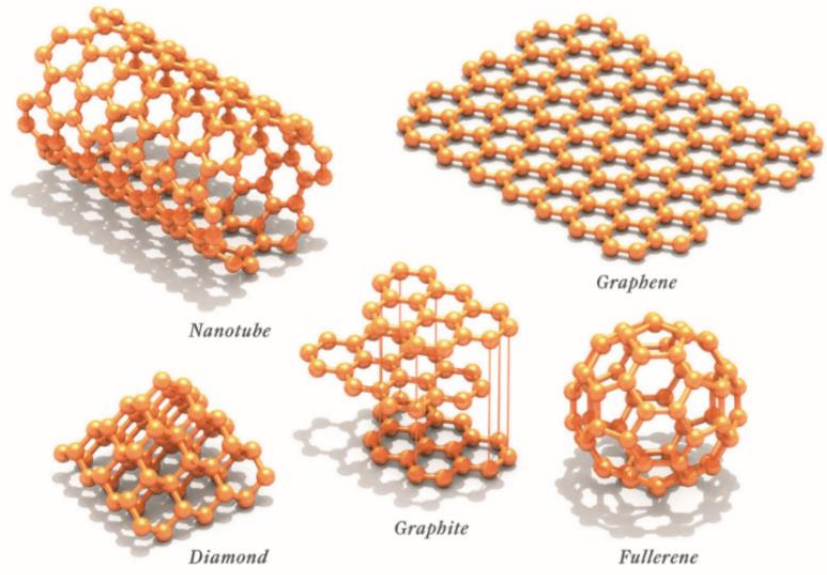

Figure 2. *Five types of carbons allotropes. Fullerene (0D), carbon nanotube (1D), graphene (2D) and (3D) graphite. All are sp^2 hybridized but diamond (sp^3) (from Sinitskii and Tour, 2010).*

FULLERENE was discovered in 1985 by H. W. Kroto and colleagues. The most common fullerene presents an icosahedral and symmetrical structure, which is composed of 20 hexagons and 12 pentagons where every carbon atom is linked to other three with sp^2 hybridization (Kroto et al., 1985). This compound is characterized by 60 carbon atoms (C60) are arranged in soccer ball shape. Fullerenes are considered zero-dimensional (0D) carbon materials, which exhibit very interesting chemical and physical features (Gaudiana and Brabec, 2008; Guldi and Prato, 2000; Jensen et al., 1996; Kirner et al., 2014). Fullerene presents excellent mechanical features, it is able to resist high pressures and then return to its original shape; these hallmarks make this carbon-based material harder than others, such as steal and diamond. Moreover, fullerene is characterized by notable optical properties and high electron affinity. (Dresselhaus et al., 1996; Ruoff and Ruoff, 1991; Thompson and Fréchet, 2008).

CARBON NANOTUBES (CNTs) are one of the most studied nanostructures in the latest decades (Li et al., 2015b). Described by S. Iijima in 1991 (Iijima, 1991), they are nano-objects obtained from a graphene sheet rolled in a cylindrical structure, where the length/diameter ratio makes CNTs a 1-dimensional object (Iijima, 1991; Iijima and Ichihashi, 1993). Single-walled CNTs (SWCNTs) and multi-walled CNTs (MWCNTs) are the two most important and used forms in biomedical applications; the first presents a single cylinder structure while the second consists of different concentric SWCNTs. Since their features are depending on length, diameter and morphology of the carbon tube, but also on how the graphene sheet is twisted, SWCNTs and MWCNTs display different properties (Charlier, 2002; Gooding, 2005; Thostenson et al., 2001). CNTs present remarkable properties, such as high mechanical strength and elasticity, great thermal, chemical and structural stability, high electrical conductivity and high surface area (Ajayan, 1999; Katz and Willner, 2004); due to these, CNTs are among the most studied carbon based material in several fields.

CARBON QUANTUM DOTS (CQDs, C-dots or CDs), called also fluorescent carbon nanoparticles, were first accidentally discovered in 2004 by Xu and collaborators in the course of SWCNTs purification (Xu et al., 2004). They are described as small nanoparticles characterized by excellent properties like high conductivity and chemical stability, low toxicity and in particular a very strong photoluminescence emission and optical features. Components and structure of CDs define their distinct characteristics (Lim et al., 2015) and, moreover, they can be functionalized with different organic, inorganic or biological

materials. Due to their properties, these nanoparticles have been used to develop solid-state nanostructured solar cells (Briscoe et al., 2015) , in photocatalytic energy conversion (Fernando et al., 2015), in sensing applications (Zhao et al., 2015) but also in bioimaging applications due to their great intrinsic fluorescence, from the visible up to the neat infrared (IR) (Li et al., 2012; Strauss et al., 2014).

NANODIAMONDS (NDs). Diamond is a metastable carbon allotrope where the atoms are organized in a variation of the face-centered cubic crystal structure (Shao et al., 2004) and, it is known to be characterized by the greatest hardness and thermal conductivity for any material. Said that, nanodiamonds are nanoscale-level size diamonds that were described during 1960s. Structures of NDs are very complex; in fact, they present an amorphous carbon shell and a diamond core where the average size of particles are around 4-5 nm (Aleksenskii et al., 1999). Different techniques have been used to synthesize nanodiamonds like detonation (Yeap et al., 2008) or ion irradiation of graphite (Daulton et al., 2001). Among all the properties, NDs are defined by high hardness, reflection index and thermal conductivity, they also present great stability at room temperature and an extremely high resistivity (Zhang et al., 2018).

2.2 Biological Interaction of Carbon-Based Nanomaterials

BIOCOMPATIBILITY of CBNs. In recent years, carbon-based nanomaterials have been attracting significant attention in nanomedicine due to their unique mechanical, electronic, thermal and optical properties (Chen et al., 2015; Mundra et al., 2014). For example, CNTs present great optical absorption in the near IR and photo acoustic properties, which allow CNTs to be potentially used in *in vivo* applications with a bio-imaging and tracing function coupled with drug delivery, or like nanodiamonds or fullerenes, which in the last few years, have been used in the cancer medicine area (Chen et al., 2015). However, before describing the biomedical application of CBNs, it is important to take into account their toxicity.

The first thing to underline is that graphene or CNTs, for example, are not single nanomaterials but groups, family of nanomaterials, which possess significant differences in terms of their chemical and physical features, like purity or surface functionalization, but also in their safety/toxicity profile; because of this, generalizations and categorizations about the toxicity of carbon-based materials must be avoided. For biocompatibility evaluation of carbon-based materials it is extremely important to assess their potential effect on the

immune system (Farrera and Fadeel, 2015). In fact, this specialized system is extremely important to protect us from pathogens and other external intrusion.

Mainly for CNTs, due to their great potential in biomedical applications, a large number of studies were performed to evaluate their effect on the immunity. For example, Pescatori and colleagues, reported that functionalized MWCNTs, after have being internalized and assessed the lack of toxicity in cell lines, were able to activate immune-related pathways in monocytes demonstrating that CBN may behave like specific cell immunostimulatory agents, opening great future perspectives for their application also as immunotherapeutic agents (Pescatori et al., 2013). It has been described that surface functionalization of CBNs such as CNTs and carbon nano-onions, led to a reduction of their inflammatory response, with an attenuation of innate immune system recruitment (Yang et al., 2013b). Nevertheless, the CBNs and the immune system interaction may be also reciprocal, meaning that the immune cells can react to nanomaterials and degrade them (Bhattacharya et al., 2013).

BIOMEDICAL APPLICATIONS of CBNs. As stated above, carbon-based nanomaterials are characterized by excellent physical and chemical features that make them extremely useful and attractive in biomedicine, for diagnostic and therapeutic applications, as well as in regenerative medicine.

In novel therapeutic developments, these materials may be exploited as gene or drug delivery carriers. Among CBNs for drug vehicle, CNTs are the most studied. For this aim, drugs can be inserted into CNTs using non-covalent interactions, like for examples π-π bonds as shown for doxorubicin, a chemotherapy drug (Chen et al., 2015), while for hydrophilic drugs also covalent binding have been reported (Bhirde et al., 2009). CNTs can be used for gene or, more recently, small interfering RNA (siRNA) delivery (Al-Jamal et al., 2011) (Sacchetti et al., 2014), since CNTs are known to interact with DNA. Kostarelos and collaborators have supported a passive “nanosyringe-like” mechanism that can allow CNTs to permeate through the plasma membrane. The latter, if confirmed to be specific for the target cells, can be utilized for gene delivery (Kostarelos et al., 2007). In this context, since lipids, proteins or other biomolecules present in the biological environment, may rapidly coat the nanomaterial’s surface (so-called bio-corona formation), the potential impact of this corona on target recognition and uptake is a matter of debate (Docter et al., 2015).

Other CBNs which have been studied as drug and gene delivery vehicles are fullerenes, particularly C60 (Dellinger et al., 2013). For example, Maeda-Mamiya and collaborators showed for the first time an effective gene delivery using a water-soluble fullerene *in vivo* (Maeda-Mamiya et al., 2010). These carbon materials, in addiction of being studied as vehicle, are nanoparticles that might be used as theragnostic tools *per se*. In particular, the metallofullerene nanoparticles are fullerene derivatives composed by a metal atom within a fullerene cage lately tested because of their peculiar mechanical and electrochemical features. Gadolinium (Gd)-based metallofullerenes are among them and have been proposed as new contrast agents and may also work like anti-cancer agents (Lu et al., 2012). Indeed, it has been showed that Cd-metallofullerenes are able to inhibit pancreatic tumor metastasis (Balogh, 2015; Kang et al., 2012; Pan et al., 2015).

Moreover, nanodiamonds were recently proposed as new approaches able to bypass chemoresistance for metastatic cancer treatments; in fact, as reported by Chow and colleagues, nanodiamond-doxorubicin complex significantly enhances therapeutic response and reduces chemoresistance in mammary and liver cancer mouse models (Chow et al., 2011).

Another nanomedicine area, where CBNs received attention, is imaging and diagnostics. Also in this field CNTs are studied for multiple imaging modalities like Raman imaging, photoacoustic and fluorescence imaging and many others (De La Zerda et al., 2008; Delogu et al., 2012; Ghosh et al., 2014).

C60 fullerenes, functionalized with metals, have been used as radiotracers and contrast agents, like for example metallofullerenes have been investigated for magnetic resonance imaging (MRI) for more than 10 years (Lu et al., 2012). Today CBNs have been used also to develop multi-functional theragnostic devices, where diagnostic and therapeutic modalities are combined (Chen et al., 2015). Shi and collaborators recently proposed a multifunctional nanoplatform to merge photodynamic and radiofrequency therapy and cancer diagnosis (Shi et al., 2014).

Furthermore, also nanodiamonds are interesting instruments for imaging and diagnostic presenting intrinsic fluorescence features (Fu et al., 2007; Mochalin et al., 2012).

New important tools for the biomedical research, that are becoming more and more necessary for the modern healthcare, are biosensors; indeed, CNTs due to their peculiar

electric and optical characteristics, may be combined into extremely sensitive probes and sensors (Wang and Dai, 2015). One example was presented by Iverson and colleges, where functionalized SWCNTs were used *in vivo,* to sense locally the concentrations of nitric oxide (NO), a molecule involved in physiological and pathological processes, without any immune reactions or different undesired responses. Moreover, they show that, since SWCNTs do not present photobleaching, no changes in their activity were observed after 400 days, underlining the very high stability of these carbon based sensors (Iverson et al., 2013).

Finally, CBNs are valuable candidate for the growth of artificial scaffolds in tissue engineering, to replace or repair damaged tissues (Ku et al., 2013). Physiologically, cells migrate and proliferate to compose tissues and organs within a special environment: the extracellular matrix (ECM). For this reason, synthetic scaffolds need to have physical structure and/or chemical composition reminiscent to the biological milieu (Keung et al., 2010; Shin et al., 2003). Due to their similar dimensions, carbon nanomaterials may provide physical analogues of ECM components, such as collagen fibers. CBNs, given their excellent mechanical properties, can reinforce inorganic and organic synthetic scaffolds and, moreover, their high electrical conductivity may be used to provide an electric stimulation to the artificial structure (Ku et al., 2013). One of the most used CBNs to develop tissue engineering scaffolds are carbon nanotubes, in fact CNTs present dimension diameter from 1 to 100 nm in diameter, comparable to those of extracellular matrix elements. Indeed, experimental and theoretical data have shown that CNTs may ameliorate neural performance by promoting electrical “shortcuts” from the neuron cell body, or soma, to the dendrites (Cellot et al., 2009). Recently, Bosi and colleagues developed a self-standing, micro-porous, synthetic polymer-based scaffold to implement a 3-dimensional neuronal growth. Moreover, the authors entrapped MWCNTs within the scaffold, which allowed nanotubes to interact and boost cultured hippocampal neural circuits (Bosi et al., 2015). Further, it has been reported that nanodiamonds are able to act like a platform for neural growth (Thalhammer et al., 2010) whereas graphene-nanoparticles hybrid scaffold favored growth and alignment of neural stem cells (Solanki et al., 2013).

3. Graphene-Based Nanomaterials

Graphene was discovered by Novoselov, (Nobel Prize in Physics in 2010), Geim and collaborators in 2004. It is a single atom thick, two-dimensional layers of carbon atoms hybridized in sp^2 configuration with a hexagonal structural arrangement (Novoselov, 2004). One of the most exciting research field of graphene is centered on its nanoelectronic applications for next generation computer or sensing, as part of transistors or circuit elements (Ruoff, 2008). More recently, graphene research developed in a variety of engineering applications, including, for example, battery electrodes (Paek et al., 2009; Su et al., 2010), printable inks (Wang et al., 2010), conducting polymers (Stankovich et al., 2006) and supercapacitors (Dikin et al., 2007). Similarly to the case of CNTs, due to graphene's excellent mechanical, chemical and electrical features, this CBM received increased attention in biomedical nanotechnology exploitation (Qu et al., 2018; Tonelli et al., 2015). This plethora of applications includes graphene (monolayer) and, increasingly, many graphene-related materials, called graphene-based nanomaterials (GBNs).

3.1 Graphene Nanomaterial Family

Graphene nanomaterials are classified based on lateral dimension, number of layers in the sheet, surface chemistry and their chemical composition.

GRAPHENE or *MONOLAYER GRAPHENE* is, among all the GBNs, the compound that received the largest interest because of its properties (Geim, 2009). It is produced from graphite flakes by mechanical exfoliation or synthetized from non-graphite source via chemical vapor deposition (CVD) growth (Whitener and Sheehan, 2014). It is characterized by a large surface area, high thermal and electrical conductivity and mechanical flexibility (Kostarelos and Novoselov, 2014; Sanchez et al., 2012). Usually, in the absence of oxygen groups, it is highly hydrophobic.

GRAPHENE OXIDE (GO) is the oxidized form of modified graphene. Most commonly, it is produced by acid-base treatment of graphite oxide (3D structure) followed by sonication. Different functional groups are present on the GO surface, among them, we can find oxygen epoxide groups but also carbonyl (=CO), hydroxyl (-OH) and phenol groups attached to the sheet edge. This nanomaterial shows on its surface reactive oxygen functional groups, negatively charged, making GO soluble in water and in other polar solvents (Paredes et al., 2008; Park and Ruoff, 2009). GO is the product of hydrophilic graphene derivate. On the

other hand, GO shows decreased electrical conductivity that, using reducing agent, may be fixed up.

REDUCED GRAPHENE OXIDE (rGO) was obtained by Stankovich and coworkers in 2007 by reducing GO with hydrazine (N_2H_4) for 24 h at 100° C (Stankovich et al., 2007). The intention of GO reduction is usually done to reestablish electrical conductivity but this procedure makes GO more hydrophilic and may lead to precipitates formation. The chemical reduction of GO can be obtained using many other chemical agents, such as sodium borohydride (Si and Samulski, 2008) or ascorbic acid (Zhang et al., 2010). Recently, Wang et al. fabricated high quality rGO with high electrical properties using thiophene (Wang et al., 2014).

NANO-GO or GO nanosheet is a name to define small lateral dimension GO. Indeed, the stability of graphene oxide is size dependent. Usually nano-GOs are going from 5 to 50 nm size while graphene oxide sheets from 50 to 500 nm. GO nanosheets show a higher hydrophilicity due to the greater density of charges coming from the carboxyl ionized groups (-COOH) present on their edges (Luo et al., 2010). Increasing the ratio between surface and volume, nano-GOs display great dispersibility in water and organic solvents. This GBN is an excellent candidate for different biomedical applications (Compton and Nguyen, 2010).

FEW-LAYER GRAPHENE (FLG) can be defined as a structure composed of 2-10 graphene layers originally obtained as a precursor or byproduct in the graphene monolayer production (Novoselov, 2004).

3.2 Properties of GBNs

Graphene-based nanomaterials present unique properties. Among all of them, some are more relevant for their biological exploitation such as surface area, lateral dimension, number of layers and surface chemistry.

SURFACE AREA. Regarding biological interaction of nanomaterials, surely one important and central role is played by surfaces (Nel et al., 2009). In fact, small nanostructures (<10 nm) present on their surface a high part of their atoms exposed and they can mechanically and chemically interact with biological substrates. Single layer graphene is a peculiar case, because in this material every atom is placed on the surface and exposed to the surrounding environment on both sides. Also, monolayer GO presents a similar area even if the random attachment of oxygen on graphene surfaces leads to a disordered sheet and therefore introduces atomic-scale roughness, while all the other GBNs surface areas are smaller due

to the increase number of layers. In biological experiments, an important issue is to have a great stability of the surface area to avoid aggregates formation.

LAYER NUMBER. In each GBN, the specific surface area and stiffness depend on the number of graphene layers present. In fact, the surface area is inversely proportional to the number of layers while the stiffness increases with the third power of the compound thickness or layers number. Single-layer graphene is one of the thinnest GBNs with a thickness around 0.34 nm (Novoselov, 2004). Its hardness is greater than diamond because of the presence in the same plane of strong C-C bonds (Lee et al., 2008), whereas with diamond it can be deformed by low forces like water surface tension (Bellido and Seminario, 2010; Patra et al., 2009). On the contrary, multilayers GBNs during their biological interaction can act like rigid bodies.

LATERAL DIMENSION i.e. lateral size is very important to determine the maximum dimension of the nanomaterial, that is relevant for different biological phenomena depending on size such as cell uptake or blood-brain barrier (BBB) transport. The cellular uptake is susceptible to lateral dimension, with a maximum dimension of the material still going through phagocytosis or endocytosis. GBNs present a great range of lateral size, form the dimension of proteins, 10 nm, to more than the cellular size, >20 µm. Thus, because of their lateral dimension, GBNs can be internalized by cells (small GBNs), provide a support where adhering or spreading (large GBNs) but also represent a biological risk (Sanchez et al., 2012).

SURFACE CHEMISTRY. GBNs, even before any functionalization, present different surface chemistry. Single layer graphene, for example, is characterized by a hydrophobic surface and it requires specific modification to be applied in biological fluids. In contrast, GO surface is partially hydrophobic with hydrophilic area (Hsieh and Chen, 2011) and contains negative charges on the edge due to the presence of carboxylate groups (Cote et al., 2009). Due to its solubility in aqueous medium, much of the biomedical studies are done on GO nanosheets, even if it has been showed that long-term stability of GO in saline or culture medium requires specific functionalization (Feng and Liu, 2011; Sun et al., 2008).

3.3 GBNs For Biomedical Applications

In the last decade, graphene-based nanomaterials have attracted an increasing interest in biomedical application including drug and gene delivery, stem cell differentiation,

bioelectrodes, bioimaging, biosensor and tissue engineering (Bitounis et al., 2013; Ding et al., 2015; Feng et al., 2013; Yang et al., 2013a). The attention to apply GBNs in the biomedical field is related to the remarkable features of these materials such as flexibility, mechanical properties, thermo-electrical conductivity, transparency and good biocompatibility. Potentially, GBNs might overwhelm the limitations of different metals, which are nowadays adopted for implantable devices, however characterized by low stability in long-time physiological environment, high inflammatory potential and stiffness (Bramini et al., 2018). Due to these evidences, several studies focused on applying GBNs in modern medicine and in particular in neurology where, one of the most ambitious goal is to develop new tools and technologies to treat central nervous system (CNS) disorders (neural regeneration, drug delivery, sensing and imaging) (Baldrighi et al., 2016; Kostarelos et al., 2017; Reina et al., 2017). In particular, different studies have been done to investigate the interactions between GBNs and CNS such as using graphene-based electrodes for cell analysis (Li et al., 2015a; Medina-Sánchez et al., 2012), for molecules delivery to the brain across the BBB (Dong et al., 2016; Tonelli et al., 2015) and graphene-based scaffolds for cell cultures (Li et al., 2013; Menaa et al., 2015). Moreover, it has been showed that the interaction among neural cells and GBNs may be very useful to study their electrical behavior or, by favoring controlled neural processes elongation, promoting neuronal regeneration (Fabbro et al., 2016; Tu et al., 2014).

3.3.1 Three-Dimensional GBNs-Based Scaffolds

Tissue engineering points to reestablish the functionality of a damaged tissue by interacting it with proper biomaterials. This research field is nowadays in fast and great expansion due to the need of innovative strategy to reach greatly functional, biocompatible and low invasive implants for long time applications. In particular, when referring to the CNS, implantable devices can be very beneficial to stimulate and to record the neuronal electrical activity (Bramini et al., 2018). Between the devices that have been design and manufactured as neural interface there are deep brain stimulations implants (DBI), that allow to stimulate electrically deep CNS structures, used for example to treat tremors in Parkinson's disease (Perlmutter and Mink, 2006); cochlear prosthesis able to transform external sounds in electrical signals (Spelman, 2006); neural interface systems to help people in motor rehabilitation after damage or diseases of the motor system (Hatsopoulos and Donoghue,

2009) or in diagnostic, microfabricated electrodes to outline brain activity and signal processing (Chang, 2015). To define suitable neural implants several features are required such as good biocompatibility, low inflammatory response and avoiding the implanted tissue damage; moreover, if neural recordings are planned, a low signal-to-noise ratio is required. In this research field, GBNs characteristics can be exploited to develop new devices and improve the mechanical electrical and optical features of neural interfaces. Engineered 3D scaffolds is one of the most traditional applications of GBNs-based device in medicine that could be applied for *in vitro* or *in vivo* neuronal regeneration, for recording and stimulation or for drugs delivery (Cheng et al., 2017; Cong et al., 2014). 3D GFNs-structures can offer a controlled environment where cells can grow with geometries closer to the *in vivo* condition. Different 3D scaffolds have been developed and studied *in vitro* even if, up to now, just few of them have been tested also *in vivo*. For example, 3D flexible and porous rGO scaffolds were implanted in the injured rat spinal cord showing no local and systemic toxicity and the capacity of these devices to promote recovering tissue integrity after the lesion, even though uncapable to guide neural growth through it (López-Dolado et al., 2015). Moreover, rGO scaffolds chronically implanted were able to favor immunomodulation, angiogenesis but only partial regeneration of axons (López-Dolado et al., 2016). Different studies reported also how 3D graphene and GO structures can be compatible substrates for steam cells (Guo et al., 2016; Sayyar et al., 2016; Serrano et al., 2014). Beside the fact that within 3D graphene-based foams neural stem cells (NSCs) were able to growth, proliferate and differentiate into astrocytes and neurons, Li N. and collaborators showed how these structure were optimal stage to stimulate electrically the NSCs and improve their differentiation (Li et al., 2013). Not only NSCs but also dissociated hippocampal neurons have been cultured within 3D graphene-based scaffolds; as reported by Ulloa Severino et al., 3D neural cultures showed a more extended connectivity linked to a greater network synchronization if compared with 2D graphene structures (Ulloa Severino et al., 2016). To date the applications of 3D GBNs-based implants in neuroscience are still limited if compared with other biomedical area such as anticancer therapy (Xu et al., 2018), muscles (Mahmoudifard et al., 2016), guide bones (Lu et al., 2016) and cartilage regeneration (Nieto et al., 2015) but we expect the development and improvement of functional 3D GBNs-based devices for nervous system purposes in the next future.

3.3.2 Graphene-Based Nanosheets For Molecules Delivery

GB nanosheets cytotoxicity. A different research branch of these nanomaterial applications is to use GBN nanosheets as drug *per se* or to delivery drug, gene or protein into the CNS bypassing the BBB. In literature, studies about the interaction between GB nanosheets and different cell types reported several common cytotoxicity mechanisms that include for example the physical interaction with cell membranes (Seabra et al., 2014), production of reactive oxygen species (ROS) that lead to oxidative stress (Mittal et al., 2016), DNA and mitochondrial damage (Fahmi et al., 2017; Pelin et al., 2017), but also necrosis and apoptosis (Lim et al., 2016). In the neuroscience area, several studies have been done using both neuronal-like cell lines (Lv et al., 2012) and primary cultures (Bramini et al., 2016; Rauti et al., 2016) but, to date, the interaction between neurons and glial cells and GB nanosheets is still not very clear primarily due to intrinsic features of these materials. In fact, the controversial biocompatibility of graphene-based nanosheets is related to the big heterogeneity of the available materials and the different methods of synthesis; due to these, nanosheets can be characterized by different size, aggregation state, chemical surface and thickness, which, as we said previously that can affect the interaction with biological systems.

To date, based on previous findings it is apparent that GO is better tolerated than other graphene family materials like graphene or rGO and also that bigger nanosheets are more toxic than smaller one (Bianco, 2013; Ou et al., 2016); moreover, since GO presents great stability and solubility in biological fluids, it is preferred for biomedical studies (Reina et al., 2017).

GB nanosheets for molecule delivery. One important feature of GBNs is that their surface may undergo chemical functionalization and in this way it is possible to remodel their structure, for example, by adding hydroxyl, carboxyl, amino or other functional groups (John et al., 2015) and increase their biocompatibility degree. Moreover, the large surface area of GB nanosheets can host and carry also biomolecules such as drugs, antibody, genes and proteins (Chen et al., 2013). In fact, GB nanosheets might be used as a structure to deliver molecules to target cells, loading them via noncovalent functionalization like hydrophobic or π-π stacking interactions and hydrogen bonding (Georgakilas et al., 2016)(Fig.3)

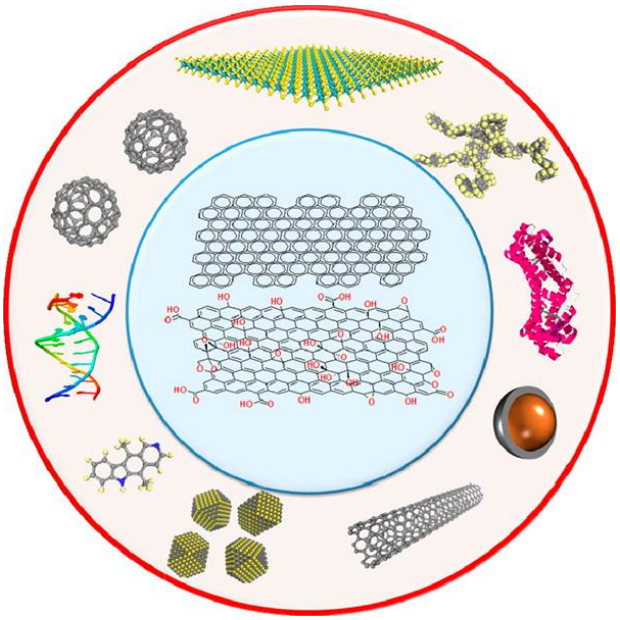

Figure 3. *Schematic representation of noncovalent interactions of graphene and GO with different molecules: MoS2, aromatic polymers, proteins, core–shell nanoparticle, nanotube, quantum dot, ellipticine (drug/photoluminescence probe), DNA segment, and fullerenes (clockwise from top) (from* (Georgakilas et al., 2016).

For delivering molecules into the CNS, an important factor that must be taken into consideration is the blood-brain barrier. The BBB is one of the most important physiological barriers which purpose is to control and limit the entrance from the circulatory system into the brain of foreign materials and chemical substances. The neuroprotective function of BBB also blocks the crossing of drugs designed to reach target cells in the brain; in fact, from all the drugs that have been created for neuronal diseases only the 5% enters the CNS. In literature, several works have been published about the ability of GB nanosheets, functionalized or not, to bypass the BBB. For example, Mendonça and colleagues reported that intravenously administration of rGO in rats led to a downregulation of the tight and adherent junction proteins of the BBB and after that rGO nanosheets was found in the hippocampus (Mendonça et al., 2016a). The same group showed also that the PEGylation of rGO induced a toxic effect to the key components of BBB, like astrocytes and endothelial cells, *in vivo* (Mendonça et al., 2016b). A different approach to allow GB nanosheets to reach the brain is represented by the use of ultrasounds, which can physically open temporarily the tight junction of the BBB. Yang et al., using this method were able to deliver GO nanosheets, administered through tail vein injection, into the brain (Yang et al., 2014). An additional method is the functionalization of GB nanosheets surface with specific biomolecules that can lead nanomaterials to cross the BBB (Goenka et al., 2014; John et al.,

2015). The number of molecules/drugs that are successfully loaded to GB nanosheets is growing and one of the main applications is anticancer therapy where nanomaterials are linked to chemotherapeutics. Moreover GBNs, due to their optical properties, are been studying for diagnostic as attractive tools for bioimaging (Zhang et al., 2013). For all these reasons, GBNs delivery tool, if functionalized or associated with new technological approach, can be a promising player for neuroscience applications.

4. Three-Dimensional *in vitro* Neuronal Culture Models

In vitro models are extremely important and useful tools to study and evaluate the cellular behavior in highly controlled conditions. Regardless of the extraordinary progress in tissue engineering and in bioengineering cell culture systems, two-dimensional (2D) cell culture continues to be the principal technique in the majority of biological studies. This is partly due to the fact that 2D cell culture are well characterized in literature and data are easily comparable; moreover, 2D samples are fast and simple to obtain and the techniques are definitely well set. However, 2D cell cultures present many limitations; first among all, cells that grow in 2D structures do not represent carefully the features of the three-dimensional (3D) tissue *in vivo*. In fact, cells are grown on flat surfaces, made of plastic or glass, which present unfamiliar mechanical properties and also the absence of the extracellular matrix support may lead to important changes in the growth, behavior and morphology of the cells (Bozza et al., 2014; Daud et al., 2012; Yano et al., 2015). To fill the gap between *in vivo* and 2D *in vitro* conditions, new approaches have been developed such as 3D cell cultures. In neuroscience, 3D cell cultures preserve several good aspect of the *in vitro* model but with higher levels of cell survival, longer outgrowth of neurites and distinct patterns of differentiation if compared with 2D one (Blackshaw et al., 1997; Choi et al., 1993; Pardo and Honegger, 2000). Also, in 3D cultures, cells show a more spherical body and the processes have the possibility to spread in all directions (Fig.4).

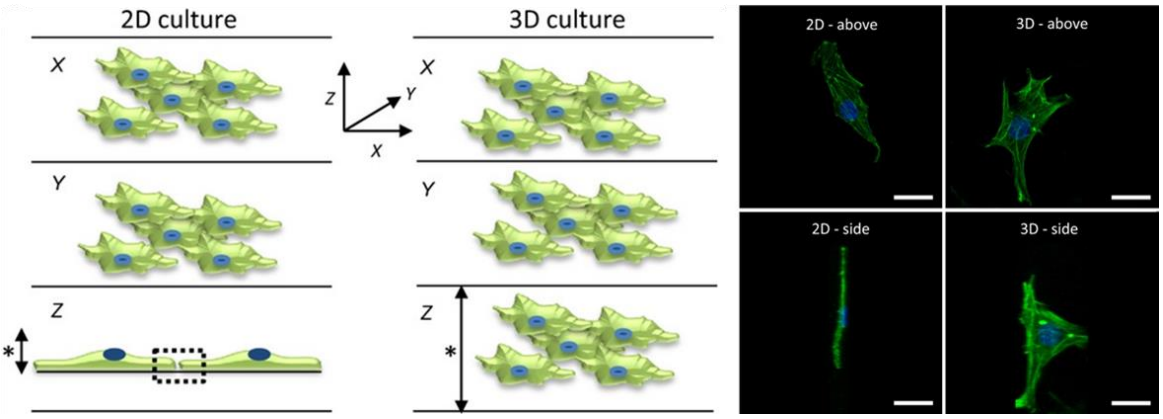

Figure 4. *(Left). Visualization of cells for the three dimensions (X,Y,Z). In conventional 2D culture, cells grow as monolayers on a solid substrate; they flatten and possess a low vertical height. In contrast, cells cultured in a 3D model preserve a more physiological 3D structure and possess more normal dimensions all round. Moreover, the overall height (*) of a conventional 2D culture is relatively fixed, whereas that of a 3D culture is more versatile. Interactions between adjacent cells cultured in 2D are restricted to the periphery of the cells within a single plane (dotted box), whereas in 3D models the*

scope of intercellular contact is all around. (Right) Images acquired by confocal microscope of a single fibroblast grown in 2D or 3D culture. Scale bar: 10 µm (from Knight and Przyborski, 2015)

3D models of the CNS can be obtained by explanted tissue cultures, self-assembled aggregate cultures and scaffolds-based cell culture (Ko and Frampton, 2016). *Explanted culture* can be obtained with techniques that enable to culture preserved tissues *in vitro*. This method permits to dissect the desired tissue from animals and to preserve the original 3D architecture. Brain or spinal cord slices can be used fresh (acute slices) or they can be cultured in cell culture dishes using supporting membrane inserts (organotypic cultures) offering the possibility to study neuronal pathways, or nerve growth or neurological diseases (Navarro et al., 2016; Plenz and Kitai, 1996; Ravikumar et al., 2012). *Self-assembled aggregate cultures* exploit the natural propensity of cells to aggregate and they include spheroids, neurospheres and embryoid body which can be developed by different techniques including suspension cultures or using microwells (Choi et al., 2013; Dingle et al., 2015; Ko and Frampton, 2016). Neural spheroids may be obtained either with primary cell cultures and cell lines, for example neuroblastoma cell lines (Besançon et al., 2012; Dingle et al., 2015). One important limitation of spheroids is the dimension that the cellular aggregate may reach; in fact, bigger is the cluster lower is the amount of nutrients and oxygen that can diffuse and reach the inner cells leading to necrosis of the center of the structure. However, this type of 3D culture is very common for studying tumors due to the fact that cell aggregates show good analogy to actual tumor tissue (Yano et al., 2015). In the other hand, spheroids present a fast rate of production and show a great potential for different applications like drug screening and toxicity testing (Choi et al., 2013).

All the methods described above to develop 3D cultures are useful models to study various aspects of the nervous system, however they still present several limitations such as loss of connectivity, low gases diffusion and lack of control in the choice of the cell type. A different approach to develop 3D culture, which might overcome these limitations, is to use synthetic and/or natural biomaterial to create scaffolds where cells can grow and differentiate and reproduce a neural tissue in a very controllable system.

4.1 Scaffold-Based Cell Culture: The Hippocampus

In this thesis, I have been working with hippocampal cultures to characterize and develop 3D systems enriched with graphene interfacing.

Scaffold-based cell cultures exploit the presence of a 3D structure to recreate a cellular network with a 3D architecture. Nowadays, a great number of materials have been developed to engineer a 3D environment both natural such as agarose, collagen, laminin or synthetic like polycaprolactone, polyethylene glycol, polystyrene and polydimethylsiloxane (Ko and Frampton, 2016). Due to the big range of materials available the choice of the scaffold and its properties is very important and might affect several cellular functions and organization, and gene expression (Bozza et al., 2014; Li et al., 2007). In developing a scaffold for 3D culture there are different criteria that should be taken into consideration depending on the cell type we want to grow within it. To study *in vitro* neural system, dissociated hippocampal cultures have been popular for addressing and investigating neuronal processes and behaviors. Part of their popularity derives from their physiological relevance; hippocampus, for example, is one of the main sites for acquisition and storage of memory and it is also a part of the brain affected by neurodegenerative diseases. In addition, *in* vitro hippocampal network allows investigating synapses formation and functions; in fact, in the whole hippocampus, principal neurons send out recurrent collaterals that synaptically contact other pyramidal cells. Due to these features dissociated hippocampal cultures are an accessible and widely adopted model to study both physiological neuronal development and neurodegeneration (Hollenbeck and Bamburg, 2003).

In terms of scaffold features, one of the most important is the *porosity*, in fact scaffolds for 3D culture must present a strong but also porous structure where cells can adhere but also have the possibility to migrate and extend processes. The presence of pores is very important for the sufficient gases diffusion and medium perfusion to allow cell survival. The most used techniques to develop macroporous scaffolds are based on exploiting templates and molds that can be removed by dissolution or heat processes (Aurand et al., 2018; Bosi et al., 2015; Zhang et al., 2007). The *pore size* and the *stiffness* of the scaffold are also important and related with each other. In particular, the pore size must be correlated with the dimension of the selected cell type; in fact, pores should not be too small or too big to allow the formation of culture with a 3D architecture and at the same time to avoid cell clusterization and aggregation (LaPlaca et al., 2010). The *charge* of the 3D structure may influence the porosity and the cell behavior like in the study published by Dillon and coworkers where they showed that charged biopolymers affect the neurite outgrowth in a polarity related manner (Dillon et al., 1998). A crucial property of 3D scaffold to take into

consideration is its *stability* during the time both for short and long-term cultures. In fact, the structure can go into degradation over time or may be modified by enzymatic reaction, especially when the scaffold is made of biomaterials like Matrigel (LaPlaca et al., 2010).

4.2 Polydimethylsiloxane (PDMS)

In the last two decades, the silicon-based elastomer polydimethylsiloxane (PDMS) has become very popular material for microfabrication and microfluidic devices in general but also, it has been more and more applied for *in vitro* biological applications (Gross et al., 2007; Meyvantsson and Beebe, 2008; Yeon and Park, 2007). This is due to its intrinsic properties and moreover because its simple fabrication procedures and pattern adjustability (Regehr et al., 2009). Among all its characteristics, PDMS is optically transparent, flexible and permeable to gases and it adhere to generally utilized substrates like glass; these make it suitable for microscopy and for long-term cell cultures. Moreover, the surface of pristine PDMS presents a remarkable hydrophobicity, mostly because of the presence of methyl groups; however this can be overcome using oxygen plasma treatment which, introducing hydroxyl groups, convert PDMS surface to hydrophilic (Zhou et al., 2012). Indeed, PDMS surface can be chemically functionalized but also enriched with materials such as nanoparticles (Bai et al., 2010) or CNTs (Han et al., 2013).

Recently, PDMS has been used to fabricate 3D porous scaffold for *in vitro* 3D neural culture (Bosi et al., 2015) and spinal cord implantation *in vivo* (Usmani et al., 2016).

5. The Amygdaloid Complex

In this thesis, I have developed 2D cultures from the amygdaloid complex to test sGO flakes ability to interfere with synaptic excitation in a neural system governing complex behavioural responses.

5.1 Anatomy and Connection

Despite the fact that human beings own a number of cognitive abilities that make a distinction between us and other animals, we share emotional behaviors — described as behavioral responses to emotionally relevant and vital stimuli such as food or threats — with other vertebrates.

Amygdala is a region of the brain that is very important for emotional processing, of which circuitry and function have been reported to be well-conserved across evolution (Figure 5), even if differences within species do exist (McDonald, 1998). Indeed, also non-mammalian species such as birds, reptiles and fish present an amygdala-like brain region that shows similar circuits and functions to the mammal one (Jarvis et al., 2005; Johnston, 1923; Lanuza et al., 1998).

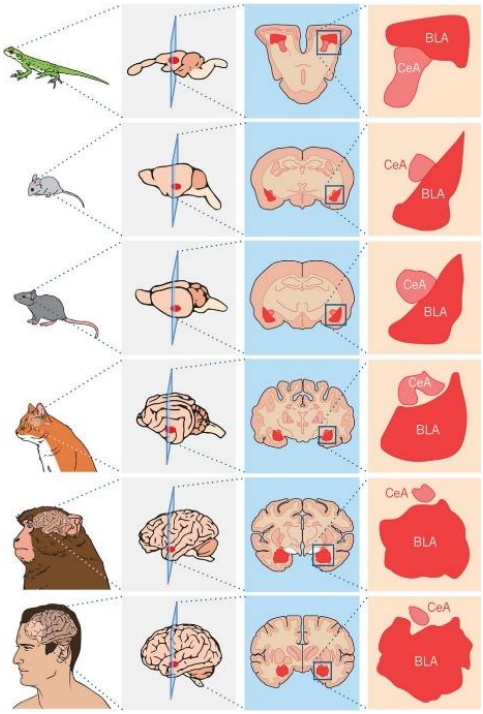

Figure 5. *Primary amygdalar nuclei and basic circuit connections and function are conserved across species. An enlarged image of the basolateral complex of the amygdala (BLA) and central nucleus of the amygdala (CeA) or analogues are shown next to a coronal section from the brains of a lizard, mouse, rat, cat, monkey and human (From Janak and Tye, 2015).*

The amygdala is an almond-shaped structure nestled deep in the temporal lobe and was first described and named by the anatomist K.F. Burdach in the 19th century, who originally identified a group of cells that are known as the basolateral complex. After that, in many species, a great number of structures have been described around the basolateral complex creating what is today known as the amygdaloid complex (Sah et al., 2003).

The amygdaloid complex is structurally diverse and it is comprised of about a dozen nuclei. In turn, these can be divided into subgroups that have extensive connections, both internuclear and intranuclear. These nuclei and subnuclei are characterized by different cytoarchitectonic and connections they make (Krettek and Price, 1978).

Three main groups or complexes of nuclei can be identified: 1) the deep or basolateral group, (BLA), which includes the lateral nucleus, the basal nucleus and basomedial nucleus; 2) the centromedial groups, composed by the medial and central nuclei and 3) the superficial or cortical-like groups, which includes the cortical nuclei and the lateral olfactory tract nucleus. Moreover, a distinct set of nuclei do exist, which are listed apart because they do not fit within any of these groups, such as the amygdalohippocampal area and the intercalated cell masses (Sah et al., 2003).

One traditional view is that the amygdala is composed of an evolutionary primitive part correlated with the olfactory system (the cortico-medial groups) and a recently developed division related with the neocortex (the basolateral region). Lately, it has been discussed that amygdala is not a functional or structural unit, however it consists of regions that belong to different regions or systems of the brain. Following this point of view, for example, the central and medial amygdala are suggested to be ventral expansion of the striatum while the basal and lateral nucleus instead of being regions related to the cortex, they are seen as a nuclear extensions of it (LeDoux, 2007).

Indeed, morphologically, the neuronal composition of the BLA is similar to that of the cerebral cortex except for the fact that neurons are randomly oriented in the BLA. As in cortex, BLA contains two classes of neurons. The dominant group (~80%) consists of glutamatergic projection cells with multipolar dendritic trees covered with spines and axons contributing multiple collaterals to neighboring BLA cells, amygdala nuclei, or other structures of the brain. The second class of BLA neurons consists of local circuit GABAergic cells with short axons and aspiny to sparsely spiny dendrites (~20% of the cells). Conversely

the CeA is a striatum-like that is constitute of GABAergic medium spiny neurons which project to different brain areas (Tovote et al., 2015).

CONNECTIVITY. Amygdala nuclei and subnuclei show their unique inputs and outputs. Since describing all the amygdala connections is not the aim of this thesis I will mention just some key examples. The lateral amygdala is commonly identified as the gatekeeper of the complex, receiving sensory inputs from the visual, olfactory somatosensory and auditory area. However, different information reaches the amygdala through diverse nuclei (Figure 6).

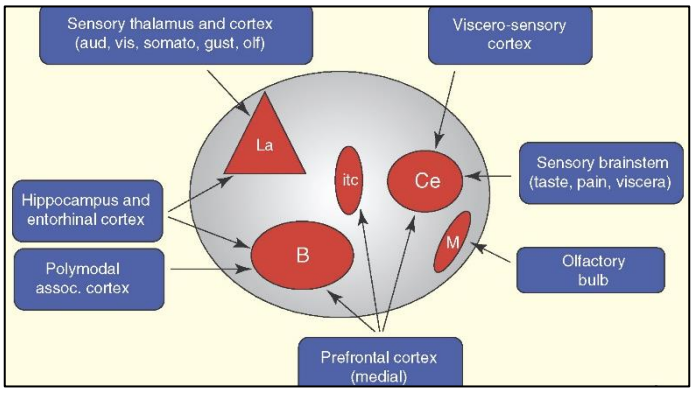

Figure 6. *Inputs to some amygdala nuclei. Abbreviations: B, basal nucleus; Ce, central nucleus; ITC, intercalated cells; La, lateral nucleus; M, medial nucleus. Aud, auditory; vis, visual; somato, somatosensory; gust, gustatory (From LeDoux, 2007).*

The central nucleus instead is one of the most important amygdala output nucleus where projection neurons synapse to brainstem areas that control physiological responses and specific behaviors (Figure 7).

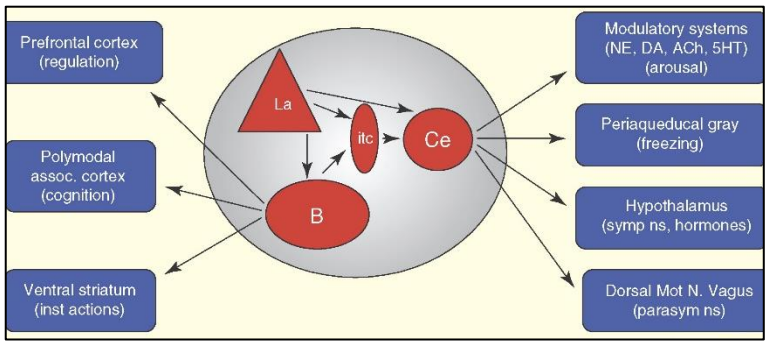

Figure 7. *Outputs from some amygdala nuclei. Abbreviations: NE, norepinephrine; DA, dopamine; Ach, acetylcholine; 5HT, serotonin (From LeDoux, 2007).*

The information from the lateral nucleus to the central one must travel through different middle station; one possible pathway is from lateral to the basal nuclei which project to the

central one. Moreover, the information might be delivered to the intercalated cells that are connected to the principal amygdala output.

In addition to the central nucleus, different output connections start from the basal one (Figure 7). In fact, the latter is also connected with striatal areas implicated in the control of instrumental behaviors, like escaping to safety (LeDoux, 2007).

5.2 Isolated Rat Amygdala Culture

Over the past decades there has been an increase of interest in the amygdala complex mostly due to recent data on humans showing the role of the amygdala in determining the emotional meaning of sensory inputs (Adolphs et al., 1994; Scott et al., 1997) and in regulating the memory of emotionally eliciting stimuli (Cahill and McGaugh, 1998; Hamann et al., 1999). These functions are extremely important for successful managing in daily social surroundings (Morris et al., 1998). Knowing and understanding the roles of amygdala in human beings, however, is preceded by many laboratory works where are investigated the neuronal pathways and cellular mechanisms implicated in the emotional behavior of the rats (Gallagher and Holland, 1994). Regarding this, knowing the connectivity of the rat amygdala nuclei has been a key aspect in evaluating the hypothesis that were generated concerning the possible role of amygdala into different components of emotional behavior. Different works where electrophysiological activity were recording in various amygdala nuclei during a behavior task (Rogan and LeDoux, 1996) or where different nuclei were selectively lesioned (Killcross et al., 1997), has led to a further need for a deeper understanding of amygdala connectivity at molecular, cellular and functional levels.

The simplest model that can be used to reach these goals is culturing *in vitro* isolated rat amygdala neurons. This *in vitro* model is an invaluable tool for investigating cell behavior and it has been using to characterize and describe molecular and cellular function in a very controlled setting (Kaneda and Akaike, 1989; Lin et al., 2001; McCool and Farroni, 2001; Meis and Pape, 1997). Moreover dissociated amygdala culture might be exploited for studying the chronic and toxic effect of different chemical compounds, like ethanol (McCool et al., 2003) or to evaluate the interaction between neurons and nanomaterials.

AIMS OF THE STUDY

In the past few years, a growing number of studies were published showing the extensive applications of GBNs in the modern medicine and in particular in neurology. However, use of GBN in biomedicine requires a deeper understanding of the interaction between nanomaterial and neuron in terms of cell responses or cellular uptake. In fact, due to the unique properties that GBNs possess, these materials, interacting with cellular and subcellular components, might modulate important biological processes.

The major aim of my work has been to understand the impact of nanomaterials on the neuronal network and in particular to study the ability of GBNs in shaping the synaptic activity by various physiological methods.

During the first part of my PhD, we exploited elastomeric 3D scaffolds functionalized with single layer graphene to evaluate the effects of this nanomaterial, combined together with the 3D architecture, on the neuronal network dynamics. In fact, a better understanding of graphene ability to alter the neuronal activity in a 3D environment will allow to develop and design future devices for tissue engineering.

We were able to recreate genuine 3D hippocampal cultures within the scaffolds, with and without graphene. Thus, we evaluated the synaptic activity of neurons grown in the two conditions and we described the graphene capability to perturb neural circuits maturation using imaging techniques.

Recently, graphene oxide flakes characterized by small lateral size (s-GO) have been reported to alter selectively the glutamatergic synaptic activity of hippocampal neurons (Rauti et al., 2016, 2019). This selective and precise interaction with the neuronal signaling in the CNS might lead to design novel neuropharmacological tools that can be exploited when the excitatory synapses are the desired target. In this regard, anxiety related disorders (ArDs), including for example post-traumatic stress disorders, are diseases which present alterations in the amygdala neuronal circuits; in particular they are characterized by a glutamate hyperactivity in the excitatory synapsis of amygdala neurons (Cortese and Phan, 2005; Ganella and Kim, 2014; Wierońska et al., 2011).

For all these reasons we designed a project which aim was to study the interaction, at the cellular level, between s-GO and amygdala neurons. Thus, we first developed and

characterized amygdala dissociated cultures through electrophysiological and immunofluorescence techniques and subsequently we explored whether s-GO ability in targeting selectively hippocampal glutamatergic synaptic transmission might be translated in different neuronal models.

PAPER 1: Tuning neuronal circuit formation in 3D polymeric scaffolds by introducing graphene at the bio/material interface

Rossana Rauti[1†], Nicola Secomandi[1], Cristina Martín[2,3], Susanna Bosi[3], Francesco P. U. Severino[1#], Denis Scaini[1], Maurizio Prato[3,4,5], Ester Vázquez[2,6*], Laura Ballerini[1*]*

[1]International School for Advanced Studies (SISSA/ISAS), Trieste 34136, Italy

[2]Instituto Regional de Investigación Científica Aplicada (IRICA), Universidad de Castilla-La Mancha, Avda Camilo José Cela, 13071 Ciudad Real, Spain.

[3]Department of Chemical and Pharmaceutical Sciences, Università degli Studi di Trieste, Via Licio Giorgieri 1, Trieste 34127, Italy

[4]Carbon Bionanotechnology Group, CIC biomaGUNE, Paseo Miramón 182, San Sebastián, 20014 Guipúzcoa, Spain

[5]Basque Foundation for Science, Ikerbasque, Bilbao 48013, Spain

[6]Faculty of Chemical Science and Technology, Universidad de Castilla-La Mancha, 13071 Ciudad Real, Spain

Corresponding Authors:
* E-mail: laura.ballerini@sissa.it
* E-mail: ester.vazquez@uclm.es
* E-mail: prato@units.it

Keywords: graphene; hippocampal network; 3D-scaffolds; neuronal maturation

Abstract

2D cultures are useful platforms allowing studies of the fundamental mechanisms governing neurons and synapse functions. Yet, such models are limited when exploring the contribution on networks dynamics of circuit topology, when neuronal branches can navigate in the 3D-space. 3D platforms fill this gap and favor investigating topologies closer to the real brain organization. Graphene, an atom-thick layer of carbon, possesses remarkable properties and since its discovery has been considered highly promising in neuroscience developments. Here, we exploit elastomeric 3D platforms endowed with graphene cues to modulate, by interfacing graphene in 3D topology, neuronal circuits. We successfully reconstructed ex-vivo neuronal networks within 3D scaffolds, with and without graphene, characterized by comparable size and morphology. By confocal microscopy and live imaging we documented the 3D architecture of synaptic networks sustaining high rate of bursting in 3D scaffolds, an activity further increased by graphene interfacing. We report changes in the excitation/inhibition ratio, potentially following 3D-graphene interfacing. We thus propose a hypothesis, where the combination between synapse formation under 3D architecture and graphene interfaces affected the maturation of GABAergic inhibition, tuning the balance between hyperpolarizing and depolarizing responses, and potentially contributing to network synchronization in the absence of changes in GABAergic phenotype expression.

1. Introduction

The brain ability to elaborate and store information relies on neural circuits topology, that is the way neurons are synaptically connected in a given network. The architecture of neural connectivity, therefore, is one of the crucial mechanisms enabling the emergence of a

particular function from specific brain circuitries.[1] Investigating the interplay between morphology and function in brain networks is an important yet challenging task limited, for example, by the overwhelming complexity of the intact Central Nervous System (CNS). Recently, the development of biomimetic 3D scaffolds has allowed to culture neuronal and glial cells within an interconnected porous structure, promoting the development of more complex three-dimensional organizations of neuronal synaptic networks than in traditional monolayer conditions.[2,3] We recently developed a 3D versatile platform that provides a biocompatible cellular elastomeric scaffold to be engineered for tissue formation, that we further nanostructured with nano-topographies by means of multi walled carbon nanotubes (MWCNTs).[2,4] Decorating the elastomeric structure with nanomaterials exploits the scaffold properties at the interface, for example guiding growth and adhesion of axons to the device or implementing the 3D construct of active components, such as electrically conductive pathways.[4] In addition, apart MWCNTs,[2,5-7] many other carbon-based nanomaterials, as for example graphene,[8] may provide artificial biomimetic cues able to affect synapse formation or neuronal information processing through the physical interactions of the nanomaterial with the biological environment. Hybridizing 3D biomimetic scaffolds with nanomaterials demonstrated to improve their biocompatibility,[9] their stability in vivo,[4] and provides efficient tools to modulate biological processes.[4,8] Graphene, a single atomic plane material made of sp2-hybridized carbon atoms, is characterized by peculiar properties, including high electrical conductivity, stiffness, electron mobility, mechanical flexibility and optical transparency.[10-13] The recent exploiting of graphene as component of neural interfaces relies on the combination in a single material of all these features.[14]

In neuroscience, flat graphene substrates has shown to promote axon sprouting and outgrowth,[15] to reduce tissue inflammatory responses[16,17] and, surprisingly, to enhance neuron electrical signaling,[8,18] highlighting its potential as a tool for engineering neuronal interfacing devices.[14,17,19-22] The translation of graphene capability to perturb neuronal network activity from 2D to 3D represents the next step in the design of artificial platforms for tissue engineering. Only a few studies report how graphene-based 3D constructs, yet with diverse graphene derived materials (from graphene foams to graphene oxide scaffolds), interact with biological tissue/cells and how the interfaced neuronal network responds when exposed to graphene in 3D.[3,13,23,24] However, a detailed characterization of neural circuit adaptation to a 3D graphene environment is currently missing. Here, we took advantage of self–standing elastomeric scaffolds, characterized by a micro-porosity able to shape a functional 3D neuronal network,[2] to create a condition where neuronal cells could interact with single layer graphene in a genuine three-dimensional environment. We studied intracellular calcium activity in neurons within 3D hippocampal cultures that differed only by their being interfaced to graphene or not providing evidence that, despite the similar cellular composition and morphology of the resulting 3D neuronal networks, graphene has the ability to alter the synaptic inhibitory control of the network emerging activity. Surprisingly this effect seems intrinsic of the 3D topology since in 2D it is not present.

2. Results

2.1 Fabrication and characterization of 3D-scaffolds

We present here a micro-porous, self-standing elastomeric-scaffold whose facets are covered by graphene and able to sustain the development of a genuine 3D-network of cells from rat hippocampus. Control 3D scaffolds consisting of polydimethylsiloxane (PDMS) alone were fabricated following a previously described procedure.[2,4] Briefly, the scaffold

was made of PDMS with micrometric cavities generated by the dissolution of a sugar template after that all interstitial space was previously embedded by the elastomer and cured. To exploit the ability of graphene to impact a three-dimensional neuronal circuit, the pristine 3D PDMS scaffold fabrication procedure was then modified by mixing few-layer graphene flakes with the sugar. This produces an agglomerate with graphene flakes layered on all sugar grains' faces. After PDMS infiltration and curing, sugar dissolution leaves graphene flakes partially embedded, and consequently trapped, at the surface of the PDMS scaffold resulting in 3D PDMS-Graphene (3D-PDMS-GR) samples. The starting graphene flakes were fully characterized by TGA, Raman spectroscopy, and TEM (Figure 1, A-C). A low number of defects/functional groups characterize the graphene surface as pointed out by TGA analysis (Figure 1A) while Raman spectroscopy shows a ratio between the intensities of D and G bands (ID/IG) of 0.42 (Figure 1B). These two results indicate that the starting graphene material consist of about 4 layers graphene flakes.[25-27] TEM analysis, on the other hand, shows that the distribution of lateral dimensions of the flakes, based on a gaussian fit, is centered around 304 ± 124 nm (Figure 1C).

The presence of graphene flakes trapped within 3D PDMS-GR was assessed by Raman spectroscopy. An example of a typical Raman profile acquired within a pore of a 3D PDMS-GR scaffold is displayed in Figure 1D (average of 25 consecutive spectra) where graphene characteristic tangential (G, ~1580 cm-1), disordered (D, ~1350 cm-1) and second order (2D, ~2700 cm-1) peeks are clearly visible,[28] together with two very intense bands around 3000 cm-1 which correspond to the methyl stretching vibrations (symmetric and asymmetric) of the PDMS.[29] In Figure 1E we show a 3D mapping of the G-band intensity within a parallelepiped extending from the surface of the scaffold to 10 µm in depth by steps of 1 µm. A total of 4290 spectra were represented in the 3D representation and a color code was

chosen to represent G-band intensity (red for higher intensities). From this, we were able to chemically visualize graphene on PDMS scaffold facets confirming the presence of homogeneous distribution of graphene flakes trapped within the scaffold surface.

We aimed at a system developed to allow the growth (within a three-dimensional environment) of a neuronal network directly interfaced to graphene and, at the same time, soft enough to resemble the compliance of neural tissues. Using a high-resolution compressive load-cell we measure, by uniaxial-load compression test (see Methods), an indicative E value of 59.10 kPa for the 3D PDMS scaffold and of 58.82 kPa for the 3D PDMS-GR one (Figure 1F). The two values, obtained calculating the initial linear slope of the corresponding stress-strain curve, are very similar, highlighting the absence of alterations in the bulk mechanical properties due to the superficial layering of graphene.

The electrical characterization (see Methods) of the graphene enriched PDMS scaffold was performed as function of scaffold deformation squeezing the sample between two conductive, flat, electrodes (Figure 1G, left). Our analysis pointed out the necessity to induce at least a 20% deformation in the 3D PDMS-GR scaffold to start having a measurable value of resistivity (4.7 GΩ·mm). Not surprisingly, resistivity value decreased monotonically as deformation was increased, reaching a final value of about 2.7 MΩ·mm at 60% deformation (Figure 1G, right plot).

The general morphologies of both 3D PDMS and 3D PDMS-GR scaffolds were compared by scanning electron microscopy (SEM) reconstructions (Figure 2A, left and right, respectively). SEM analysis revealed very similar morphologies for the two scaffolds and showed that sugar crystals dissolution generates faceted interconnected pores, which allow networks of channels within the PDMS matrix. The diameter of the pores within the two scaffolds was evaluated in the range of 100÷200 µm in both conditions except that in 3D PDMS-GR

scaffolds their surface is covered by a thin layer of graphene flakes, as pointed out by Raman spectroscopy (Figure 1D and 1E).

2.2 Self-standing PDMS scaffolds sustain hippocampal cells growth in 3D: functional impact of few-layer graphene

To investigate the development of neuronal networks when interfaced in the third dimension to graphene, we seeded rat dissociated hippocampal cells in the two elastomeric micro-porous scaffolds,[2,30] named 3D PDMS and 3D PDMS-GR, whose structure and porosity are shown in the representative SEM images of Figure 2A. The cell composition and 3D organization of cultured hippocampal tissues within the two scaffolds were assessed after 9÷11 days in vitro (DIV) by confocal microscopy of β-tubulin III and glial fibrillary acidic protein (GFAP) immunofluorescence labeling, to visualize cytoskeletal components selective for neurons and astrocytes, respectively (Figure 2B).[31-34] In all cultures tested for confocal reconstruction (n = 8 for 3D PDMS and n = 7 for 3D PDMS-GR), prior to microscopy analysis, neuronal calcium activity was monitored (see below) and at the end of each recording session, the samples were fixed and processed for microscopy. Representative confocal micrographs at low (Figure 2B, first row) and high (Figure 2B, second row) magnifications highlight the formation of a genuine 3D configuration of neurons and glial cells when developed sustained by the 3D PDMS (left) and 3D PDMS-GR (right) scaffolds. To highlight the three-dimensional networks topology into the two porous scaffolds we extrapolated from the 3D confocal images obtained by zeta stacking, the zeta profile reconstructions (Figure 2B, bottom panels). In both conditions (3D PDMS and 3D PDMS-GR) an effective growth along the z axis is depicted confirming that these scaffolds promote three-dimensional cellular networks formation, where neurons and glial cells are disposed on different levels, as also disclosed by cell nuclei distribution (in blue).[2,30] We further

quantified the hippocampal cell density which did not differ in the two conditions for both neurons (3D PDMS: 262.3 ± 29.2 β-tubulin positive cells/mm^2; 3D PDMS-GR: 227.9 ± 16.4 β-tubulin positive cells/mm^2) and astrocytes (3D PDMS: 146.8 ± 18.6 GFAP positive cells/mm^2; 3D PDMS-GR: 118.4 ± 9.2 GFAP positive cells/mm^2; n = 28 visual fields in 3D PDMS and n = 23 visual fields in 3D PDMS-GR, four independent culture series; bar plots in Figure 2C). Biocompatibility together with the ability to instruct a 3D culture formation were thus confirmed for the 3D PDMS platforms and our results suggest that decorating scaffold pores' surfaces by a thin film of few layer graphene flakes did not alter the resulting cellular network in size and morphology.[2]

Primary cultured neurons once reorganized ex vivo in 3D scaffolds are known to develop functional synaptic connections and circuits characterized by the spontaneous generation of temporally structured electrical activity.[2] We explored the network dynamics in 3D PDMS and 3D PDMS-GR by calcium imaging with fluorescent indicators, this is a minimally invasive approach that allows monitoring calcium transients in neuronal populations at single-cell resolution.[2,3,30,35] Neurons, stained with the membrane permeable Ca^{2+} dye Oregon Green 488 BAPTA-1, were simultaneously visualized within the sampled area (visual field 680×680 μm^2; Fig. 3A, left fields of view) and on average 30 ± 12 fluorescent cells were isolated and imaged in each visual field (see Methods). In these recordings, repetitive and spontaneous Ca^{2+} events were detected in 77% (555 out of 723 neurons, n = 23 visual fields, 3D PDMS) and, similarly, in 79% (705 out of 894 neurons, n = 24 visual fields; 3D PDMS-GR cultures) of visualized neurons. In Figure 3A, right, sample tracings of spontaneous fluorescent recordings from active cells are depicted for comparison between 3D PDMS (in green) and 3D PDMS-GR (in red) cultures. Spontaneous and bicuculline (10 μM; a competitive antagonist of $GABA_A$ receptors) sustained activity of two representative cells were shown

for each condition. Calcium events are usually due to spontaneous episodes of synaptic, action potential-dependent, bursts of activity, fully blocked by Tetrodotoxin (TTX, 1 µM; a blocker of fast voltage dependent Na^+ channels; see Methods) applications. We quantified the occurrence of spontaneous Ca^{2+} episodes in active cells by measuring the inter-event interval (IEI), the time interval between the onset of a calcium burst and the beginning of the next one, that was significantly (*** $p < 0.001$; Kolmogorov-Smirnov test) shorter in 3D PDMS-GR cultures (9.8 ± 0.18 s, n = 175 cells, from 5 different series of cultures) when compared to 3D PDMS ones (12.7 ± 0.23 s, n = 208 cells, from 5 different series of cultures; see the IEI cumulative distribution in Figure 3B, left plot). We further quantified network synchronization by evaluating the mean Cross Correlation Factor (CCF; see Methods) of spontaneous calcium episodes. 3D PDMS cultures displayed a CCF value of 0.48 ± 0.04 (n = 14 fields) significantly (** $p < 0.006$, Mann Whitney test) smaller than the value detected in 3D PDMS-GR (CCF 0.66 ± 0.04; n = 13 fields), indicative of a higher synchronization among active neurons when interfaced to graphene in the third dimension. All these results suggest an increased neuronal excitability or diverse paths of neuronal interconnection, for example displaying a lower synaptic inhibition, when neurons are interfaced to graphene in 3D constructs.

In neuronal circuits, the ratio of excitatory and inhibitory inputs to a cell usually regulates the balance between excitation and inhibition. To gain insights into the GABAergic inhibitory control of the neural circuits developed in the two 3D scaffolds, we compared network activity upon pharmacological block of $GABA_A$ receptors by bicuculline (10 µM) application. In neural networks, the removal of GABAergic synaptic component is known to alter the emerging activity patterns,[2,36,37] leading to a more intense and regular bursting.[2,35,38] Figure 3A (right dotted traces), shows samples of fluorescence tracings of active cells in the

presence of bicuculline (similar results were obtained by gabazine applications, see methods). As expected, regular Ca^{2+} events were detected in both culturing groups, characterized by IEI of 8.0 ± 0.05 s in 3D PDMS cultures (n = 218 cells), a value significantly (*** $p < 0.001$; Kolmogorov-Smirnov test) lower when compared to that of 3D PDMS-GR 14.2 ± 0.2 s, n = 175 cells; all data summarized in the cumulative distribution in Figure 3B, right plot). Disinhibited activity was defined, in both groups, by comparable, although higher than in control, CCF values (3D PDMS CCF 0.75 ± 0.03; 3D PDMS-GR 0.81 ± 0.03, data not shown), strengthening the hypothesis that the higher calcium episodes occurrence in standard saline solutions when 3D PDMS-GR cultures are compared to 3D PDMS, might indicate a diverse contribution of the GABAergic drive to the network activity in the two groups.

To ascertain whether the observed changes in network dynamics emerged from the sole presence of graphene, independently from the 3D growth conditions, hippocampal cultures were grown on flat coverslips covered by a thin layer of graphene flakes (2D GR, see Methods) and the emerging activity was compared to cells grown on flat glass coverslips (CTRL). In standard saline solution, we detected 44% spontaneously active cells in 2D control conditions, increased to 52% in 2D GR. Figure 4A (left) shows representative visual fields of fluorescent cells and representative fluorescent tracings (right) of spontaneous and bicuculline-induced neuronal activity (dotted traces) recorded from 2D CTRL (top) and 2D GR (bottom) cultures. When we measured Ca^{2+} activity, the IEI was significantly (*** $p < 0.001$; Kolmogorov-Smirnov test) lower in 2D GR cultures (9.2 ± 0.16 s, n = 185 cells, from 3 different series of cultures) when compared to control ones (14.7 ± 0.28 s, n = 232 cells, from 3 different series of cultures; see cumulative distributions in Figure 4B, left plot), in line with the reported increase in neuronal activity when cultures grow interfaced to single-layer

graphene.[8] The trend in terms of IEI in 2D graphene was preserved also in the presence of bicuculline (13.4 ± 0.09 s, n = 258 cells, control; 7.4 ± 0.07 s, n = 197 cells, 2D GR; ***p < 0.001; see cumulative distribution in Figure 4B, right plot). These results suggest that neurons when interfaced to graphene increased their activity but, differently from the 3D condition, the inhibitory control of the network was unaltered by graphene interfacing.

To acquire a better understanding of our observations, we investigated whether the 3D PDMS-GR scaffolds affected the development of inhibition in resulting 3D neuronal circuits by considering two hypotheses. First, graphene might have changed the ratio of excitatory to inhibitory neurons altering the expression of the GABAergic neuronal phenotype. To validate this possibility 3D cultures developed inside 3D PDMS and 3D PDMS-GR scaffolds were co-immunostained with β-tubulin III and anti-GABA and processed by confocal microscopy (Figure 5A left and right images, respectively). By quantifying the percentage of double positive cells, i.e. GABAergic neurons, for the two conditions we discovered that the two values were similar for 3D PDMS (40.3%, n = 27 visual fields, from 4 different series of cultures) and for 3D PDMS-GR (43.2%, n = 25 visual fields, from 4 different series of cultures; summarized in the bar plot of Figure 5B).

The second hypothesis we investigated was that 3D PDMS-GR could have affected the maturation of GABAergic inhibition via tuning chloride ion fluxes through GABAA receptors. It is in fact well known that during CNS development, neuronal intracellular chloride concentration shifts from higher to lower values (with respect to the extracellular one), modulating the amplitude of GABAergic currents.[39,40] In accordance, in immature neurons, $GABA_A$ receptors activation may result in a depolarization contributing to network bursting.[41] We performed chloride imaging using a quinoline-based Cl^- indicator dye: MQAE (N-[6-methoxyquinolyl] acetoethyl ester).[8,42] Figure 6A shows representative visual fields

of MQAE-labeled neurons, in 3D PDMS (left) and 3D PDMS-GR (right) cultures. As shown in Figure 6B (tracings from 2 representative cells), when GABA (10 mM; 10÷20 s) is applied to 9÷11 DIV cultures, efflux or influx of Cl^- are induced in the neurons, depending on their maturation, resulting in opposite changes in the Cl^- sensitive MQAE fluorescence.[8] In all imaged fields (n = 13 for both condition), cells displaying opposite directions of GABA-evoked Cl^- fluxes were detected, thus confirming that immature and mature GABAergic phenotypes coexist within the same network. Anyhow, as shown in the plot of Figure 6B, the majority of neurons inside the 3D PDMS responded to GABA applications with a Cl^- influx, resulting in a decreased fluorescence signal due to dye quenching (plain trace at the bottom) while the opposite condition was observed in neurons developed interfaced to the graphene within 3D PDMS-GR scaffolds (dotted line at the top, striped part of the histograms on the right).

3. Discussion

In basic neuroscience, 2D cultures represent a powerful platform that has allowed unraveling the mechanistic features of neurons and synapses, yet they are limited tools when investigating the role of circuit topology on networks dynamics, for example when neuronal branches are exposed to the 3-dimensional space.[2,3] Besides, 3D platforms, when compared to 2D ones, were shown to impact neuronal differentiation,[9,43,44] cell and axonal growth,[45,46] circuit functional organization and synaptic network synchronization.[2] Further engineering of 3D scaffolds into CNS regenerative interfaces may be pursue by the use of nanomaterials, such as carbon-based ones, to improve the device electrical conductivity and to favor the development of excitable tissue.[7,22,47-49] Here, we exploit elastomeric 3D platforms to investigate the impact on network dynamics of posing at the interface few-layer graphene, known to affect cell signaling when supporting 2D cultures.[8] The macroscopic stiffness of the three-dimensional scaffolds we have fabricated was about 60

kPa, not so far from compliance values of rodent and human brains (Young's moduli falling in the range of 0.1÷20 kPa).[50] The extremely high values of resistivity of the 3D PDMS-GR scaffold (in the MΩ·mm range, at best) despite the presence of few-layers graphene flakes (whose electrical resistivity is in the order of 10–6 Ω·mm)[51,52] may result from the combined effects of the large contact resistances taking place between contiguous graphene flakes and the fact that graphene is not distributed in bulk inside the PDMS but it is randomly distributes on the scaffold's facets. The latter point implicates that the flat gold electrodes we used to electrically characterize the material have a minimal contact area with graphene being, in the majority, in contact with PDMS, that is an insulator. Importantly, cells inside the scaffold developed in contact to the graphene flakes, consequently they locally experienced the intrinsic low resistivity of this nanomaterial. This supposition is supported by the perturbation of neuronal network electrical activity we observed that is very similar to the effect induced on neuronal cells by single layer graphene.[8]

We successfully reconstructed neuronal networks inside 3D PDMS and 3D PDMS-GR. In both growth conditions neurons and GFAP-positive cells percolated the thickness of the scaffolds, generating healthy 3D networks of comparable size in the two constructs,[2] being hippocampal cell densities and the neuron to glia ratio not affected by graphene layering. By live calcium imaging we simultaneously monitor the activity of small groups of neurons. We detect episodes of intracellular calcium rise to measure the occurrence of neuronal and synaptic activity, a notion supported by TTX experiments.[2] In 3D constructs, neuronal calcium episodes are usually due to brief synchronous firing, leading to transient synchronization of synaptic events.[2,5] These bursts are accepted index of network dynamics,[2,35] even in the absence, in calcium imaging, of single action potential or individual synaptic currents resolution. The 3D architecture of synaptic connections sustained a high

rate of bursting in 3D PDMS, confirming previous results where we postulated that 3D networks topology favors neuronal connectivity efficiency.[2] Spontaneous bursting was further increased in 3D PDMS-GR, potentially due to higher neuronal excitability or augmented neuronal connectivity, given the substantial similarities in network size with or without graphene. Indeed, 2D monoatomic layer of graphene was shown to improve cellular excitability via tuning the distribution of extracellular ions at the interface with neurons, leading to cell biophysical changes.[8] In accordance, in our experiments with 2D graphene, the up-scaled circuit excitability was observed in active cells involved in spontaneous and disinhibited bursting. On the contrary, the similar probability of finding spontaneously active neurons among 3D PDMS and 3D PDMS-GR fields does not support a mere increase in cell excitability or in neuronal connectivity,[2,53] and the slower pace of disinhibited rhythms in the presence of graphene is more suggestive of adaptive changes in the excitation/inhibition ratio, potentially following graphene interfacing in 3D configurations. We thus favor an alternative hypothesis, where the combination between synapse formation under 3D architecture and graphene interfaces affected the maturation of GABAergic inhibition, tuning the balance between hyperpolarizing and depolarizing responses, the latter acting in synergy with glutamate and potentially contributing to network synchronization,[41] in the absence of changes in GABAergic phenotype expression.

Physical interactions between cells and the artificial materials on which they grow may influence biological behaviors and trigger growth, maturation or differentiation.[22,47-49,54] In the case of 3D PDMS-GR the mechanisms responsible for the (slight) network redistribution of inhibition maturation are not known, and might include a complex interplay of mechanical, chemical and electrical cues imposed by graphene when cells are able to grow in the third dimension. Regardless the need of future mechanistic studies resolving the

effects of few-layer graphene in 3D constructs, our report suggests the importance of controlling the physicochemical properties of 3D scaffolds for the successful specialized guidance of neural network formation and function.

4. Conclusion

In this work we exploited material science strategies to manufacture 3D scaffolds enabling the formation of neuronal circuits in the third dimension. We further introduced, by a simple and reproducible procedure, graphene flakes to interface neurons within the three dimensional structures. Innovative methods to introduce graphene in interfacing devices may improve long-term stability of ultra-sensitive electronic devices. On the other hand, graphene and graphene-based materials are attractive nanoplatforms for regenerative medicine approaches in neural tissue injury. Within this framework, we describe the ability of graphene to modulate neuronal circuit formation when interfaced in the third dimension. The possibility to govern cell neurobiology by nanomaterials physical and topographical properties can be of interest in future 3D regenerative interfaces for long term medical developments.

5. Experimental Section

Graphene preparation and characterization

Graphene used for the scaffold preparation was obtained by a ball-milling protocol, as previously described.[25] Briefly, 7.5 mg of graphite (Bay Carbon, Inc. – USA) and 22.5 mg of melamine (Sigma-Aldrich), were ball-milled at 100 rpm for 30 minutes using a Retsch PM 100 planetary mill (Retsch Technology GmbH, Germany) under air atmosphere. The resulting solid was dispersed in water (20 mL), obtaining a dark suspension. Melamine was afterwards

removed by washing with hot water and a precipitate consisting in poorly exfoliated graphite was removed from the liquid fraction after stabilization for 5 days.

The obtained graphene was subsequently fully characterized by thermogravimetric analysis (TGA), Raman spectroscopy and transmission electron microscopy (TEM) techniques. TGA was performed at 10 ºC min-1 under nitrogen flow using a TGA Q50 (TA Instruments). About 20 graphene samples were analyzed by Raman spectroscopy using a Renishaw inVia Raman microspectrophotometer. The laser wavelength and the objective used were 532 nm and 100×, respectively. The morphology and the lateral size of so obtained graphene flakes were obtained by a Jeol JEM 1011 transmission electron microscope and analyzed using ImageJ open-source software to calculate sheets dimensions.[55]

Samples fabrication and characterization

Flat glass control (CTRL) substrates were commercial glass coverslips (12x24 mm^2) cleaned in “piranha solution” (H2SO4:H2O 3:1, 100 mL for 50 coverslips) at 90 °C for 16 hours. Before use samples were carefully rinsed with deionized water and let to dry in an oven at 80 °C overnight.

Flat graphene samples (2D GR) were prepared depositing by spray-coating a thin homogeneous film of few-layers graphene flakes on glass control substrates (see Supplementary Figure 1). Briefly, substrates were placed on a hot plate at 100 °C and were sprayed with an ethanol dispersion of graphene flakes (0.05 mg/mL) using a Junior 140 air brush (SAGOLA, Spain) until reaching a sheet resistance of about 150 kOhm/□. The distance between the air brush and the plate was around 20 cm and the nitrogen pressure used to spray was 2 bars. The substrates were then placed in an oven at 350 °C for 20 minutes to remove any trace of solvent. Finally, sheet resistance and transmittance (550 nm) were measured using a 34461A Agilent Bench Multimeter (Agilent Technologies, Inc - US) and a

Cary 5000 UV-Vis-NIR spectrophotometer (Agilent Technologies, Inc - US), obtaining final graphene films with an average sheet resistance of 30.4 kOhm/□ and an average transmittance of 37%. Scanning electron microscopy was performed using a Philips XL30 system after samples were coated with a 3 nm layer of gold (Figure S1).

Self–standing elastomeric scaffolds (3D PDMS-GR) with all facets decorated with flakes of graphene were obtained by shaking overnight and in dry conditions a mixture of graphene (30 mg) and sucrose (500 mg, sieved in order to have a granulometry of 125÷250 µm). Subsequently, 20 µL of deionized water were added and mixed, obtaining a homogeneously wet mixture. The mixture was molded into the desired shape (a 5 mm edge cube), gently pressed and dried at 60 °C. Polydimethylsiloxane (PDMS – SYLGARD® 184 Silicone Elastomer from Dow Corning) was prepared and layered with a thickness of 5 mm in a glass dish. The sugar/graphene solid conglomerate was placed onto the dish and was infiltrated under vacuum with PDMS. The cubes were then cured in an oven at 85 °C for 1 hour and cooled at room temperature. PDMS excess was trimmed away and the cube was dipped in distilled water in order to dissolve the sugar. 3D PDMS control samples were prepared following the same protocol but in the absence of graphene.

Elastomeric scaffold containing few-layer graphene was further characterized by Raman spectroscopy. Raman spectra of 3D PDMS-GR were recorded with an InVia Renishaw microspectrometer equipped with a 532 nm point-based laser. Power density was kept in all cases below 5 mW/µm^2 to avoid laser-over heating effects. The obtained spectra were a result of probing 25 random locations on the sample. Three-dimensional Raman mappings were performed with the 532 nm laser by using the line-based option (streamline), which analyzed rectangular slices of sample and depth steps of 1 µm until reaching 10 µm allowing to map the G-band intensities in three dimensions. 3D PDMS and 3D PDMS-GR scaffold

morphologies were evaluated by means of scanning electron microscopy (SEM) imaging. Images were collected on a Gemini SUPRA 40 SEM (Carl Zeiss GmbH, Germany) collecting secondary electrons mounting 250 µm thick slices of the bare scaffolds with conductive carbon tape (Ted Pella, Inc., USA). Images were acquired at 2.5 keV accelerating voltage. Before SEM characterization both samples were Au metalized with a metal sputter coater (Polaron SC7620). For the mechanical characterization of the 3D PDMS-GR microporous scaffold we performed compressive test. In this, we used cubic samples with a dimension of 5 mm in side. Tests were performed taking advantage of a Galdabini SUN 500 uniaxial microcompression apparatus. Scaffolds were compressed between two circular (20 mm in diameter) flat surfaces using a high sensitivity load cell for data acquisition (CTCA10K5, AEP Transducers, Italy). All tests were done in air at room temperature. Before starting the test, a 50 mN preload was applied to the sample to ensure a good contact between the sample and the two pressing surfaces. 10 µm/s constant speed loading cycle was used with a final load limit fixed at 1 N. Final compressive displacement was about 2 mm (40%). Each representative stress-strain curve was obtained by averaging the results from at least 5 measurements. Sample stiffness was determined as Young's Modulus (E) evaluating the slope of the linear portion of the stress-strain curve (roughly from 10% to 25% deformation). Graphene-based scaffold electrical characteristic was studied placing a 5 mm side size cube of the 3D PDMS-GR scaffold between the two conductive coplanar flat electrodes (10×10 mm^2) of a home-made device. The sample was initially squeezed between the two electrodes with a constant 50 mN load in order to assure optimal contact. Resistivity was assessed using a low current source-meter (KEITHLEY 2601A System SourceMeter) at an applied bias voltage of about 20 V. The dependency of the resistance upon deformation was determined at steps of 10% up to 60% total deformation. All electrical measurements were

carried out at room temperature, in air. The deformation dependent resistivity plot was obtained by averaging the results from 3 different samples and was calculated from resistance via scaffold's geometrical characteristics.

Cell Culture Preparation

Isolation of primary hippocampal tissue was operated in agreement with the guidance of the National Institutes of Health and with the proper international and institutional standards for the care and use of animals in research (Italian Ministry of Health, in agreement with the EU Recommendation 2007/526/CE). All procedures were approved by the local veterinary authorities and performed in accordance with the Italian law (decree 26/14) and the UE guidelines (2007/526/CE and 2010/63/UE). The animal use was approved by the Italian Ministry of Health. All efforts were made to reduce the number of animals used and to minimize animal suffering. All the reagents were purchased from Sigma-Aldrich if not otherwise indicated. Dissociated hippocampal cultures were prepared from postnatal 2÷3 days old (P2÷P3) Wistar rats as previously reported.[2,30] Cells were plated on four distinct substrates: poly-L-ornithine coated glass coverslips (CTRL) and graphene flakes coated glass coverslips (2D GR) or on pristine three-dimensional scaffolds (3D PDMS) and three-dimensional, graphene functionalized, scaffolds (3D PDMS-GR). 3D scaffolds were sliced with a thickness of about 400 µm and then mounted on the glass coverslips using a slight adhesive PDMS layer cured for 1 hour at 120 °C.[2,9] One-hour prior to cell plating, in order to promote cell adhesion, 2D GR, 3D PDMS and 3D PDMS-GR samples were exposed to low-pressure air plasma (Harrick PDC-32G Plasma Cleaner) for 5 minutes at room temperature (20÷22 °C) and finally sterilized with ultraviolet (UV) radiations for 20 minutes.[2] Cultures were incubated at 37 °C, 5% CO_2 in a culture medium consisting of MEM (Gibco) containing 35 mM glucose (Carlo Erba Reagents), 15 mM HEPES, 1 mM Apo-

Transferrin, 48 mM Insulin, 3 mM Biotin, 1 mM Vitamin B12. 500 nM Gentamicin (Gibco) was also added to prevent contaminations. Half of the culture medium was renewed two days after seeding and then changed every two days. Cultures were grown for 9÷11 days in vitro (DIV) and then used for experiments.[2]

Immunofluorescence

Cells cultured in 3D PDMS and 3D PDMS-GR Scaffolds were fixed in 4% formaldehyde (prepared from fresh paraformaldehyde) in PBS 1× for 30 minutes and 1% glutaraldehyde for 1 hour for GABA staining, as previously reported.[56] Cultures were permeabilized for 45 min with 0.3% Triton-X-100 (Carlo Erba) in PBS and subsequently incubated with primary antibodies for 45 minutes at RT. After been washed, samples were finally incubated with secondary antibodies for 45 minutes. Samples were mounted with anti-fade medium Fluoromount on 1 mm thick microscope glass slides. Neurons were stained with rabbit anti-β-tubulin III primary antibody (1:500 dilution) and visualized with Alexa® 594 goat anti-rabbit as secondary antibody (1:500, Invitrogen). Astrocytes were labeled with mouse anti-GFAP primary antibodies (1:250) and visualized with Alexa® 488 anti-mouse in goat as secondary antibody (1:500, Invitrogen).

For GABA immunostaining we used mouse anti-β-tubulin III (1:500) and rabbit anti-GABA (1:300 dilution) as primary antibodies while Alexa® 594 goat anti-mouse (1:500) and Alexa® 488 goat anti-rabbit (1:500 dilution) as secondary antibodies. Nuclei were stained in all conditions with 4',6-diamidino-2-phenylindole (DAPI, 1:200, Invitrogen). Graphene was visualized by reflection mode during the confocal acquisition.[57,58] To evaluate the density of neurons and astrocytes, images of immunolabeled 3D cultures were acquired using an inverted confocal Microscope (Nikon Eclipse Ti, Nikon, Japan) with a 20× objective (0.5 NA, PlanFluor, Nikon, Japan) and serial confocal planes (z-stack) were acquired every 1 µm across

the entire 3D sections. Moreover, to quantify the percentage of GABA-positive neurons, images were acquired with 40× objective (0.75 NA, PlanFluor, Nikon, Japan; z-stack every 500 nm) from randomly selected fields, and GABA-positive neurons were counted. This value was then normalized to the overall number of neurons (β-tubulin III positive cells) for each field. Analysis and images reconstruction were accomplished using open-source ImageJ software.[55]

Live cell imaging

For Calcium (Ca^{2+}) imaging experiments, hippocampal cultures were loaded with cell permeable Ca^{2+} indicator Oregon Green 488 BAPTA-1 AM (Molecular Probes): to the dye stock (50 µg), 10 µL of DMSO was added and dissociated cultures were incubated for 45 min at 37 °C, 5% CO_2 at a final concentration of 4 µM. Subsequently samples were placed in a recording chamber mounted on an inverted microscope (Nikon Eclipse Ti-U) and continuously perfused at RT and at 5 mL/min with a recording solution of composition (mM): 150 NaCl, 4 KCl, 2 $CaCl_2$, 1 $MgCl_2$, 10 HEPES, 10 glucose (pH adjusted to 7.4 with NaOH; osmolarity 300 mOsm). The Oregon Green loaded cultures were observed with a 20× objective (PlanFluor, 0.45 NA, Nikon, Japan) using an ORCA-Flash 4.0 V2 sCMOS camera (Hamamatsu). Images were acquired at a sampling rate of 6.67 Hz (150 ms exposure time) under continuous illumination. The camera was set to operate at 512×512 pixels. The Ca^{2+} dye was excited at 488 nm using an appropriate filters/dichroic cube set and a mercury (Hg) lamp (Nikon Intensilight). The excitation light was attenuated by neutral density filters (ND 32). Images from collected light were acquired by an integrating imaging software package (HCImage Live, Hamamatsu). After recording the spontaneous activity of hippocampal neurons for 10÷15 minutes, 10 µM bicuculline or 10 µM gabazine (both $GABA_A$ antagonist) were applied to the bath for 20 minutes. At the end of each experiments, 1 µM TTX (a

voltage-gated, fast Na^+ channel blocker; Latoxan) was added to the recording solution to confirm the neuronal nature of the recorded signals. For each sample we recorded, from each field, individual (not overlapping or interfering) 30 ± 12 cells by drawing regions of interest (ROIs) around clearly recognizable cell bodies. The corresponding light intensity traces were analyzed with Clampfit software (pClamp suite, 10.4 version; Axon Instruments) in off-line mode and with Igor Pro Software (6.32 A version; WaveMetrics, Lake Oswego, Oregon, USA). We then computed the difference between consecutive onset times, to obtain the inter-event interval (IEI). Once we obtained the IEI values from each active cell in the field, data were pooled for all fields recorded under the same experimental conditions and averaged for further comparison. Intracellular Ca^{2+} transients were expressed as fractional amplitude increase ($\Delta F/F_0$, where F_0 is the baseline fluorescence level and ΔF is the rise over baseline); we determined the onset time of neuronal activation by detecting those events in the fluorescence signal that exceed at least five times the standard deviation of the noise.[2] The values of cross correlation function (CCF) were evaluated using a home-made procedure in Igor Pro and used to measure the strength of the correlation between cells, i.e. the relative probability that the peaks of calcium transients took place at the same time in all the cells of a certain field. For chloride imaging, hippocampal dissociated cultures grown within 3D scaffolds were loaded with the fluorescent chloride indicator MQAE (N-[6-methoxyquinolyl] acetoethyl ester, 1 mM final concentration, from Abcam) diluted in the recording solution for 10 minutes at 37 °C.[42] After 10 min washes, each sample was placed in a recording chamber mounted on an inverted microscope (Nikon Eclipse Ti-U) and observed with a 60× objective (0.7 NA, PlanFluor, Nikon, Japan). Samples were continuously perfused at RT and at 5 mL/min with a recording solution (see above the composition). Images were acquired using an ORCA-Flash 4.0 V2 sCMOS camera (Hamamatsu) for 1 minute

at 5 Hz (200 ms exposure time), the fluorescent chloride indicator was excited at the 365 nm Hg peak using a UV-2A Nikon filter set; excitation light was attenuated by a neutral density filter (ND 16). The imaging system was controlled by the integrating imaging software (HCImage Live, Hamamatsu) and the camera was set to operate on 1024 × 1024 pixels. After 5 seconds from the beginning of the recording, 10 mM GABA was bath-applied for 20 seconds in order to evoke chloride influx/efflux through the membrane.

Image time stacks were analyzed in selected ROI to evaluate the variations in MQAE fluorescence intensity. Images were analyzed by ImageJ software (NIH) and the corresponding traces were studied with Clampfit software (pClamp suite, 10.4 version; Axon Instruments) in off-line mode and with Igor Pro Software (6.32 A version; WaveMetrics, Lake Oswego, Oregon, USA). Intracellular Cl^- transients were expressed as fractional amplitude variations ($\Delta F/F_0$) and selected only when exceeding at least five times the standard deviation of the noise.[8]

Statistical Analysis

All values from samples subjected to the same experimental protocols were pooled together and expressed as mean ± s.e.m., with n = number of cells, if not otherwise indicated. D'Agostino & Pearson omnibus normality test was applied to evaluate the statistical distribution of the data sets. Statistically significant difference between two data sets was assessed by Student's t-test for parametric data and by Mann-Whitney or Kolmogorov-Smirnov test for non-parametric ones. Statistical significance was determined at $p<0.05$, unless otherwise indicated. Significance was graphically indicated as follows: * $p<0.05$, ** $p<0.01$, and *** $p<0.001$.

Supporting Information: Figure S1

Acknowledgements

We are especially grateful to Micaela Gandolfo for supervising the confocal image reconstruction, to Livia Piatti and Gianluca Turco for characterizing the material compressibility. IOM-TASC national laboratory (Trieste) is also gratefully acknowledged for SEM assistance. We also wish to thank the IRICA Institute for the use of their shared equipment, services and expertise.

Author Contributions

The manuscript was written through contributions of all authors. All authors have given approval to the final version of the manuscript.

Present Address

† Department of Biomedical Engineering, Tel Aviv University, Tel Aviv 69978, Israel

Cell Biology Department, Duke University Medical Center, Durham 27710, North Carolina, USA

Funding Sources.

We acknowledged financial support from the European Union's Horizon 2020 research and innovation program under Grant Agreements 696656 and 785219 Graphene Flagship. This work was also supported by the Spanish Ministry of Economy and Competitiveness MINECO (projects CTQ2017-88158-R and CTQ2016-76721-R), by the University of Trieste, and

Consorzio Interuniversitario Nazionale per la Scienza e Tecnologia dei Materiali (INSTM). MP, as the recipient of the AXA Chair, is grateful to the AXA Research Fund for financial support. This work was performed under the Maria de Maeztu Units of Excellence Program from the Spanish State Research Agency – Grant No. MDM-2017-0720

Received: ((will be filled in by the editorial staff))
Revised: ((will be filled in by the editorial staff))
Published online: ((will be filled in by the editorial staff))

References

[1] A. Gladkov, Y. Pigareva, D. Kutyina, V. Kolpakov, A. Bukatin, I. Mukhina, V. Kazantsev, A. Pimashkin, *Sci Rep*. 2017, *7*, 15625.

[2] S. Bosi, R. Rauti, J. Laishram, A. Turco, D. Lonardoni, T. Nieus, M. Prato, D. Scaini, L. Ballerini, *Sci. Rep*. 2015, *5*, 9562

[3] F. P. Ulloa Severino, J. Ban, Q. Song, M. Tang, G. Bianconi, G. Cheng, V. Torre, *Sci. Rep*. 2016, 29640

[4] E. R. Aurand, S. Usmani, M. Medelin, D. Scaini, S. Bosi, F. B. Rosselli, S. Donato, G. Tromba, M. Prato, L. Ballerini, *Adv. Funct. Mater*. 2018, *28*, 1700550

[5] G. Cellot, E. Cilia, S. Cipollone, V. Rancic, A. Sucapane, S. Giordani, L. Gambazzi, H. Markram, M. Grandolfo, D. Scaini, F. Gelain, L. Casalis, M. Prato, M. Giugliano, L. Ballerini, *Nat. Nanotechnol*. 2009, *4*, 126-33

[6] G. Cellot, F. M. Toma, Z. K. Varley, J. Laishram, A. Villari, M. Quintana, S. Cipollone, M. Prato, L. Ballerini, *J. Neurosci*. 2011, *31*, 12945-12953

[7] I. Rago, R. Rauti, M. Bevilacqua, I. Calaresu, A. Pozzato, M. Cibinel, M. Dalmiglio, C. Tavagnacco, A. Goldoni, D. Scaini, *Adv. Biosys*. 2019, *3*, 1800286

[8] N. P. Pampaloni, M. Lottner, M. Giugliano, A. Matruglio, F. D'Amico, M. Prato, J. A. Garrido, L. Ballerini, D. Scaini, *Nat. Nanotechnol*. 2018, *13*, 755-764

[9] C. Martín, S. Merino, J. M. González-Domínguez, R. Rauti, L. Ballerini, M. Prato, E. Vázquez, *Sci. Rep*. 2017, *7*, 10942

[10] V. C. Sanchez, A. R. Jachak, H. Hurt, A. B. Kane, *Chem. Res. Toxicol*. 2012, *25*, 15-34

[11] K. Kostarelos, K. S. Novoselov, *Science* 2014, *344*, 261-263

[12] H. Y. Mao, S. Laurent, W. Chen, O. Akhavan, M. Imani, A. A. Ashkarran, M. Mahmoudi, *Chem. Rev*. 2013, *113*, 3407-3424

[13] M. C. Serrano, J. Patiño, *et al*., *J. Mater. Chem. B*. 2014, *2*, 5698-5706

[14] L. Yichen, L. Xin, H. Ryoma, R. Chi, Z. Xingwang, K. Takaki, K. Duygu, *Adv. Funct. Mater*. 2018, *28*, 1800002.

[15] N. Li, X. Zhang, Q. Song, R. Su, Q. Zhang, T. Kong, L. Liu, G. Jin, M. Tang, G. Cheng, *Biomaterials* 2011, *32*, 9374-9382

[16] Q. Song, Z. Jiang, N. Li, P. Liu, L. Liu, M. Tang, C. Cheng, *Biomaterials* 2014, *35*, 6930-6940

[17] R. Rauti, M. Medelin, L. Newman, S. Vranic, G. Reina, A. Bianco, M. Prato, K. Kostarelos, L. Ballerini, *Nano Lett*. 2019, *19*, 2858-2870

[18] M. Tang, Q. Song, N. Li, Z. Jiang, R. Huang, G. Cheng, *Biomaterials* 2013, *34*, 6402-6411

[19] D. Bitounis, H. Ali-Boucetta, B. H. Hong, D. H. Min, K. Kostarelos, *Adv. Mater*. 2013, *25*, 2258-2268

[20] D. Kuzum, H. Takano, E. Shim, J. C. Reed, H. Juul, A. G. Richardson, J. de Vries, *et al*., *Nat. Commun*. 2014, *5*, 5259

[21] E. Masvidal-Codina, X. Illa, M. Dasilva, A. B. Calia, T. Dragojević, E. E. Vidal-Rosas, E. Prats-Alfonso, *et al*., *Nat. Mater*. 2019, *18*, 280-288.

[22] R. Rauti, M. Musto, S. Bosi, M. Prato, L. Ballerini, *Carbon* 2019, *143*, 430-446

[23] N. Li, Q. Zhang, S. Gao, Q. Song, R. Huang, L. Wang, L. Liu, J. Dai, M. Tang, G. Cheng, *Sci Rep*. 2013, *3*, 1604.

[24] A. Domínguez-Bajo, A. González-Mayorga, C. R. Guerrero, F. J. Palomares, R. García, E. López-Dolado, M. C. Serrano, *Biomaterials* 2019, *192*, 461-474

[25] V. León, J. M. González-Domínguez, J. L. Fierro, M. Prato, E. Vázquez, *Nanoscale* 2016, *8,* 14548-14555

[26] C. Casiraghi, A. Hartschuh, H. Qian, S. Piscanec, C. Georgi, A. Fasoli, K. S. Novoselov, D. M. Basko, A. C. Ferrari, *Nano Lett*. 2009, *9*, 1433-1441

[27] K. R. Paton, E. Varrla, C. Backes, R. J. Smith, U. Khan, A. O'Neill, C. Boland, M. Lotya, *et al*., *Nat. Mater*. 2014, *13*, 624-630

[28] U. Mogera, R. Dhanya, R. Pujar, C. Narayana, G. U. Kulkarni, *J. Phys. Chem. Lett*. 2015, *6*, 4437-4443

[29] D. Cai, A. Neyer, R. Kuckuk, H. M. Heise, *Journal of Molecular Structure*, 2010, *976*, 274-281

[30] R. Rauti, N. Lozano, V. León, D. Scaini, M. Musto, I. Rago, F. P. Ulloa Severino, *et al*., *ACS Nano*. 2016, *10*, 4459-4471

[31] A. Càceres, G. A. Banker, L. Binder, *J. Neurosci*. 1986, *6*, 714-722

[32] N. J. Willmott, K. Wong, A. J. Strong, *FEBS Lett*. 2000, *487*, 239-247

[33] A. Fabbro, A. Villari, J. Laishram, D. Scaini, F. M. Toma, A. Turco, M. Prato, L. Ballerini, *ACS Nano* 2012, *6*, 2041-2055

[34] E. Marconi, T. Nieus, A. Maccione, P. Valente, A. Simi, M. Messa, S. Dante, P. Baldelli, L. Berdondini, F. Benfenati, *PLoS One* 2012, *7*, e34648

[35] O. Stetter, D. Battaglia, J. Soriano, T. Geisel, *PLoS Comput. Biol*. 2012, *8*, e1002653

[36] D. M. Sokal, R. Mason, T. L. Parker, *Neuropharmacology* 2000, *39*, 2408-2417

[37] E. Tibau, M. Valencia, J. Soriano, *Front. Neural Circuits* 2013, *7*, 1-16

[38] A. Fabbro, B. Pastore, A. Nistri, L. Ballerini, *Cell Calcium* 2007, *41*, 317-329

[39] D. Arosio, G. M. Ratto, *Front. Cell. Neurosci*. 2014, *8*, 258

[40] E. Cherubini, *Int. J. Dev. Neurosci*. 1990, *8*, 481-490

[41] G. Cellot, L. Maggi, M. A. Di Castro, M. Catalano, R. Migliore, M. Migliore, M: L. Scattoni, G. Calamandrei, E. Cherubini, *Sci. Rep*. 2016, *6*, 31696

[42] N. Marandi, A. Konnerth, O. Garaschuk, *Pflug. Arch*. 2002, *445*, 357-365

[43] Y. Lee, J. M. Lee, P. K. Bae, I. Y. Chung, B. H. Chung, B. G. Chung, *Electrophoresis* 2015, *36*, 994-1001

[44] P. Moshayedi, L. R. Nih, I. Llorente, A. R. Berg, J. K. Cinkornpumin, W. E. Lowry, T. Segura, S. T. Carmichael, *Biomaterials* 2016, *105*, 145-155

[45] T. B. Puschmann, Y. de Pablo, C. Zanden, J. Liu, M. A. Pekny, *Tissue Eng. Part C*, 2014, *20*, 485-493

[46] S. Usmani, E. R. Aurand, M. Medelin, A. Fabbro, D. Scaini, J. Laishram, F. B. Rosselli, *et al*., *Sci. Adv*. 2016, *2*, 1600087

[47] T. Dvir, B. P. Timko, M. D. Brigham, S. R. Naik, S. S. Karajanagi, O. Levy, H. Jin, K. K. Parker, R. Langer, D. S. Kohane, *Nat Nanotechnol*. 2011, *6*, 720-5

[48] S. Marchesan, L. Ballerini, M. Prato, *Science* 2017, *356*, 1010-1011

[49] S. Scaini, L. Ballerini, *Curr. Opin. Neurobiol*. 2018, *50*, 50-55

[50] W. J. Tyler, *Nat. Rev. Neurosci*. 2012, *13*, 867–878

[51] N. Rouhi, Y. Y. Wang, P. J. Burke, *Appl. Phys. Lett*. 2012, *101*, 263101

[52] A. N. Sruti, K. J. Jagannadham, *Electron. Mater*. 2010, *39*, 1268-1276

[53] F. Aguado, M. A. Carmona, E. Pozas, A. Aguiló, F. J. Martínez-Guijarro, S. Alcantara, V. Borrell, R. Yuste, C. F. Ibañez, E. Soriano, *Development*. 2003, *130*, 1267-80

[54] K. Kenry; W. C. Lee, K. P. Loh, C. T. Lim, *Biomaterials* 2018, *155*, 236-250

[55] C. A. Schneider, W. S. Rasband, K. W. Eliceiri, *Nat. Methods*. 2012, *9*, 671-675

[56] F. Furlan, G. Taccola, M. Grandolfo, L. Guasti, A. Arcangeli, A. Nistri, L. Ballerini, *J. Neurosci*. 2007, *27*, 919-928

[57] M. Bramini, S. Sacchetti, A. Armirotti, A. Rocchi, E. Vázquez, V. León Castellanos, T. Bandiera, F. Cesca, F. Benfenati, *ACS Nano* 2016, *10*, 7154-7171

[58] M. Musto, R. Rauti, A: F. Rodrigues, E. Bonechi, C. Ballerini, K. Kostarelos, L. Ballerini, *Front. Syst. Neurosci*. 2019, *13*,1

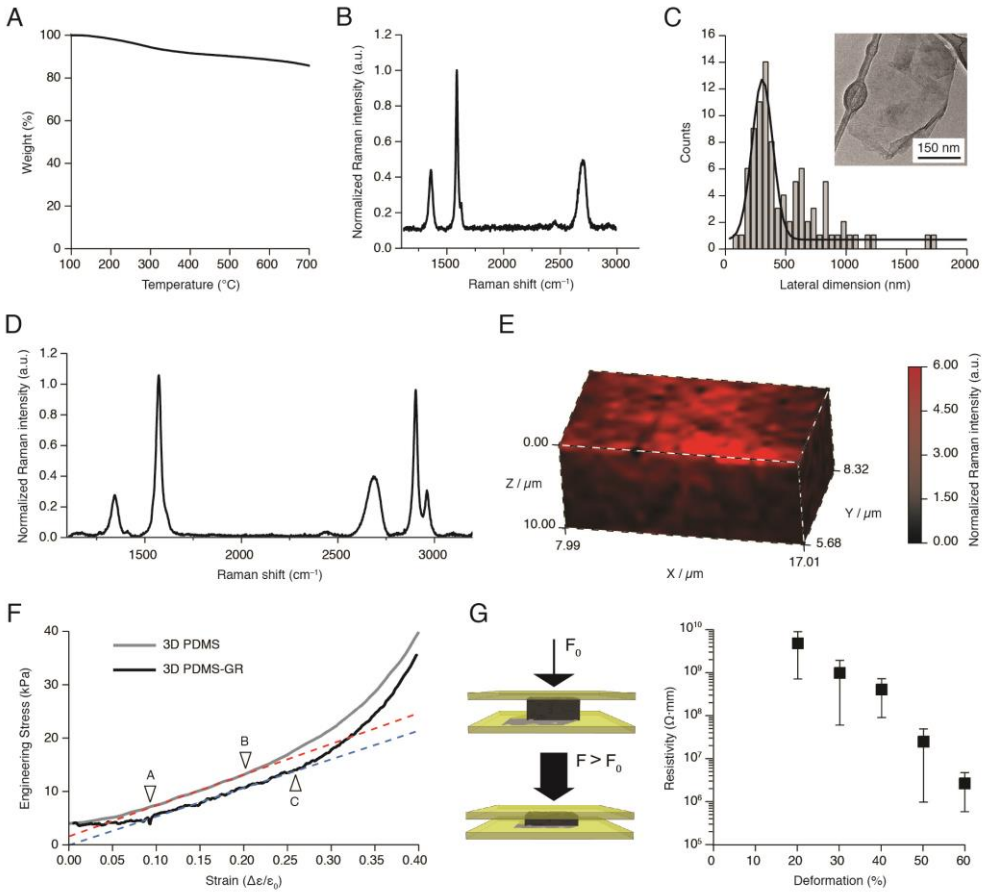

Figure 1| Physicochemical characterization of the few-layer graphene and the 3D PDMS-Gr scaffold used in this study

A. Thermogravimetric analysis (repeated twice) and B. Raman Spectroscopy (average spectrum of at least 20 individual spectra) of the starting few-layers graphene flakes used. In C., lateral size distribution of graphene flakes determined from transmission electron microscopy (TEM) observations (in the inset a representative image is shown). In D., average Raman spectrum obtained from 25 different point measurements performed within a pore of a 3D PDMS-GR scaffold. E. Perspective of a G-band intensity Raman 3D mapping of the interior of a 3D PDMS-GR pore. The reddest regions evidence the higher presence of graphene. In F., stress-strain plots for a 3D PDMS scaffold (in gray) and for a 3D PDMS-GR scaffold (in black). Elastic moduli (E) (about 60 kPa in Young's Modulus for both materials)

were determined from the initial linear slope of the corresponding stress-strain curves (in red, from A to B strain values, for 3D PDMS; in blue, from A to C strain values for 3D PDMS-GR). In G., deformation-dependent resistivity measurements of a 5 mm side size cube of 3D PDMS-GR scaffold. At the left a sketch of the experimental apparatus used to assess scaffold resistivity under variable values of elastic deformation (initial F0 was 50 mN and increased until a maximum 60% deformation was achieved); at the right the resistivity vs. deformation plot showing a monotonic decrease in resistivity as the scaffold is compressed between the two flat contacts. Has to be noted that a minimum 20% deformation has to be reached before being able to measure a resistivity value.

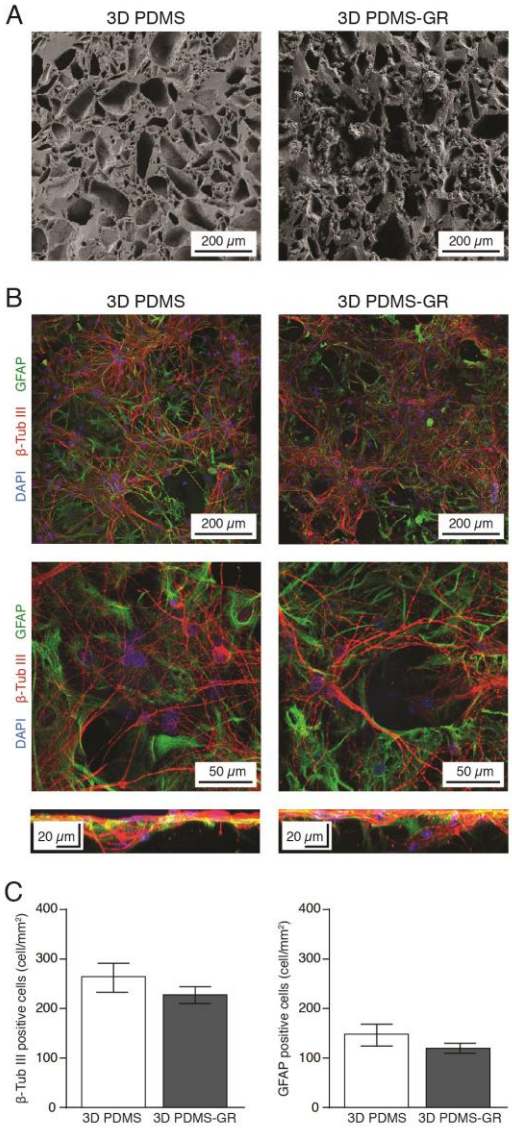

Figure 2 | Development of primary neurons in 3D PDMS and 3D PDMS-GR scaffolds

A. Low magnification SEM images of 3D PDMS and 3D PDMS-GR scaffolds (left and right, respectively); note the similar morphology and cavity size distribution between the two materials. B. Confocal micrographs at low (first row) and high (second row) magnification showing hippocampal cultures grown within a 3D PDMS scaffold (left) and a 3D PDMS-GR one (right). Cells were immune-stained for neurons (anti β-tubulin III, in red), glial cells (anti GFAP, in green) and nuclei (DAPI, in blue). Note the complex growth of neuronal and glial processes exposed to the third dimension. To highlight the genuine three-dimensional cellular networks developed within the two porous scaffolds lateral z views from the 3D

images were shown (third row). C. Bar plots summarizing the neuronal (left) and glial (right) cell densities in the two constructs.

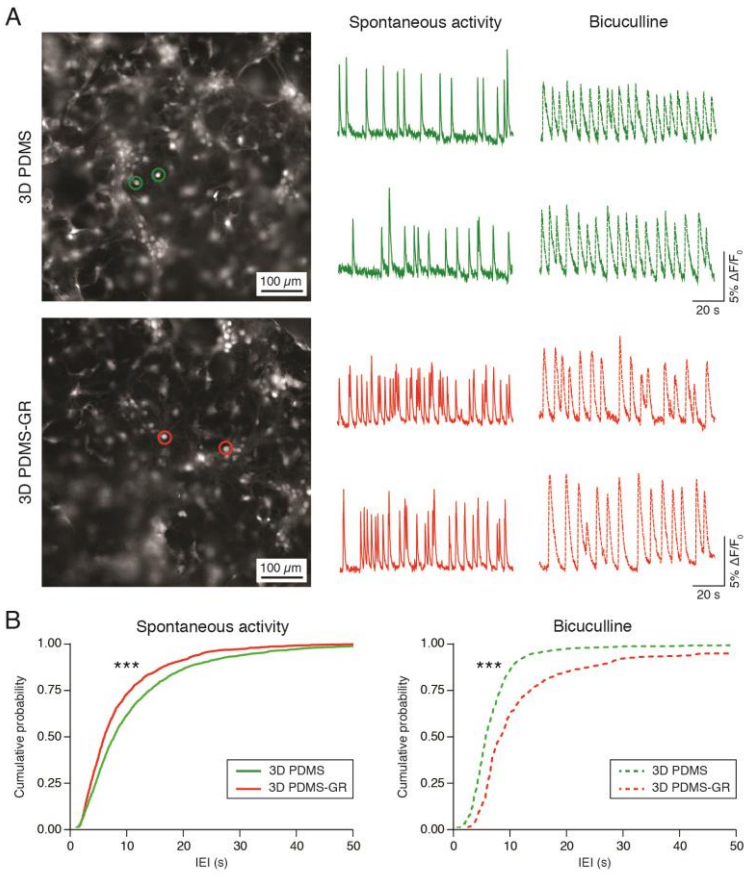

Figure 3 | Live calcium imaging of network activity in 3D PDMS and 3D PDMS-GR

A. Snapshots of representative fields of neuronal cultures grown on 3D PDMS and 3D PDMS-GR stained with the Oregon Green 488-BAPTA-1 AM calcium indicator. Fluorescence tracings represent repetitive Ca2+-events spontaneously (plain traces) or bicuculline induced (dotted traces) recorded in hippocampal cultures (two sample neurons were selected from the same field) in the two culturing conditions (3D PDMS, in green; 3D PDMS-GR, in red). B. Cumulative probability plots of the distribution of Inter Event Interval (IEI) values within 3D PDMS and 3D PDMS-GR neuronal networks in saline solution (left) and upon removal of synaptic inhibition by bicuculline (left). ***$p < 0.001$.

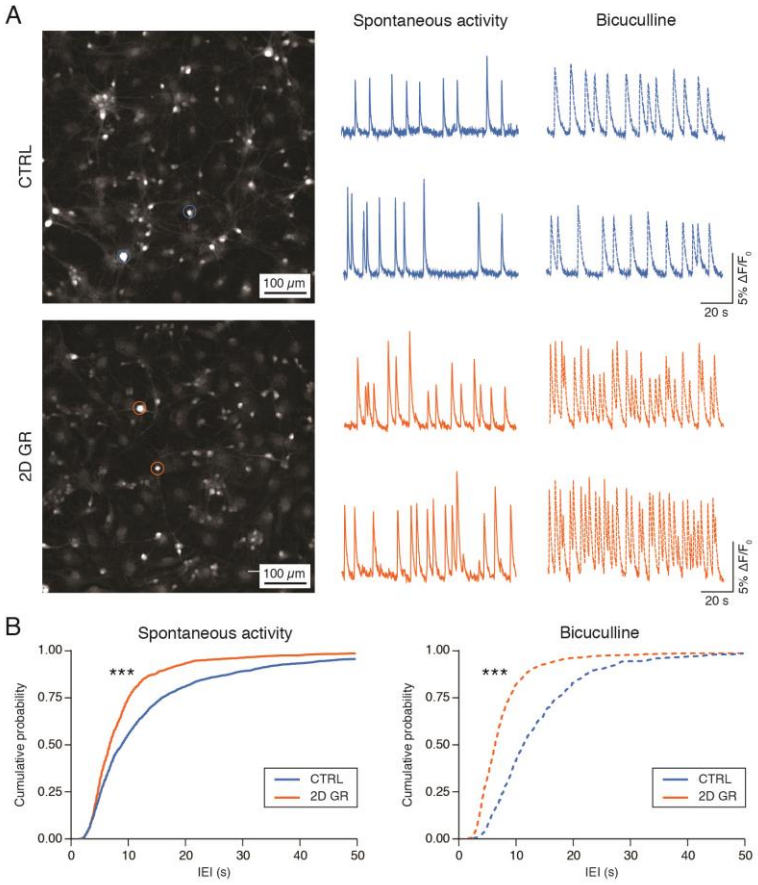

Figure 4 | Live calcium imaging of hippocampal network in 2D controls and 2D-GR

A. Snapshots of representative fields of hippocampal cultures grown on 2D controls (CTRL) and 2D graphene (2D GR) stained with Oregon Green 488-BAPTA-1 AM Ca2+-dye. Fluorescence tracings represent repetitive Ca2+-events spontaneously (plain traces) or bicuculline induced (dotted traces) recorded in hippocampal cultures (two sample neurons were selected from the same field) in the two culturing conditions (CTRL, in blue; 2D GR, in orange). B. Cumulative probability plots of the Inter Event Interval (IEI) values distribution in CTRL and 2D GR neurons in saline solution (left) and upon removal of synaptic inhibition by bicuculline (left). ***$p < 0.001$.

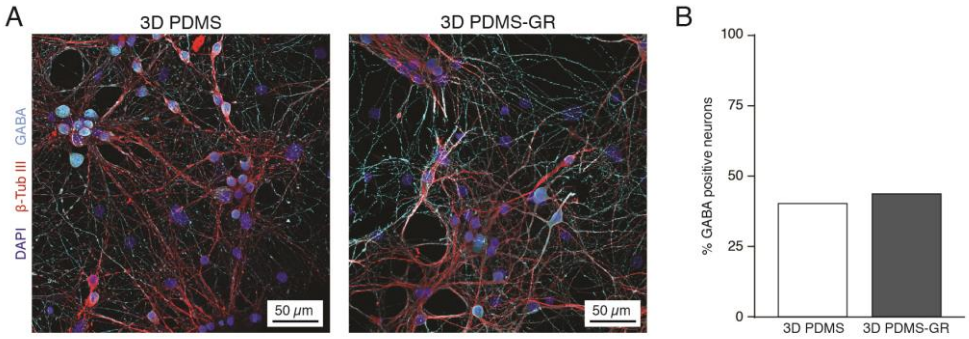

Figure 5 | Expression of GABA phenotype in 3D PDMS and 3D PDMS-GR cultures

A. Confocal reconstructions of 3D PDMS (left) and 3D PDMS-GR (right) cultures co-immunostained against the neuronal marker β-tubulin III (in red) and a phenotypic-specific marker anti-GABA (in cyan). Cell nuclei were pointed out by DAPI (in dark blue). B. Bar plot summarizing the percentage of GABA-positive cells within the total neuronal population.

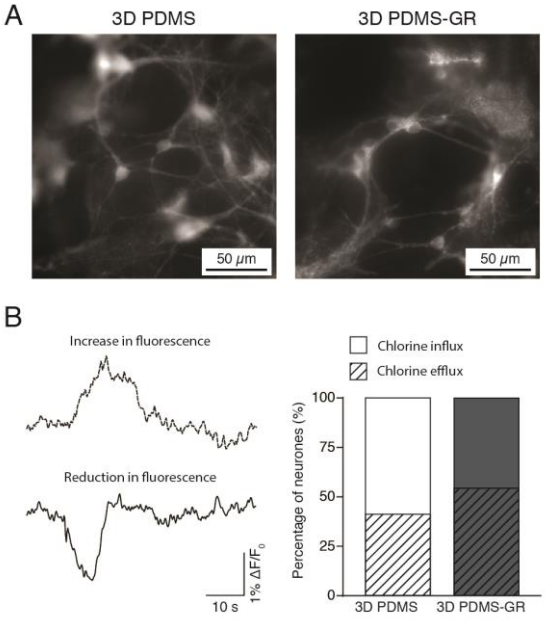

Figure 6 | Live chloride imaging of hippocampal network in 3D PDMS and 3D PDMS-GR cultures

A. Representative visual fields of MQAE-labeled neurons of belonging to neuronal networks developed within a 3D PDMS scaffold (left) and a 3D PDMS-GR scaffold (right). B. At the left, fluorescent tracings representing chloride efflux (dotted trace corresponding to an increase in the detected fluorescence signal) or influx (plain trace corresponding to a reduction of the detected fluorescence signal) observed in two different cells, depending on their degree of maturation. At the right, a bar plot summarizing the percentage in 3D PDMS and in 3D PDMS-GR of neurons responding to GABA application with a chloride influx (mature GABAergic neurons, plain areas) or, instead, a chloride efflux (immature GABAergic neurons, striped areas).

Supporting Information

Tuning neuronal circuit formation in 3D polymeric scaffolds by introducing graphene at the bio/material interface

Rossana Rauti[1†], Nicola Secomandi[1], Cristina Martín[2,3], Susanna Bosi[3], Francesco P. U. Severino[1#], Denis Scaini[1], Maurizio Prato[3,4,5], Ester Vázquez[2,6*], Laura Ballerini[1*]*

Figure S1

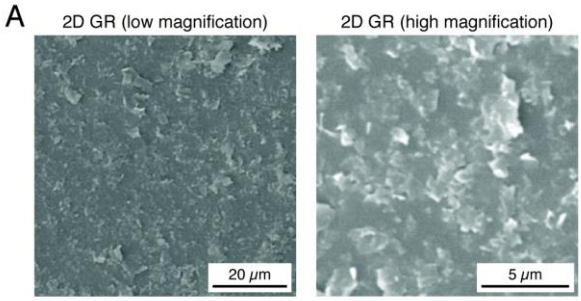

Figure S1 | SEM pictures of a graphene sprayed substrate at different scales.

A. Representative SEM micrographs of a flat graphene substrate prepared by spray-coating. At the left a low magnification image of the substrate showing the high uniformity of the so obtained carpets of graphene flakes; at the right a high magnification image pointing out the islands of graphene flakes composing the film.

PAPER 2: Graphene oxide (nano)flakes modulation of glutamatergic synapses in the amygdala cultured circuits: exploiting synaptic approaches to anxiety disorders

Nicola Secomandi[1], Audrey Franceschi Biagoni[1], Kostas Kostarelos[2], Giada Cellot[1]* and Laura Ballerini[1]*

[1] International School for Advanced Studies, SISSA Trieste, Italy

[2] University of Manchester, Manchester, UK

* Referring authors: Giada Cellot (cellot@sissa.it) and Laura Ballerini (laura.ballerini@sissa.it)

ABSTRACT

Anxiety disorders (ADs) are nervous system maladies involving changes in the amygdala synaptic circuitry, such as an up-regulation of excitatory neurotransmission at glutamatergic synapses. In the field of nanotechnology, graphene oxide flakes with small lateral size (s-GO) have shown outstanding promise for the manipulation of excitatory neuronal transmission with high temporal and spatial precision, thus they are ideal candidates for modulating amygdalar glutamatergic transmission. Here, we validated an *in vitro* model of amygdala circuitry for screening tools to target synapses towards ADs future treatments. After one week *in vitro*, dissociated amygdalar neurons reconnected forming functional networks, whose development recapitulated that of the tissue of origin *in vivo*. When acutely applied to these cultures, s-GO induced a selective modification of excitatory activity. Such evidence

of the interaction between s-GO and amygdalar neurons may ground the exploitation of alternative approaches for the therapy of ADs.

INTRODUCTION

Anxiety disorders (ADs), including phobias and post-traumatic stress disorder, comprise diseases whose common features are excessive and enduring fear, anxiety or avoidance to situations perceived as a threat by the subject.[1] These syndromes are the most prevalent type of psychiatric illness in western societies[2] and have a significant socio-economic burden.[3] Studies, both in patients and in animal models of ADs, have indicated as a potential mechanistic explanation of these syndromes, the expression of glutamate hyper-activity in excitatory synapses of the amygdala.[4–8]

Amygdaloid complex is an almond shaped small structure located deeply into the temporal lobes of the right and left hemispheres, whose function has been related to the processing of emotions such as fear.[9] These structures are composed by clusters of nuclei, uniquely connected with other intra-amygdalar bodies or encephalic areas.[10] This specific wiring is at the basis of amygdala functionality, which works as a processor that receives sensory and cognitive information from the thalamus and cortex and, upon elaboration of these inputs, send diverse outputs to other brain structures, resulting in a range of behavioral/autonomic and endocrine responses to various environmental contests.[11] The characterization of this complex connectivity has been instrumental also in identifying dysfunctional pathways in ADs and new therapeutic approaches aimed at manipulating synaptic functions with a high spatial-temporal control. To address such demands, innovative and promising tools might emerge from nanotechnology developments.

Recently, small graphene oxide flakes (s-GO), a type of carbon based nanomaterial characterized by reduced lateral size, has been found to interfere selectively with the activity of hippocampal glutamatergic synapses.[12,13] When delivered *in vivo* into the hippocampus of juvenile rats, this nanomaterial induced a selective, transient and spatially restricted modulation of the excitatory synaptic activity.[13]

s-GO high spatial and temporal precision in targeting glutamatergic synaptic transmission, might be exploited to address the excitatory malfunction of the amygdala, underlying ADs. However, to date it is completely unexplored whether s-GO exerts effects on the activity of amygdalar neurons.

The restricted anatomical access to amygdaloid bodies limits specific experimental synaptic studies *in vivo*, thus, more simplified models of amygdala circuitries are needed for fast screening of new drugs, molecules and nanomaterials that might have applications for the treatment of ADs. In the current work, we developed an *in vitro* model of amygdalar neuronal networks, whose activity was explored by patch clamp recordings. We show that after one week *in vitro* neurons reconnected, forming active synapses, whose characteristics underwent to a process of maturation, resembling those occurring *in vivo*. The acute treatment with s-GO of these cultures strongly modulated glutamatergic signaling, indicating that the nanomaterial interacted with amygdalar neurons at the level of excitatory synapses. Thus, we validated this alternative *in vitro* model of amygdala for studying the effect of innovative nano-sized tools for the therapy of ADs.

MATERIALS AND METHODS

Graphene oxide nanosheets

Graphene oxide sheets of small lateral dimensions were synthesized using a modified Hummers method. A detailed description for the preparation and characterization of this nanomaterial can be found elsewhere.[12,13]

Dissociated amygdalar cultures

Isolation of rat brains was performed in agreement with the Italian law (decree 26/14) and the European Union (EU) guidelines (2007/526/CE and 2010/63/UE) and all the procedures were authorized by the local veterinary authorities and by the institutional (ISAS) ethical committee. The animal use was approved by the Italian Ministry of Health.

Primary cultures of amygdalar cells were obtained from Wistar rats aged 8-10 days. Brains were quickly removed from the skull and placed in fresh ice-cold artificial cerebrospinal fluid (ACSF) whose composition was (in mM): 124 NaCl, 24 $NaHCO_3$, 13 glucose, 5 HEPES, 2.5 KCl, 2 $CaCl_2$, 2 $MgSO_4$ and 1,2 $NaPO_4H_2$ with a pH of 7.3-7.4 when saturated with 95% O_2 and 5% CO_2.[14]

Coronal brain slices (400 μm) including the amygdala complex were cut using a vibratome (Leica VT100S) and transferred into a dish containing ice-cold oxygenated ACSF. Under a dissecting microscope (Olympus SZ40), the regions containing the amygdalar nuclei were isolated using a biopsy punch with a dimeter of 1 mm (Kai Medical, Japan).

The collected tissue was enzymatically and mechanically dissociated following standard protocol.[15] Cells were seeded onto poly-L-ornithine-coated glass coverslips at a density of 800 cells/mm^2 and maintained in controlled conditions (at 37 °C, 5% CO2) for 8-12 days.

Immunofluorescence

Cultures were fixed after 8 or 12 days *in vitro* (DIV) with 4% paraformaldehyde in PBS for 20 minutes and adding 1% glutaraldehyde in PBS for 1 hour for GABA staining as previously reported.[16] Cells were permeabilized with Triton X-100 (0.3 %), incubated for 30 minutes at room temperature (RT) with primary antibodies and, after being rinsed with PBS, incubated with secondary antibodies for 30 min at RT. As primary antibodies, we used mouse monoclonal anti-GFAP antibody (Sigma G3893, 1:500 dilution) and rabbit polyclonal anti- β-tubulin III antibody (Sigma T2200, 1:500 dilution) to label glial cells and neurons respectively.[12] GABAergic neurons were co-stained with mouse monoclonal anti- β-tubulin III antibody (Sigma T8535, 1:500 dilution) and anti-GABA polyclonal antibody produced in rabbit (Sigma A2052, 1:300 dilution[17]). As secondary antibodies, we employed Alexa 594 goat anti-rabbit (Invitrogen, 1:500 dilution), Alexa 594 goat anti-mouse (Invitrogen, 1:500 dilution), Alexa 488 goat anti-mouse (Invitrogen, 1:500 dilution) and Alexa 488 goat anti-rabbit (Invitrogen, 1:500 dilution). Nuclei were marked with DAPI (1:400, Invitrogen). For each sample, images of 5 randomly selected fields were acquired using a confocal microscope (Nikon Eclipse Ti, Nikon, Japan). Images from three different culture series were analyzed with the software ImageJ (NIH).

Electrophysiology

Patch clamp whole-cell recordings were performed from neurons using glass micropipettes with a resistance of 4 ÷ 7 MΩ when filled with the intracellular saline solution composed of (mM): 120 K gluconate, 20 KCl, 10 HEPES, 10 EGTA, 2 $MgCl_2$, 2 Na_2ATP, pH 7.3 and osmolarity 300 mOsm. All experiments were performed at RT from cells continuously perfused at 5 ml/min with the standard extracellular solution containing (mM): 150 NaCl, 4 KCl, 2 $CaCl_2$, 1

$MgCl_2$, 10 HEPES, 10 glucose, pH 7.4. All data were recorded by means of a Multiclamp 700B patch amplifier (Axon CNS, Molecular Devices) digitized at 10 KHz by pClamp 10 software (Molecular Devices LLC, USA). Input resistance and cells capacitance were measured online with the membrane test feature of the pClamp software. Spontaneous activity was recorded in voltage clamp mode at a holding potential of -56 mV (not corrected for the liquid junction potential which was -14 mV).

Spontaneous postsynaptic currents (PSCs) were analyzed offline using the software AxoGraph X (Axograph Scientific), which exploits a detection algorithm based on a sliding template. For each recording, all the collected events were averaged and the peak amplitude and kinetic properties of the mean current were calculated. The decay time of PSCs was calculated by fitting the decaying phase of the current with a mono-exponential function. Templates characterized by diverse decay times were used to separate offline glutamate AMPA-receptor mediated PSCs (~3 ms) and those mediated by $GABA_A$ -receptors (~20 ms)

Pairs of monosynaptically connected neurons, in which the cells were apart ~100 µm one from the other, were recognized by the short latency 2.9 ± 0.3 ms[12,18] between the peak of the presynaptic neuron and the onset of the evoked PSC (ePSC).

Using a Picospritzer (PDES-02DX; NPI electronic GmbH, Germany), an injection of pressurized air (500 ms, 0.5 PSI) was exploited to deliver a puff of s-GO to the amygdalar neurons. The puff pipette was filled with standard saline solution (control) or with s-GO (100 µg/ml diluted in saline solution) and located at a distance of about 200 µm from the recorded cell. Considering 1 ml of extracellular solutions in our recording chamber, we estimated that the concentration of s-GO reaching the patch-clamped neurons was at least 10% of that present in the puff pipette as previously reported.[12,13] PSCs were recorded before (10 min, baseline) and after (5 min) the local ejection.

Statistical Analysis

All values from samples subjected to the same experimental protocols were pooled together and expressed as mean ± s.e.m. with n = number of neurons, if not otherwise indicated. D'Agostino & Pearson omnibus normality test was applied to evaluate the statistical distribution of the data sets. Statistically significant difference between two data sets was assessed by Student's t-test or by Mann–Whitney test. Statistical significance was determined at $P<0.05$.

RESULTS

To explore the impact of nanomaterials on amygdalar circuitry, in particular on subcellular components, such as synapses, we developed a simplified *in vitro* model of amygdala. This structure was isolated with a high degree of precision from coronal brain slices using a biopsy punch. The collected region underwent to a process of enzymatic digestion (see methods), then cells were seeded on peptide covered glass coverslips and allowed to develop for 8-12 DIV. In parallel, the slices from which the amygdalar complexes were isolated were processed with Nissl staining, to assess brain structures and confirm the correct anatomical sampling of amygdalae (Figure 1A).

The maturation of amygdalar cultures *in vitro* was characterized through immunofluorescence technique and confocal microscopy. Fixed preparations were immunostained for neuronal and glial markers at two different time points of their development (8 and 12 DIV) to measure culture size and cell composition (Figure 1B-E). Neurons were labelled with antibodies against the specific cytoskeletal components β-tubulin III (in red) and against glial fibrillary acidic protein (GFAP, in green) to visualize glial

cells. Nuclei were marked with DAPI (in blue). As shown by the z-stack reconstructions in Figure 1B, glial cell density remained stable between 8 and 12 DIV (at 8 DIV: 110.6 ± 7.8 cells/mm^2 and at 12 DIV: 98.0 ± 5.3 GFAP positive cells/mm^2; n = 30 visual fields each condition), while neuronal density decreased along with the culture aging (at 8 DIV: 80.3 ± 4.8 cells/mm^2 and at 12 DIV: 64.2 ± 4.3 cells/mm^2; P = 0.0131, Figure 1B-C). We further explored the neuronal composition of our cultures by determining the amount of inhibitory neurons. To this aim, we co-immunostained cells with antibodies against β-tubulin III (in red) and GABA (in light blue, Figure 1D). The amount of double positive cells, identified as GABAergic neurons, was not changed between 8 and 12 DIV (42 % and 40 % respectively, n = 30 visual fields for each conditions, Figure 1E). Thus, dissociated amygdalar cultures appeared healthy and formed by well-differentiated GFAP-positive cells and different neuronal phenotypes. Their composition appeared stable over time with the exception for a slight, but statistically significant reduction in the number of neurons in older cultures.

Next, we tested amygdalar circuit activity *in vitro* by patch clamp recording of basal synaptic activity (voltage clamp mode) from single cells which were used as probes to sense inputs received by surrounding neurons. Figure 1F shows exemplificative recordings from neurons at 8 and 12 DIV, in which the current deflections correspond to spontaneous PSCs (sPSCs). sPSCs frequencies were slightly larger, although not significantly, in older cultures (8 DIV: 1.5 ± 0.3 Hz, n = 21; 12 DIV: 2.4 ± 0.4 Hz, n = 41; Figure 1G), while PSCs amplitudes increased in older cultures (from 20 ± 1 pA 8 DIV to 30 ± 2 pA 12 DIV; Figure 1H). Such statistically significant difference (P = 0.0003) is in agreement with the presence of more mature synapses at the end of the second week *in vitro*.

In amygdalar cultures, spontaneous synaptic activity was composed by a mixed population of fast (~3 ms) and slow (~20 ms) decaying sPSCs. The former were abolished by the

application of CNQX (10 μM), an antagonist of glutamate AMPA receptor mediated currents (n = 6), while the latter were blocked by treatment with gabazine (10 μM), a $GABA_A$ receptor antagonist (n = 3). Their kinetic properties together with their pharmacology supports their excitatory glutamatergic (EPSCs; fast decaying events) or inhibitory GABAergic (IPSCs; slow decaying events) nature.

The diverse decay times of EPSCs and IPSCs were exploited to isolate them offline (see methods). Figure 2A displays examples of fast decaying excitatory and slow decaying inhibitory sPSCs, collected from the traces of Figure 1F. The analysis of the EPSCs and IPSCs revealed small changes in their frequencies during the maturation of the cultures (EPSCs from 1.1 ± 0.3 Hz to 2.1 ± 0.4 Hz; IPSCs from 0.4 ± 0.1 Hz to 0.3 ± 0.1 Hz, 8 and 12 DIV, respectively; Figure 2B). However, the amplitudes of both EPSCs and IPSCs resulted enhanced in a statistically significant manner in older cultures in respect to younger ones (EPSCs from 17 ± 1 pA to 22 ± 1 pA, 8 and 12 DIV, respectively $P = 0.008$; IPSCs: from 25 ± 3 pA to 39 ± 3 pA, 8 and 12 DIV, respectively, $P = 0.005$; Figure 2C). When analyzing the kinetic properties of IPSCs and EPSCs separately, we found that the rise and decay times of EPSCs both increased during neuronal growth (rise time: from 0.72 ± 0.02 ms to 1.02 ± 0.04 ms, from 8 and 12 DIV, respectively, $P < 0.0001$; decay time: from 2.64 ± 0.16 ms to 3.64 ± 0.18 ms, 8 and 12 DIV, respectively, $P = 0.0042$). Conversely, while also the IPSCs rise time became longer (from 1.37 ± 0.07 ms to 2.05 ± 0.05 ms, 8 and 12 DIV, $P < 0.0001$), their decay time resulted faster in older cells (from 21.10 ± 1.31 ms to 17.31 ± 0.88 ms, 8 and 12 DIV, $P < 0.0001$; Figure 2D). All together these findings indicated that both the excitatory and inhibitory components of the network mature during the second week of differentiation *in vitro*.

With the exception of IPSCs decay time, all sPSCs kinetic parameters slowed down during neuronal growth, a result in accordance with an increase in the electrotonic filtering of neurites (e.g. longer neurites), following dimensional growth of single neurons. Indeed, cell capacitance, an indirect measure of neuronal size,[19] of more mature neurons was increased in respect to younger cultures (from 52 ± 3 pF to 61 ± 3 pF, n = 30 and n = 55, 8 and 12 DIV respectively, $P = 0.031$), while the input resistance (from 398 ± 36 MΩ to 413 ± 28 MΩ, 8 and 12 DIV, Figure 2E) and the resting membrane potential (from -59 ± 2 mV to -63 ± 1 mV, 8 and 12 DIV, Figure 2F) were similar at the two time points measured.

In a further set of experiments, we induced in current clamp mode action potentials (APs) by injecting neurons with short square pulses of depolarizing currents (Figure 2G). The analysis of AP amplitudes (at 8 DIV: 98 ± 4 mV, n = 14, and 12 DIV: 102 ± 2 mV, n = 47) and half-widths (at 8 DIV: 3.0 ± 0.2 ms 12 DIV: 3.0 ± 0.2 ms) detected no differences between the two culture groups (Figure 2 G-I), suggesting that APs were already mature after one week of growth *in vitro*.

We further investigated synaptic connectivity at 12 DIV by dual patch clamp recordings from pairs of mono-synaptically connected neurons (Figure 3A): the presynaptic cell was elicited to fire APs in current clamp configuration, while the postsynaptic one was simultaneously clamped at -56 mV to monitor the presence of an ePSC (Figure 3B, see methods). The probability to find monosynaptically connected pairs of neurons was high (75%, n = 36 pairs, Figure 3C), indicating an elevated degree of connectivity in the neuronal network. In addition, the analysis of ePSCs kinetic features revealed that the majority (93%, n = 29, Figure 3D) of synapses activated slow decaying currents (~ 20 ms), identifiable as $GABA_A$ mediated IPSCs, while only a subset of these (7%) showed fast ePSCs (~3 ms), compatible with AMPA receptor mediated EPSCs (Figure 3B). The short-term plasticity of these

synapses, evaluated by a pair of stimuli at 20 Hz (see methods), revealed that both excitatory and inhibitory connections underwent to short-term depression of ePSCs (ratios between the amplitude of the second and first ePSCs were 0.9 ± 0.1 for the excitatory connections and 0.7 ± 0.1 for the inhibitory ones; Figure 3B).

In sum, our electrophysiological characterization showed that after 8 DIV, dissociated amygdalar neurons reconnected forming functional synapses, whose activity was further modified during the second week of development *in vitro*, compatibly with the acquisition of a more mature phenotype of the culture. We decided to exploit such simplified model to test the interaction of s-GO with amygdalar neurons.

In the last set of experiments, we tested whether s-GO affected synaptic activity as showed before for hippocampal culture.[12,13] In mature cultures (12 DIV), a puff of solution containing s-GO (or saline as control) was pressure-applied through a pipette located at a distance of 200 µm from a neuron, while its spontaneous activity was monitored in voltage clamp mode (Figure 4A). Figure 4B shows that s-GO application (orange arrow) produced a change in neuronal activity, while the treatment with saline (black arrow) exerted no effect. Magnifications of the traces before and after the puffs (insets in the bottom row of figure 4B) display that s-GO induced changes in the frequency but not in the amplitude of sPSCs. A quantification of these parameters detected a statistically significant increment in the after puffs frequencies of sPSCs between saline (n = 12) and s-GO (n = 12) treated neurons (for saline-treated: 2.5 ± 0.5 Hz and for s-GO-treated: 5.5 ± 1.1 Hz, $P = 0.0447$; Figure 4C), while the pre-puffs frequencies were similar between the two treatments (for saline-treated: 2.6 ± 0.5 Hz and for s-GO-treated: 4.2 ± 1.0 Hz; figure 4C). No changes were detected in the amplitudes of sPSCs due to s-GO application (pre-puff values were 65 ± 16 pA for saline and

66 ± 13 pA for s-GO; post-puff values were 57 ± 13 pA for saline and 48 ± 6 pA for s-GO; Figure 4D).

To better point out the effect of s-GO, we normalized the post-puff values for the pre-puff ones for each cell (Figure 4E). Thus, we observed a change of 78.8% ± 36.5% in sPSCs frequency after the puff in s-GO treated neurons (P = 0.0424), on the opposite in saline treated cells this difference was not statistically relevant (-1.5% ± 5.0%; Figure 4E). By isolating the excitatory and the inhibitory components of the network by means of offline analysis, we detected that s-GO induced modifications only in the frequency of EPSCs (for saline treated neurons: -0.4% ± 7.3%, and for s-GO treated ones: 130% ± 65.3%, P = 0.0255 pre vs post in s-GO treated samples; P = 0.0292 saline vs s-GO; figure 4F), while that of IPSCs was unchanged (12.1% ± 14.3%, for saline treated and 15.2% ± 19.5%, for s-GO treated; figure 4G). These results showed that this nanomaterial was able to interfere with the function of amygdalar neurons, by upregulating specifically the activity of excitatory synapses.

DISCUSSION

In the current work, we studied the interaction of s-GO with amygdalar neurons, showing that this material can modulate selectively the excitatory glutamatergic transmission in neuronal circuits obtained from this brain region. We developed dissociated cultures from the amygdalae to better dissect synaptic activity at the single cell level.[20,21] In respect to previous works,[14,22–25] we improved our preparation in terms of purity, due to a more precise procedure to explant amygdalae, confirmed by our Nissl staining.

Cultured amygdalar circuits developed with a slight decrease in neurons during the second week *in vitro*, commonly observed in culture,[26] possibly related to a reduced availability of

neurotrophic factors in respect to the *in vivo* condition.[27–29] However, despite the slight decline in the number of neurons, synaptic circuits seems to mature progressively, as indicated by the enhancement in the amplitude of both EPSCs and IPSCs at 12 DIV.

Also the kinetic properties of sPSCs underwent to modifications in this time window: rise times of EPSCs and IPSCs slowed down, while decay times got slower for EPSCs and faster for IPSCs. These trends match with those observed in amygdala explants obtained from animals at different ages,[30] indicating that, in our model, neurons retraced a process of physiological maturation. While the speed up of IPSCs decay time is compatible with a developmental switch from the α2- to the α1-subunit of $GABA_A$ receptors,[31] the slowing down of the other kinetic properties may be in part related to electrotonic filtering due to the growth of neurons during the maturation. Longer dendrites, indeed, would result in slower kinetic properties of sPSCs.[32] In agreement with this hypothesis, an increase in cell capacitance, an indicator of neuronal dimension, was observed at 12 DIV.[19] Conversely, we did not detect changes either in the properties of APs or in the resting membrane potentials, both reported similar to those of juvenile amygdalar neurons *in vivo.*[33] This confirms that our cultures present characteristics of mature amygdalar cells, with synapses undergoing a progressive strengthening when re-constructing active contacts *in vitro.*[34,35]

This observation was reinforced by the high connectivity detected by dual patch clamp recordings at 12 DIV: to note, the large majority of synaptic connections were GABAergic. This might appear controversial respect to the characterization of spontaneous network activity, where the frequency of EPSCs was prevalent when compared to that of IPSCs. The higher probability to find inhibitory synapses was possibly related to our experimental setting (dual recordings from neurons apart 100 μm one to the other), which would favor the selection of interneurons.[15]

The contribution of amygdala in shaping behavioural responses to environmental stimuli is developmentally regulated,[36,37] with complex fear responses consolidating around the third postnatal week.[38–40] Our electrophysiological characterization showed that, when the tissue of origin is collected from adolescent animals (P8-P10) and cells are allowed to differentiate *in vitro* for 8-12 days, cultures have single cell and synaptic features resembling those of *in vivo* amygdalar neurons of juvenile animals. Thus, we developed an easily accessible, simplified model of mature amygdala for the study of neuronal circuits, suited for fast screening of new drugs/materials/devices.

We used this system to show that s-GO could modify the synaptic function of amygdalar neurons. In fact, we reported that when acutely applied, the nanomaterial induced an enhancement in network activity, measured as an increase in the frequency of sPSCs respect to the pre-treatment baseline. Such effect was selective for the glutamatergic synapses, since s-GO changed the occurrence of EPSCs, but not that of IPSCs. s-GO exert their effect modifying the presynaptic release of the neurotransmitter.[12,13] In other brain region, the prolonged exposure to this nanomaterial resulted in a depletion of glutamate from presynaptic terminals, responsible for a decrease in the activity of excitatory synapses.[12,13] Since ADs are characterized by a glutamate mediated hyper-function of the amygdala,[4,7,41,42] s-GO might be exploited as therapeutics for long term impairing of glutamate release, ultimately down-regulating specifically this pathologically potentiated excitatory signaling.

Further experiments will be required to demonstrate that the increase in EPSC frequency reported here after s-GO application is only a transient effect and that, upon prolonged application, the nanomaterial is effective in reducing amygdalar activity. If the high spatial and temporal precision demonstrated by s-GO in downregulating excitatory signaling in other brain regions will be preserved in the amygdala, this nanomaterial might be a powerful

alternative tool for the modulation of selective glutamatergic circuits whose activity is aberrant in ADs.

REFERENCES

1. American Psychiatric Association APA. *Diagnostic and statistical manual of mental disorders: DSM-5*. 5th ed. American Psychiatric Association: Washington, D.C, 2013.

2. Kessler RC, Berglund P, Demler O, Jin R, Merikangas KR, Walters EE. Lifetime Prevalence and Age-of-Onset Distributions of DSM-IV Disorders in the National Comorbidity Survey Replication. *Arch Gen Psychiatry* 2005; **62**: 593.

3. Trautmann S, Rehm J, Wittchen H. The economic costs of mental disorders: Do our societies react appropriately to the burden of mental disorders? *EMBO Rep* 2016; **17**: 1245–1249.

4. Cortese BM, Phan KL. The Role of Glutamate in Anxiety and Related Disorders. *CNS Spectr* 2005; **10**: 820–830.

5. Ganella DE, Kim JH. Developmental rodent models of fear and anxiety: from neurobiology to pharmacology: Pharmacological studies in developmental anxiety. *Br J Pharmacol* 2014; **171**: 4556–4574.

6. Shin LM, Liberzon I. The Neurocircuitry of Fear, Stress, and Anxiety Disorders. *Neuropsychopharmacology* 2010; **35**: 169–191.

7. Wierońska J, Stachowicz K, Nowak G, Pilc A. The Loss of Glutamate-GABA Harmony in Anxiety Disorders. In: Kalinin V (ed). *Anxiety Disorders*. InTech, 2011.

8. Forster G, Andrew M, L. L, J. M. The Role of the Amygdala in Anxiety Disorders. In: Ferry B (ed). *The Amygdala - A Discrete Multitasking Manager*. InTech, 2012.

9. Aggleton JP. *The Amygdala. A functional analysis*. Second edition. Oxford Univ. Press: New York, 2000.

10. Pitkänen A. Connectivity of the rat amygdaloid complex. In: *The amygdala. A functional analysis*. Oxford Univ. Press: New York, 2000, pp 31–115.

11. Yaniv D, Desmedt A, JaffAD R, Richter-Levin G. The amygdala and appraisal processes: stimulus and response complexity as an organizing factor. *Brain Res Rev* 2004; **44**: 179–186.

12. Rauti R, Lozano N, León V, Scaini D, Musto M, Rago I *et al.* Graphene Oxide Nanosheets Reshape Synaptic Function in Cultured Brain Networks. *ACS Nano* 2016; **10**: 4459–4471.

13. Rauti R, Medelin M, Newman L, Vranic S, Reina G, Bianco A *et al.* Graphene Oxide Flakes Tune Excitatory Neurotransmission in Vivo by Targeting Hippocampal Synapses. *Nano Lett* 2019; **19**: 2858–2870.

14. Wu YE, Pan L, Zuo Y, Li X, Hong W. Detecting Activated Cell Populations Using Single-Cell RNA-Seq. *Neuron* 2017; **96**: 313-329.e6.

15. Cellot G, Toma FM, Kasap Varley Z, Laishram J, Villari A, Quintana M *et al.* Carbon Nanotube Scaffolds Tune Synaptic Strength in Cultured Neural Circuits: Novel Frontiers in Nanomaterial-Tissue Interactions. *J Neurosci* 2011; **31**: 12945–12953.

16. Furlan F, Taccola G, Grandolfo M, Guasti L, Arcangeli A, Nistri A *et al.* ERG Conductance Expression Modulates the Excitability of Ventral Horn GABAergic Interneurons That Control Rhythmic Oscillations in the Developing Mouse Spinal Cord. *J Neurosci* 2007; **27**: 919–928.

17. Pampaloni NP, Lottner M, Giugliano M, Matruglio A, D'Amico F, Prato M *et al.* Single-layer graphene modulates neuronal communication and augments membrane ion currents. *Nat Nanotechnol* 2018; **13**: 755–764.

18. Pavlidis P, Montgomery J, Madison DV. Presynaptic Protein Kinase Activity Supports Long-Term Potentiation at Synapses Between Individual Hippocampal Neurons. *J Neurosci* 2000; **20**: 4497–4505.

19. Lindau M, Neher E. Patch-clamp techniques for time-resolved capacitance measurements in single cells. *Pflügers Arch Eur J Physiol* 1988; **411**: 137–146.

20. Buchhalter JR, Dichter MA. Electrophysiological comparison of pyramidal and stellate nonpyramidal neurons in dissociated cell culture of rat hippocampus. *Brain Res Bull* 1991; **26**: 333–338.

21. Godfrey EW, Nelson PG, Schrier BK, Breuer AC, Ransom BR. Neurons from fetal rat brain in a new cell culture system: A multidisciplinary analysis. *Brain Res* 1975; **90**: 1–21.

22. Kasckow JW, Regmi A, Gill PS, Parkes DG, Geracioti TD. Regulation of Corticotropin-Releasing Factor (CRF) Messenger Ribonucleic Acid and CRF Peptide in the Amygdala: Studies in Primary Amygdalar Cultures. *Endocrinology* 1997; **138**: 4774–4782.

23. Lin CH, Huang YC, Tsai JJ, Gean PW. Modulation of voltage-dependent calcium currents by serotonin in acutely isolated rat amygdala neurons. *Synapse* 2001; **41**: 351–359.

24. Lorenzo A, Díaz H, Carrer H, Cáceres A. Amygdala neurons in vitro: Neurite growth and effects of estradiol: Amygdaline Neurite Growth In Vitro. *J Neurosci Res* 1992; **33**: 418–435.

25. Mou L, Heldt SA, Ressler KJ. Rapid brain-derived neurotrophic factor-dependent sequestration of amygdala and hippocampal GABAA receptors via different tyrosine receptor kinase B-mediated phosphorylation pathways. *Neuroscience* 2011; **176**: 72–85.

26. Ichikawa M, Muramoto K, Kobayashi K, Kawahara M, Kuroda Y. Formation and maturation of synapses in primary cultures of rat cerebral cortical cells: an electron microscopic study. *Neurosci Res* 1993; **16**: 95–103.

27. Hanson MG, Shen S, Wiemelt AP, McMorris FA, Barres BA. Cyclic AMP Elevation Is Sufficient to Promote the Survival of Spinal Motor Neurons *In Vitro*. *J Neurosci* 1998; **18**: 7361–7371.

28. Morrison RS, Sharma A, de Vellis J, Bradshaw RA. Basic fibroblast growth factor supports the survival of cerebral cortical neurons in primary culture. *Proc Natl Acad Sci* 1986; **83**: 7537–7541.

29. Walicke P, Cowan WM, Ueno N, Baird A, Guillemin R. Fibroblast growth factor promotes survival of dissociated hippocampal neurons and enhances neurite extension. *Proc Natl Acad Sci* 1986; **83**: 3012–3016.

30. Bosch D, Ehrlich I. Postnatal maturation of GABAergic modulation of sensory inputs onto lateral amygdala principal neurons: Development of sensory input inhibition in mouse lateral amygdala. *J Physiol* 2015; **593**: 4387–4409.

31. Ehrlich DE, Ryan SJ, Hazra R, Guo J-D, Rainnie DG. Postnatal maturation of GABAergic transmission in the rat basolateral amygdala. *J Neurophysiol* 2013; **110**: 926–941.

32. Magee JC. Dendritic integration of excitatory synaptic input. *Nat Rev Neurosci* 2000; **1**: 181–190.

33. Sosulina L, Meis S, Seifert G, Steinhäuser C, Pape H-C. Classification of projection neurons and interneurons in the rat lateral amygdala based upon cluster analysis. *Mol Cell Neurosci* 2006; **33**: 57–67.

34. Isaeva EV, Sidorenko VG, Fedulova SA, Veselovskii NS. Evoked inhibitory postsynaptic currents in the dynamics of development of cultured hippocampal neurons of rats. *Neurophysiology* 1999; **31**: 304–309.

35. Lin Y-C, Huang Z-H, Jan I-S, Yeh C-C, Wu H-J, Chou Y-C *et al.* Development of excitatory synapses in cultured neurons dissociated from the cortices of rat embryos and rat pups at birth. *J Neurosci Res* 2002; **67**: 484–493.

36. Chareyron LJ, Lavenex PB, Lavenex P. Postnatal development of the amygdala: A stereological study in rats. *J Comp Neurol* 2012; **520**: 3745–3763.

37. Collier AC, Mast J, Meyer DR, Jacobs C-E. Approach-avoidance conflict in preweanling rats: A developmental study. *Anim Learn Behav* 1979; **7**: 514–520.

38. Chen SWC. The Role of the Amygdala and Olfaction in Unconditioned Fear in Developing Rats. *J Neurosci* 2006; **26**: 233–240.

39. Raineki C, Shionoya K, Sander K, Sullivan RM. Ontogeny of odor-LiCl vs. odor-shock learning: Similar behaviors but divergent ages of functional amygdala emergence. *Learn Mem* 2009; **16**: 114–121.

40. Shionoya K, Moriceau S, Lunday L, Miner C, Roth TL, Sullivan RM. Development switch in neural circuitry underlying odor-malaise learning. *Learn Mem* 2006; **13**: 801–808.

41. Mahan AL, Ressler KJ. Fear conditioning, synaptic plasticity and the amygdala: implications for posttraumatic stress disorder. *Trends Neurosci* 2012; **35**: 24–35.

42. Smerin S, Chen A, Li H. Neurophysiology of Aggression in Posttraumatic Stress Disorder. *J Psychiatry* 2016; **19**.

FIGURE LEGENDS

FIGURE 1: Dissociated amygdalar neurons reconstruct functional networks *in vitro*

(A) Schematic representation of dissociated amygdalar culture procedure: brains isolated from adolescent rats are sliced (left); amygdaloid nuclei are precisely isolated by a biopsy punch (in green) and enzymatically dissociated to get pure cultures (right). The remaining tissue is stained with Nissl procedure (middle) to confirm the sampling of the amygdalae. (B) Confocal images of cultures at 8 (left) and 12 (right) DIV, stained with β tubulin III (in red), GFAP (in green) and DAPI for nuclei (in blue). (C) Bar plots summarizing the neuron (left) and glial (right) cell densities at 8 and 12 DIV. Note the decrease in neuronal density in cultures at 12 DIV. (D) Confocal images of neurons double stained with β tubulin III (in red) and GABA (in light blue) at 8 and 12 DIV. (E) Bar plots summarize the percentage of GABAergic neurons (double-positive cells) at the two time points. (F). On the top, representation of patch clamp recording from single cell. Below, exemplificative traces of spontaneous network activity recorded from amygdalar neurons after 8 and 12 DIV. Bar plots showing the frequency (G) and the amplitude (H) of sPSCs at 8 and 12 DIV.

In all bar plots, dots superimposed to the bars are single values and * $P < 0.05$.

FIGURE 2: Electrophysiological characterization of amygdalar neurons

(A) Offline PSCs analysis of fast-EPSCs (left) and slow-IPSCs (right) at 8 and 12 DIV. Bar plots showing the frequencies (B) and the amplitudes (C) of EPSCs and IPSCs at the two considered temporal points. The amplitudes of both the types of currents are increased in more mature cultures. (D) Summary graphs of EPSC and IPSC kinetic properties at 8 (black circle) and 12 (blue square) DIV. (E) Summary graph of input resistance and cell capacitance at 8 (black circle) and 12 (blue square) DIV. Capacitance becomes larger in more mature neurons. (F)

Bar plots summarizing the neuronal resting membrane potential at the two temporal points. (G) Representative traces of action potentials in neurons at 8 (black) and 12 (blue) DIV neurons, elicited by current injection (the protocol is shown below). Bar plots summarizing the AP amplitudes (H) and half-width (I) in the two conditions.

In all bar plots dots superimposed to the bars are single values and * $P < 0.05$.

FIGURE 3: Electrophysiological characterization of unitary postsynaptic currents at 12 DIV

(A) Sketch of the experimental setting for pair recordings. (B) Currents injections (above, 4 ms, 1 nA@20Hz) elicit action potentials in the presynaptic neuron (middle). Below, representative averaged traces of evoked unitary EPSCs or IPSCs recorded from postsynaptic neurons. (C) Bar plot summarizing the percentage of monosynaptically coupled pairs at 12 DIV. (D) Histograms showing the percentage of different type of connections in monosynaptically coupled pairs.

FIGURE 4: Acute application of s-GO interferes with glutamatergic activity of amygdalar neurons (A) Sketch of the experimental setting. (B) Top, representative traces of the spontaneous synaptic activity during acute application of saline (left) or s-GO (right). Arrows represent the puff ejection (see methods). Bottom, magnified traces of the spontaneous synaptic activity recorded before and after saline (left) and s-GO (right) applications. Box plots summarize the sPSC frequency (C) and amplitude (D) before and after the acute application of saline (black) and s-GO (orange). sPSCs frequency is increased only by treatment with s-GO. Summary graphs of the change in sPSCs (E), sEPSCs(F) and sIPSCs (G)

frequency after the saline (black circle) and s-GO (orange square) puff. s-GO affect selectively the frequency of EPSCs. * $P < 0.05$.

FIGURE 1

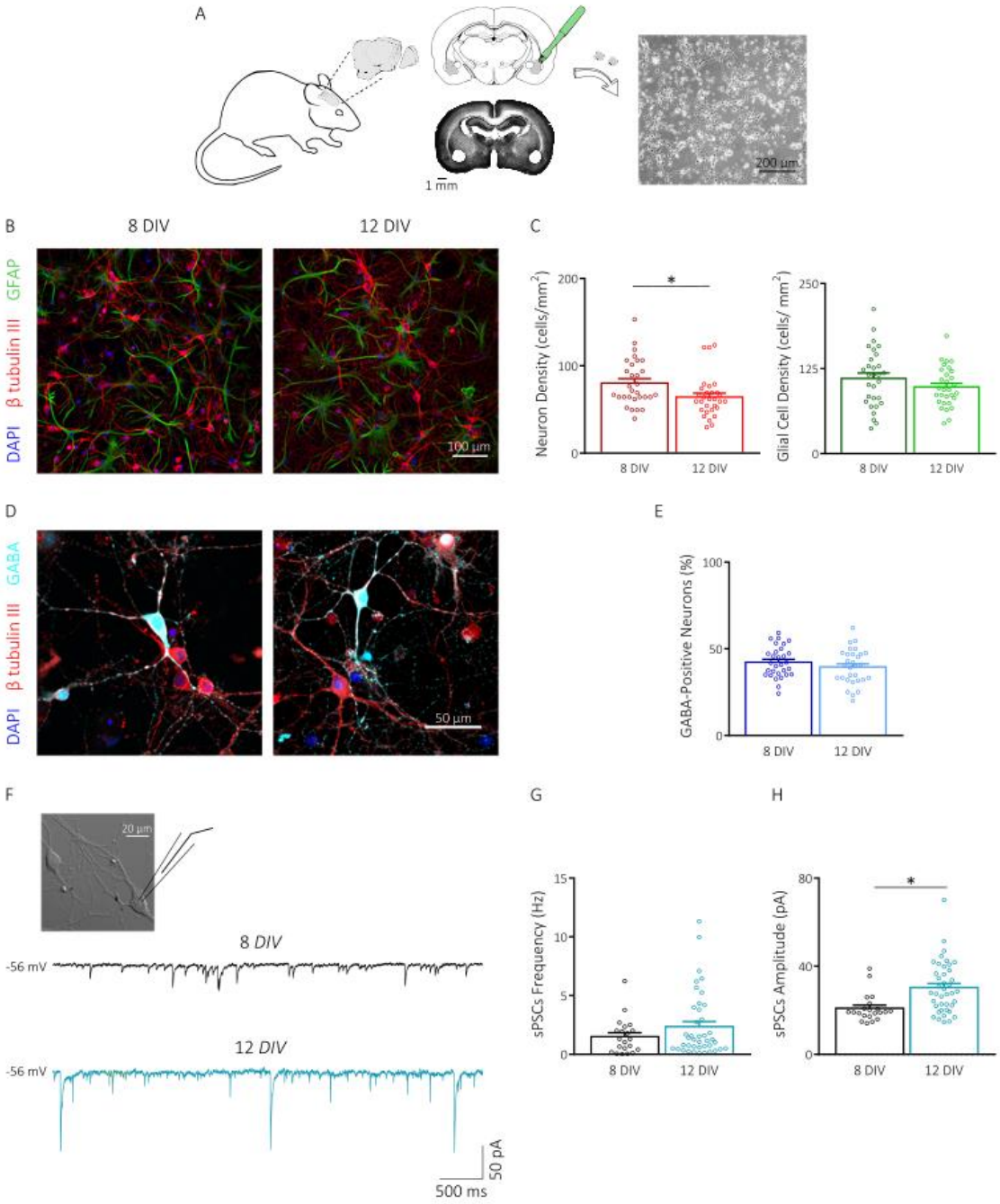
A
1 mm
200 µm
B
8 DIV
12 DIV
GFAP
β tubulin III
DAPI
100 µm
C
Neuron Density (cells/mm²)
Glial Cell Density (cells/ mm²)
8 DIV
12 DIV
D
GABA
β tubulin III
DAPI
50 µm
E
GABA-Positive Neurons (%)
F
20 µm
8 DIV
-56 mV
12 DIV
50 pA
500 ms
G
sPSCs Frequency (Hz)
H
sPSCs Amplitude (pA)

FIGURE 2

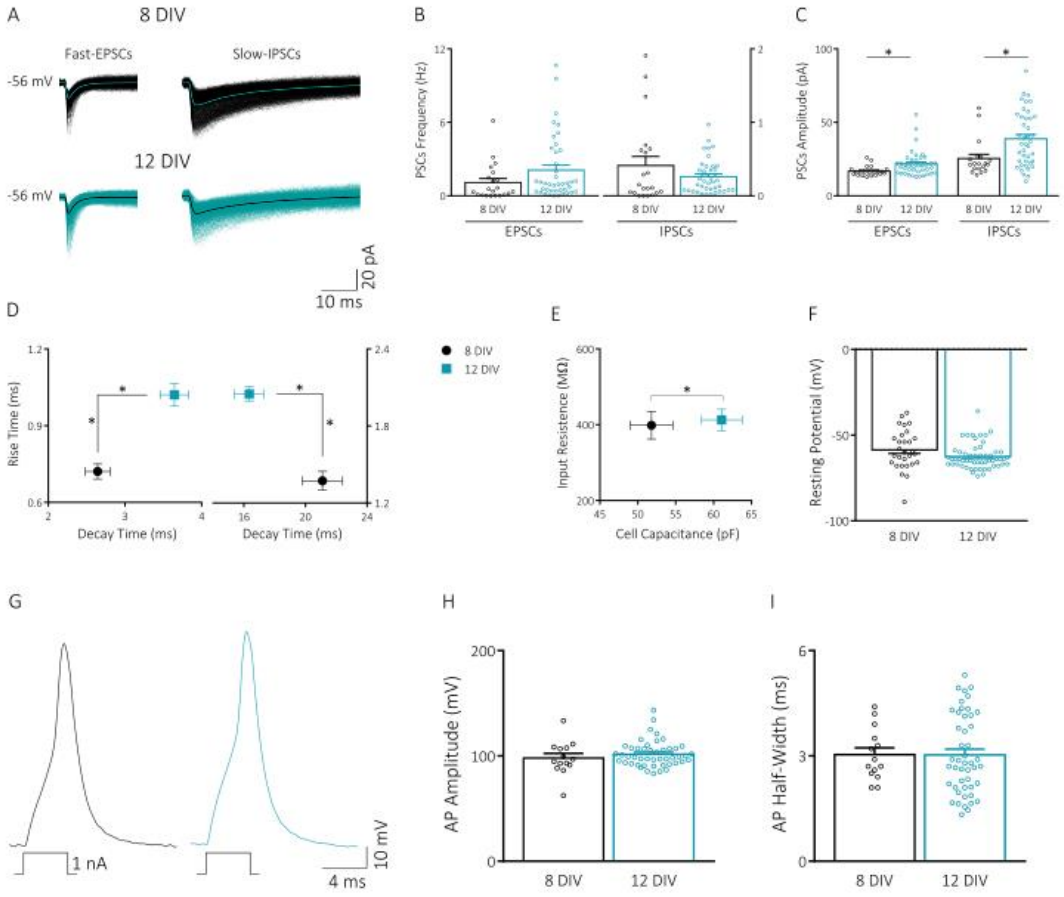
A
8 DIV
Fast-EPSCs
Slow-IPSCs
-56 mV
12 DIV
-56 mV
20 pA
10 ms
B
PSCs Frequency (Hz)
8 DIV
12 DIV
EPSCs
IPSCs
C
PSCs Amplitude (pA)
EPSCs
IPSCs
D
Rise Time (ms)
Decay Time (ms)
Decay Time (ms)
8 DIV
12 DIV
E
Input Resistence (MΩ)
Cell Capacitance (pF)
F
Resting Potential (mV)
8 DIV
12 DIV
G
1 nA
10 mV
4 ms
H
AP Amplitude (mV)
8 DIV
12 DIV
I
AP Half-Width (ms)
8 DIV
12 DIV

FIGURE 3

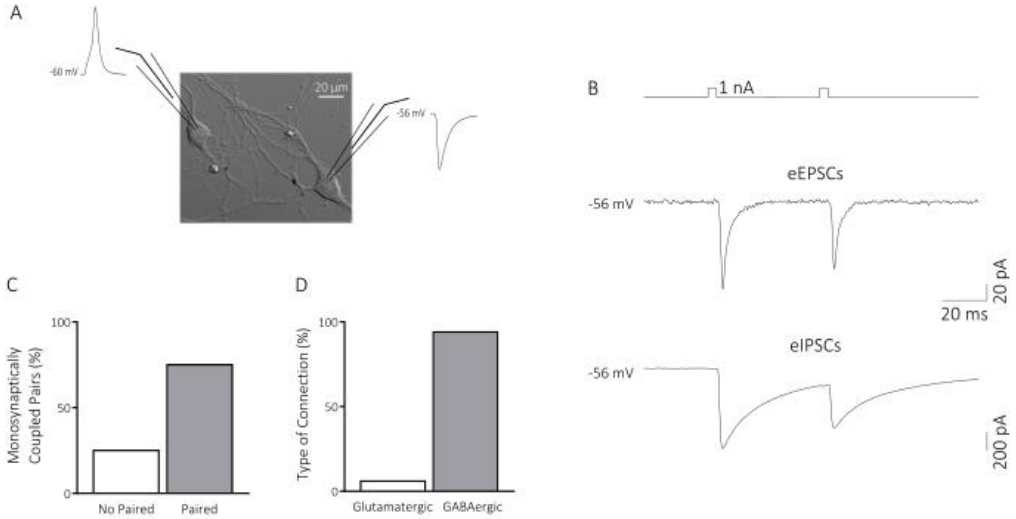
A
-60 mV
20 µm
-56 mV
B
1 nA
eEPSCs
-56 mV
20 pA
20 ms
eIPSCs
-56 mV
200 pA
C
Monosynaptically Coupled Pairs (%)
100
50
0
No Paired
Paired
D
Type of Connection (%)
100
50
0
Glutamatergic
GABAergic

FIGURE 4

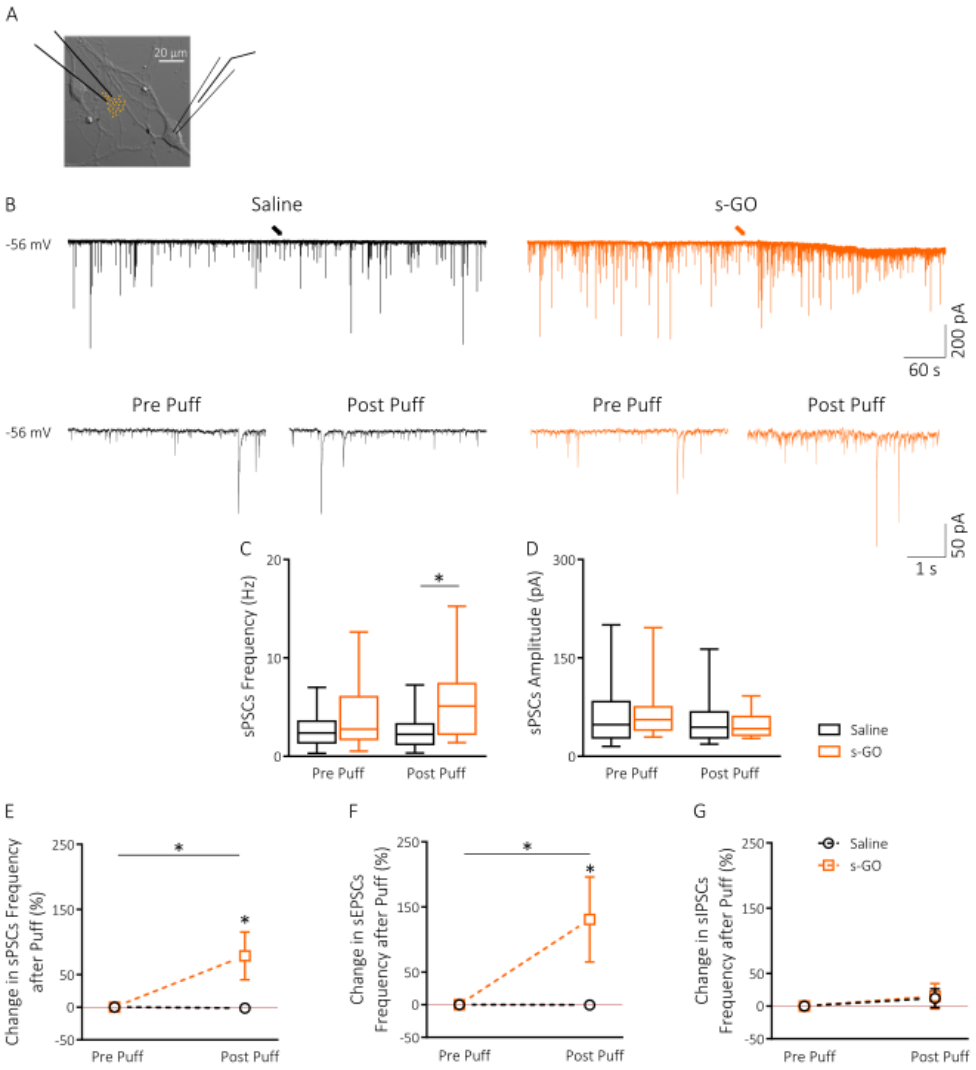
A
20 µm
B
Saline
s-GO
-56 mV
200 pA
60 s
Pre Puff
Post Puff
-56 mV
50 pA
1 s
C
sPSCs Frequency (Hz)
Pre Puff
Post Puff
D
sPSCs Amplitude (pA)
Saline
s-GO
E
Change in sPSCs Frequency after Puff (%)
F
Change in sEPSCs Frequency after Puff (%)
G
Change in sIPSCs Frequency after Puff (%)

CONCLUSIVE REMARKS

Modern medicine witnesses a great need for new and original therapies to cope with the growing demand of more effective and safer treatments for pathological conditions (Bramini et al., 2018).

Nanotechnology might offer exiting possibilities for biomedical applications, such as using engineered nanomaterials for drug and gene delivery (Bhirde et al., 2009; Chen et al., 2015; Maeda-Mamiya et al., 2010), imaging and diagnostics (De La Zerda et al., 2008; Ghosh et al., 2014) or tissue engineering (Bosi et al., 2015; Thalhammer et al., 2010). Among all nanomaterials, graphene and its derivates have attracted an increasing attention in biomedical applications, in particular in neuroscience, in the last few years (Kostarelos et al., 2017; Reina et al., 2017). This attention is mainly due to GBNs extraordinary physicochemical features such as thermo-electrical conductivity, mechanical flexibility, transparency and good biocompatibility.

However, before to exploit GBNs into potential therapeutic application, a deeper understanding of the interaction between GBNs and the intricate system underlying neural cell functions and signaling is crucial. In fact, GBNs, interfacing with cellular and subcellular structures, might alter complex biological processes including the neuronal synaptic transmission.

In this context, throughout my PhD I studied different neuron-nanomaterial interactions which results show the ability of promising GBNs, in particular single layer graphene and graphene oxide, to modulate the sophisticated neural circuit machinery.

In the first work, we showed, exploiting elastomeric 3D scaffolds, the ability of graphene to alter the neuronal circuit formation into 3D hippocampal cultures. In particular, we hypothesized that the development of the neuronal network in a 3D environment and in presence of graphene altered the maturation of GABAergic inhibition leading to changes in excitatory/inhibitory balance.

This peculiar impact on networks dynamics was not observed neither in 3D PDMS cultures nor in 2D graphene one underlying the complex interaction between graphene and cells when they are able to grow in third dimension.

Despite the fact that future studies are needed to deeper understand the effect of graphene in 3D configuration, our work underlines the possibility to exploit nanomaterials and their physical and topographical features to modulate the neuronal network for future biomedical applications.

In the second work, we reported the ability of s-GO nanosheets to modulate selectively the excitatory glutamatergic transmission of isolated amygdala neurons when acutely applied, evaluated as an increment in the spontaneous EPSC frequency if compared with the baseline. These results have been obtained upon a detailed characterization, by immunofluorescence and electrophysiological techniques, of dissociated amygdala cultures which allowed us to better study the synaptic activity at the single cell level (Godfrey et al., 1975).

Based on previous published works, the prolonged application of s-GO to hippocampal neurons led to a decrease in glutamatergic synaptic activity due to a depletion of the neurotransmitter from the presynaptic compartment (Rauti et al., 2016, 2019).

In this context, it might be possible that the increment of ESPC frequency after the acute s-GO application is only a transient effect and that, as a result of a prolonged exposure, the graphene derivate is capable of downregulating the neuronal activity.

Surely, more experiments are needed however, if the selective ability of s-GO to alter the glutamatergic synapsis reported in other brain regions will be confirmed in the amygdala, this nanomaterial might be considered as an innovative tool for biomedical applications.

In particular, s-GO could be adopted for the selective modulation of the glutamatergic circuits whose physiological activity is altered in ArDs (Cortese and Phan, 2005; Wierońska et al., 2011).

Summarizing, the results obtained during my PhD program brought new and interesting characterizations about the peculiar interactions between neurons and GBNs which might be useful for future research studies, both *in vitro* and *in vivo*, and for the development of new tools for biomedical applications.

REFERENCES

Adolphs, R., Tranel, D., Damasio, H., and Damasio, A. (1994). Impaired recognition of emotion in facial expressions following bilateral damage to the human amygdala. Nature *372*, 669–672.

Ajayan, P.M. (1999). Nanotubes from Carbon. Chem. Rev. *99*, 1787–1800.

Aleksenskii, A.E., Baidakova, M.V., Vul', A.Ya., and Siklitskii, V.I. (1999). The structure of diamond nanoclusters. Phys. Solid State *41*, 668–671.

Al-Jamal, K.T., Gherardini, L., Bardi, G., Nunes, A., Guo, C., Bussy, C., Herrero, M.A., Bianco, A., Prato, M., Kostarelos, K., et al. (2011). Functional motor recovery from brain ischemic insult by carbon nanotube-mediated siRNA silencing. Proc. Natl. Acad. Sci. *108*, 10952–10957.

Aurand, E.R., Usmani, S., Medelin, M., Scaini, D., Bosi, S., Rosselli, F.B., Donato, S., Tromba, G., Prato, M., and Ballerini, L. (2018). Nanostructures to Engineer 3D Neural-Interfaces: Directing Axonal Navigation toward Successful Bridging of Spinal Segments. Adv. Funct. Mater. *28*, 1700550.

Bai, H.-J., Gou, H.-L., Xu, J.-J., and Chen, H.-Y. (2010). Molding a Silver Nanoparticle Template on Polydimethylsiloxane to Efficiently Capture Mammalian Cells. Langmuir *26*, 2924–2929.

Baldrighi, M., Trusel, M., Tonini, R., and Giordani, S. (2016). Carbon Nanomaterials Interfacing with Neurons: An In vivo Perspective. Front. Neurosci. *10*.

Balogh, L.P. (2015). Caging cancer. Nanomedicine Nanotechnol. Biol. Med. *11*, 867–869.

Bellido, E.P., and Seminario, J.M. (2010). Molecular Dynamics Simulations of Folding of Supported Graphene. J. Phys. Chem. C *114*, 22472–22477.

Besançon, O.G., Tytgat, G.A.M., Meinsma, R., Leen, R., Hoebink, J., Kalayda, G.V., Jaehde, U., Caron, H.N., and van Kuilenburg, A.B.P. (2012). Synergistic interaction between cisplatin and gemcitabine in neuroblastoma cell lines and multicellular tumor spheroids. Cancer Lett. *319*, 23–30.

Bhattacharya, K., Andón, F.T., El-Sayed, R., and Fadeel, B. (2013). Mechanisms of carbon nanotube-induced toxicity: Focus on pulmonary inflammation. Adv. Drug Deliv. Rev. *65*, 2087–2097.

Bhirde, A.A., Patel, V., Gavard, J., Zhang, G., Sousa, A.A., Masedunskas, A., Leapman, R.D., Weigert, R., Gutkind, J.S., and Rusling, J.F. (2009). Targeted Killing of Cancer Cells *in Vivo* and *in Vitro* with EGF-Directed Carbon Nanotube-Based Drug Delivery. ACS Nano *3*, 307–316.

Bianco, A. (2013). Graphene: Safe or Toxic? The Two Faces of the Medal. Angew. Chem. Int. Ed. *52*, 4986–4997.

Biswas, P., and Wu, C.-Y. (2005). Nanoparticles and the Environment. J. Air Waste Manag. Assoc. *55*, 708–746.

Bitounis, D., Ali-Boucetta, H., Hong, B.H., Min, D.-H., and Kostarelos, K. (2013). Prospects and Challenges of Graphene in Biomedical Applications. Adv. Mater. *25*, 2258–2268.

Blackshaw, S.E., Arkison, S., Cameron, C., and Davies, J.A. (1997). Promotion of regeneration and axon growth following injury in an invertebrate nervous system by the use of three–dimensional collagen gels. Proc. R. Soc. Lond. B Biol. Sci. *264*, 657–661.

Borowska, S., and Brzóska, M.M. (2015). Metals in cosmetics: implications for human health: Metals in cosmetics. J. Appl. Toxicol. *35*, 551–572.

Bosi, S., Rauti, R., Laishram, J., Turco, A., Lonardoni, D., Nieus, T., Prato, M., Scaini, D., and Ballerini, L. (2015). From 2D to 3D: novel nanostructured scaffolds to investigate signalling in reconstructed neuronal networks. Sci. Rep. *5*.

Bozza, A., Coates, E.E., Incitti, T., Ferlin, K.M., Messina, A., Menna, E., Bozzi, Y., Fisher, J.P., and Casarosa, S. (2014). Neural differentiation of pluripotent cells in 3D alginate-based cultures. Biomaterials *35*, 4636–4645.

Bramini, M., Sacchetti, S., Armirotti, A., Rocchi, A., Vázquez, E., León Castellanos, V., Bandiera, T., Cesca, F., and Benfenati, F. (2016). Graphene Oxide Nanosheets Disrupt Lipid Composition, Ca^{2+} Homeostasis, and Synaptic Transmission in Primary Cortical Neurons. ACS Nano *10*, 7154–7171.

Bramini, M., Alberini, G., Colombo, E., Chiacchiaretta, M., DiFrancesco, M.L., Maya-Vetencourt, J.F., Maragliano, L., Benfenati, F., and Cesca, F. (2018). Interfacing Graphene-Based Materials With Neural Cells. Front. Syst. Neurosci. *12*.

Briscoe, J., Marinovic, A., Sevilla, M., Dunn, S., and Titirici, M. (2015). Biomass-Derived Carbon Quantum Dot Sensitizers for Solid-State Nanostructured Solar Cells. Angew. Chem. Int. Ed. *54*, 4463–4468.

Cahill, L., and McGaugh, J.L. (1998). Mechanisms of emotional arousal and lasting declarative memory. Trends Neurosci. *21*, 294–299.

Cellot, G., Cilia, E., Cipollone, S., Rancic, V., Sucapane, A., Giordani, S., Gambazzi, L., Markram, H., Grandolfo, M., Scaini, D., et al. (2009). Carbon nanotubes might improve neuronal performance by favouring electrical shortcuts. Nat. Nanotechnol. *4*, 126–133.

Chang, E.F. (2015). Towards Large-Scale, Human-Based, Mesoscopic Neurotechnologies. Neuron *86*, 68–78.

Charlier, J.-C. (2002). Defects in Carbon Nanotubes. Acc. Chem. Res. *35*, 1063–1069.

Chen, D., Dougherty, C.A., Zhu, K., and Hong, H. (2015). Theranostic applications of carbon nanomaterials in cancer: Focus on imaging and cargo delivery. J. Controlled Release *210*, 230–245.

Chen, Y., Star, A., and Vidal, S. (2013). Sweet carbon nanostructures: carbohydrate conjugates with carbon nanotubes and graphene and their applications. Chem Soc Rev *42*, 4532–4542.

Cheng, C., Li, S., Thomas, A., Kotov, N.A., and Haag, R. (2017). Functional Graphene Nanomaterials Based Architectures: Biointeractions, Fabrications, and Emerging Biological Applications. Chem. Rev. *117*, 1826–1914.

Choi, H.K., Won, L., and Heller, A. (1993). Dopaminergic neurons grown in three-dimensional reaggregate culture for periods of up to one year. J. Neurosci. Methods *46*, 233–244.

Choi, Y.J., Park, J., and Lee, S.-H. (2013). Size-controllable networked neurospheres as a 3D neuronal tissue model for Alzheimer's disease studies. Biomaterials *34*, 2938–2946.

Chow, E.K., Zhang, X.-Q., Chen, M., Lam, R., Robinson, E., Huang, H., Schaffer, D., Osawa, E., Goga, A., and Ho, D. (2011). Nanodiamond Therapeutic Delivery Agents Mediate Enhanced Chemoresistant Tumor Treatment. Sci. Transl. Med. *3*, 73ra21-73ra21.

Compton, O.C., and Nguyen, S.T. (2010). Graphene Oxide, Highly Reduced Graphene Oxide, and Graphene: Versatile Building Blocks for Carbon-Based Materials. Small *6*, 711–723.

Cong, H.-P., Chen, J.-F., and Yu, S.-H. (2014). Graphene-based macroscopic assemblies and architectures: an emerging material system. Chem Soc Rev *43*, 7295–7325.

Cortese, B.M., and Phan, K.L. (2005). The Role of Glutamate in Anxiety and Related Disorders. CNS Spectr. *10*, 820–830.

Cote, L.J., Kim, F., and Huang, J. (2009). Langmuir−Blodgett Assembly of Graphite Oxide Single Layers. J. Am. Chem. Soc. *131*, 1043–1049.

Daud, M.F.B., Pawar, K.C., Claeyssens, F., Ryan, A.J., and Haycock, J.W. (2012). An aligned 3D neuronal-glial co-culture model for peripheral nerve studies. Biomaterials *33*, 5901–5913.

Daulton, T.L., Kirk, M.A., Lewis, R.S., and Rehn, L.E. (2001). Production of nanodiamonds by high-energy ion irradiation of graphite at room temperature. Nucl. Instrum. Methods Phys. Res. Sect. B Beam Interact. Mater. At. *175–177*, 12–20.

De La Zerda, A., Zavaleta, C., Keren, S., Vaithilingam, S., Bodapati, S., Liu, Z., Levi, J., Smith, B.R., Ma, T.-J., Oralkan, O., et al. (2008). Carbon nanotubes as photoacoustic molecular imaging agents in living mice. Nat. Nanotechnol. *3*, 557–562.

Dellinger, A., Zhou, Z., Connor, J., Madhankumar, A., Pamujula, S., Sayes, C.M., and Kepley, C.L. (2013). Application of fullerenes in nanomedicine: an update. Nanomed. *8*, 1191–1208.

Delogu, L.G., Vidili, G., Venturelli, E., Menard-Moyon, C., Zoroddu, M.A., Pilo, G., Nicolussi, P., Ligios, C., Bedognetti, D., Sgarrella, F., et al. (2012). Functionalized multiwalled carbon nanotubes as ultrasound contrast agents. Proc. Natl. Acad. Sci. *109*, 16612–16617.

Dikin, D.A., Stankovich, S., Zimney, E.J., Piner, R.D., Dommett, G.H.B., Evmenenko, G., Nguyen, S.T., and Ruoff, R.S. (2007). Preparation and characterization of graphene oxide paper. Nature *448*, 457–460.

Dillon, G.P., Xiaojun Yu, Sridharan, A., Ranieri, J.P., and Bellamkonda, R.V. (1998). The influence of physical structure and charge on neurite extension in a 3D hydrogel scaffold. J. Biomater. Sci. Polym. Ed. *9*, 1049–1069.

Ding, X., Liu, H., and Fan, Y. (2015). Graphene-Based Materials in Regenerative Medicine. Adv. Healthc. Mater. *4*, 1451–1468.

Dingle, Y.-T.L., Boutin, M.E., Chirila, A.M., Livi, L.L., Labriola, N.R., Jakubek, L.M., Morgan, J.R., Darling, E.M., Kauer, J.A., and Hoffman-Kim, D. (2015). Three-Dimensional Neural Spheroid Culture: An *In Vitro* Model for Cortical Studies. Tissue Eng. Part C Methods *21*, 1274–1283.

Docter, D., Westmeier, D., Markiewicz, M., Stolte, S., Knauer, S.K., and Stauber, R.H. (2015). The nanoparticle biomolecule corona: lessons learned – challenge accepted? Chem. Soc. Rev. *44*, 6094–6121.

Dong, H., Jin, M., Liu, Z., Xiong, H., Qiu, X., Zhang, W., and Guo, Z. (2016). In vitro and in vivo brain-targeting chemo-photothermal therapy using graphene oxide conjugated with transferrin for Gliomas. Lasers Med. Sci. *31*, 1123–1131.

Dresselhaus, M., Dresselhaus, G., and Eklund, P. (1996). Science of fullerenes and carbon nanotubes: their properties and applications (Academic Press, Boston, MA).

Fabbro, A., Scaini, D., León, V., Vázquez, E., Cellot, G., Privitera, G., Lombardi, L., Torrisi, F., Tomarchio, F., Bonaccorso, F., et al. (2016). Graphene-Based Interfaces Do Not Alter Target Nerve Cells. ACS Nano *10*, 615–623.

Fahmi, T., Branch, L.D., Nima, Z.A., Jang, D.S., Savenka, A.V., Biris, A.S., and Basnakian, A.G. (2017). Mechanism of graphene-induced cytotoxicity: Role of endonucleases: Mechanism of graphene-induced cytotoxicity. J. Appl. Toxicol. *37*, 1325–1332.

Farrera, C., and Fadeel, B. (2015). It takes two to tango: Understanding the interactions between engineered nanomaterials and the immune system. Eur. J. Pharm. Biopharm. *95*, 3–12.

Feng, L., and Liu, Z. (2011). Graphene in biomedicine: opportunities and challenges. Nanomed. *6*, 317–324.

Feng, L., Wu, L., and Qu, X. (2013). New Horizons for Diagnostics and Therapeutic Applications of Graphene and Graphene Oxide. Adv. Mater. *25*, 168–186.

Fernando, K.A.S., Sahu, S., Liu, Y., Lewis, W.K., Guliants, E.A., Jafariyan, A., Wang, P., Bunker, C.E., and Sun, Y.-P. (2015). Carbon Quantum Dots and Applications in Photocatalytic Energy Conversion. ACS Appl. Mater. Interfaces *7*, 8363–8376.

Fu, C.-C., Lee, H.-Y., Chen, K., Lim, T.-S., Wu, H.-Y., Lin, P.-K., Wei, P.-K., Tsao, P.-H., Chang, H.-C., and Fann, W. (2007). Characterization and application of single fluorescent nanodiamonds as cellular biomarkers. Proc. Natl. Acad. Sci. *104*, 727–732.

Gallagher, M., and Holland, P.C. (1994). The amygdala complex: multiple roles in associative learning and attention. Proc. Natl. Acad. Sci. *91*, 11771–11776.

Ganella, D.E., and Kim, J.H. (2014). Developmental rodent models of fear and anxiety: from neurobiology to pharmacology: Pharmacological studies in developmental anxiety. Br. J. Pharmacol. *171*, 4556–4574.

Garbayo, E., Mendoza, A., and Blanco-Prieto, M. (2014). Diagnostic and Therapeutic Uses of Nanomaterials in the Brain. Curr. Med. Chem. *21*, 4100–4131.

Gaudiana, R., and Brabec, C. (2008). Fantastic plastic: Organic materials. Nat. Photonics *2*, 287–289.

Geim, A.K. (2009). Graphene: Status and Prospects. Science *324*, 1530–1534.

Georgakilas, V., Tiwari, J.N., Kemp, K.C., Perman, J.A., Bourlinos, A.B., Kim, K.S., and Zboril, R. (2016). Noncovalent Functionalization of Graphene and Graphene Oxide for Energy Materials, Biosensing, Catalytic, and Biomedical Applications. Chem. Rev. *116*, 5464–5519.

Ghosh, D., Bagley, A.F., Na, Y.J., Birrer, M.J., Bhatia, S.N., and Belcher, A.M. (2014). Deep, noninvasive imaging and surgical guidance of submillimeter tumors using targeted M13-stabilized single-walled carbon nanotubes. Proc. Natl. Acad. Sci. *111*, 13948–13953.

Giugliano, M., Prato, M., and Ballerini, L. (2008). Nanomaterial/neuronal hybrid system for functional recovery of the CNS. Drug Discov. Today Dis. Models *5*, 37–43.

Godfrey, E.W., Nelson, P.G., Schrier, B.K., Breuer, A.C., and Ransom, B.R. (1975). Neurons from fetal rat brain in a new cell culture system: A multidisciplinary analysis. Brain Res. *90*, 1–21.

Goenka, S., Sant, V., and Sant, S. (2014). Graphene-based nanomaterials for drug delivery and tissue engineering. J. Controlled Release *173*, 75–88.

Gooding, J.J. (2005). Nanostructuring electrodes with carbon nanotubes: A review on electrochemistry and applications for sensing. Electrochimica Acta *50*, 3049–3060.

Gross, P.G., Kartalov, E.P., Scherer, A., and Weiner, L.P. (2007). Applications of microfluidics for neuronal studies. J. Neurol. Sci. *252*, 135–143.

Guldi, D.M., and Prato, M. (2000). Excited-State Properties of C_{60} Fullerene Derivatives. Acc. Chem. Res. *33*, 695–703.

Guo, W., Wang, S., Yu, X., Qiu, J., Li, J., Tang, W., Li, Z., Mou, X., Liu, H., and Wang, Z. (2016). Construction of a 3D rGO–collagen hybrid scaffold for enhancement of the neural differentiation of mesenchymal stem cells. Nanoscale *8*, 1897–1904.

Hamann, S.B., Ely, T.D., Grafton, S.T., and Kilts, C.D. (1999). Amygdala activity related to enhanced memory for pleasant and aversive stimuli. Nat. Neurosci. *2*, 289–293.

Han, J.-W., Kim, B., Li, J., and Meyyappan, M. (2013). Flexible, compressible, hydrophobic, floatable, and conductive carbon nanotube-polymer sponge. Appl. Phys. Lett. *102*, 051903.

Hatsopoulos, N.G., and Donoghue, J.P. (2009). The Science of Neural Interface Systems. Annu. Rev. Neurosci. *32*, 249–266.

Hollenbeck, P.J., and Bamburg, J.R. (2003). Nerons: Method and Application for the Cell Biologist (Method Cell Biology).

Hsieh, C.-T., and Chen, W.-Y. (2011). Water/oil repellency and work of adhesion of liquid droplets on graphene oxide and graphene surfaces. Surf. Coat. Technol. *205*, 4554–4561.

Iijima, S. (1991). Helical microtubules of graphitic carbon. Nature *354*, 56–58.

Iijima, S., and Ichihashi, T. (1993). Single-shell carbon nanotubes of 1-nm diameter. Nature *363*, 603–605.

Iverson, N.M., Barone, P.W., Shandell, M., Trudel, L.J., Sen, S., Sen, F., Ivanov, V., Atolia, E., Farias, E., McNicholas, T.P., et al. (2013). In vivo biosensing via tissue-localizable near-infrared-fluorescent single-walled carbon nanotubes. Nat. Nanotechnol. *8*, 873–880.

Janak, P.H., and Tye, K.M. (2015). From circuits to behaviour in the amygdala. Nature *517*, 284–292.

Jarvis, E.D., Güntürkün, O., Bruce, L., Csillag, A., Karten, H., Kuenzel, W., Medina, L., Paxinos, G., Perkel, D.J., Shimizu, T., et al. (2005). Avian brains and a new understanding of vertebrate brain evolution. Nat. Rev. Neurosci. *6*, 151–159.

Jensen, A.W., Wilson, S.R., and Schuster, D.I. (1996). Biological applications of fullerenes. Bioorg. Med. Chem. *4*, 767–779.

John, A.A., Vellayappan, M.V., Balaji, A., Mohandas, H., and Subramanian, A.P. (2015). Carbon nanotubes and graphene as emerging candidates in neuroregeneration and neurodrug delivery. Int. J. Nanomedicine 4267.

Johnston, J.B. (1923). Further contributions to the study of the evolution of the forebrain. V. Survey of forebrain morphology. J. Comp. Neurol. *36*, 143–192.

Kaneda, M., and Akaike, N. (1989). The low-threshold Ca current in isolated amygdaloid neurons in the rat. Brain Res. *497*, 187–190.

Kang, C., Patel, M., Rangasamy, B., Jung, K.-N., Xia, C., Shi, S., and Choi, W. (2015). Three-dimensional carbon nanotubes for high capacity lithium-ion batteries. J. Power Sources *299*, 465–471.

Kang, S. -g., Zhou, G., Yang, P., Liu, Y., Sun, B., Huynh, T., Meng, H., Zhao, L., Xing, G., Chen, C., et al. (2012). Molecular mechanism of pancreatic tumor metastasis inhibition by Gd@C82(OH)22 and its implication for de novo design of nanomedicine. Proc. Natl. Acad. Sci. *109*, 15431–15436.

Katz, E., and Willner, I. (2004). Biomolecule-Functionalized Carbon Nanotubes: Applications in Nanobioelectronics. ChemPhysChem *5*, 1084–1104.

Keung, A.J., Healy, K.E., Kumar, S., and Schaffer, D.V. (2010). Biophysics and dynamics of natural and engineered stem cell microenvironments: Natural and engineered stem cell microenvironments. Wiley Interdiscip. Rev. Syst. Biol. Med. *2*, 49–64.

Killcross, S., Robbins, T.W., and Everitt, B.J. (1997). Different types of fear-conditioned behaviour mediated by separate nuclei within amygdala. Nature *388*, 377–380.

Kirner, S., Sekita, M., and Guldi, D.M. (2014). 25th Anniversary Article: 25 Years of Fullerene Research in Electron Transfer Chemistry. Adv. Mater. *26*, 1482–1493.

Knight, E., and Przyborski, S. (2015). Advances in 3D cell culture technologies enabling tissue-like structures to be created *in vitro*. J. Anat. *227*, 746–756.

Ko, K.R., and Frampton, J.P. (2016). Developments in 3D neural cell culture models: the future of neurotherapeutics testing? Expert Rev. Neurother. *16*, 739–741.

Kostarelos, K., and Novoselov, K.S. (2014). Exploring the Interface of Graphene and Biology. Science *344*, 261–263.

Kostarelos, K., Lacerda, L., Pastorin, G., Wu, W., Wieckowski, S., Luangsivilay, J., Godefroy, S., Pantarotto, D., Briand, J.-P., Muller, S., et al. (2007). Cellular uptake of functionalized carbon nanotubes is independent of functional group and cell type. Nat. Nanotechnol. *2*, 108–113.

Kostarelos, K., Vincent, M., Hebert, C., and Garrido, J.A. (2017). Graphene in the Design and Engineering of Next-Generation Neural Interfaces. Adv. Mater. *29*, 1700909.

Krettek, J.E., and Price, J.L. (1978). A description of the amygdaloid complex in the rat and cat with observations on intra-amygdaloid axonal connections. J. Comp. Neurol. *178*, 255–279.

Kroto, H.W., Heath, J.R., O'Brien, S.C., Curl, R.F., and Smalley, R.E. (1985). C60: Buckminsterfullerene. Nature *318*, 162–163.

Ku, S.H., Lee, M., and Park, C.B. (2013). Carbon-Based Nanomaterials for Tissue Engineering. Adv. Healthc. Mater. *2*, 244–260.

Kumar, A., Tan, A., Wong, J., Spagnoli, J.C., Lam, J., Blevins, B.D., G, N., Thorne, L., Ashkan, K., Xie, J., et al. (2017). Nanotechnology for Neuroscience: Promising Approaches for Diagnostics, Therapeutics and Brain Activity Mapping. Adv. Funct. Mater. *27*, 1700489.

Lanuza, E., Belekhova, M., Martínez-Marcos, A., Font, C., and Martínez-García, F. (1998). Identification of the reptilian basolateral amygdala: an anatomical investigation of the afferents to the posterior dorsal ventricular ridge of the lizard *Podarcis hispanica* : Basolateral amygdala of lizard. Eur. J. Neurosci. *10*, 3517–3534.

LaPlaca, M., Vernekar, N., Shoemaker, J., and Cullen, D. (2010). Three-Dimensional Neuronal Cultures. pp. 187–204.

LeDoux, J. (2007). The amygdala. Curr. Biol. *17*, R868–R874.

Lee, C., Wei, X., Kysar, J.W., and Hone, J. (2008). Measurement of the Elastic Properties and Intrinsic Strength of Monolayer Graphene. Science *321*, 385–388.

Li, G.N., Livi, L.L., Gourd, C.M., Deweerd, E.S., and Hoffman-Kim, D. (2007). Genomic and Morphological Changes of Neuroblastoma Cells in Response to Three-Dimensional Matrices. Tissue Eng. *13*, 1035–1047.

Li, H., Kang, Z., Liu, Y., and Lee, S.-T. (2012). Carbon nanodots: synthesis, properties and applications. J. Mater. Chem. *22*, 24230.

Li, N., Zhang, Q., Gao, S., Song, Q., Huang, R., Wang, L., Liu, L., Dai, J., Tang, M., and Cheng, G. (2013). Three-dimensional graphene foam as a biocompatible and conductive scaffold for neural stem cells. Sci. Rep. *3*.

Li, N., Xiao, T., Zhang, Z., He, R., Wen, D., Cao, Y., Zhang, W., and Chen, Y. (2015a). A 3D graphene oxide microchip and a Au-enwrapped silica nanocomposite-based supersandwich cytosensor toward capture and analysis of circulating tumor cells. Nanoscale *7*, 16354–16360.

Li, Y., Wu, J., and Chopra, N. (2015b). Nano-carbon-based hybrids and heterostructures: progress in growth and application for lithium-ion batteries. J. Mater. Sci. *50*, 7843–7865.

Lim, M.-H., Jeung, I.C., Jeong, J., Yoon, S.-J., Lee, S.-H., Park, J., Kang, Y.-S., Lee, H., Park, Y.-J., Lee, H.G., et al. (2016). Graphene oxide induces apoptotic cell death in endothelial cells by activating autophagy via calcium-dependent phosphorylation of c-Jun N-terminal kinases. Acta Biomater. *46*, 191–203.

Lim, S.Y., Shen, W., and Gao, Z. (2015). Carbon quantum dots and their applications. Chem. Soc. Rev. *44*, 362–381.

Lin, C.-H., Huang, Y.-C., Tsai, J.-J., and Gean, P.-W. (2001). Modulation of voltage-dependent calcium currents by serotonin in acutely isolated rat amygdala neurons. Synapse *41*, 351–359.

Littlejohn, S.D. (2014). Electrical Properties of Graphite Nanoparticles in Silicone (Cham: Springer International Publishing).

Lockman, P.R., Oyewumi, M.O., Koziara, J.M., Roder, K.E., Mumper, R.J., and Allen, D.D. (2003). Brain uptake of thiamine-coated nanoparticles. J. Controlled Release *93*, 271–282.

López-Dolado, E., González-Mayorga, A., Portolés, M.T., Feito, M.J., Ferrer, M.L., del Monte, F., Gutiérrez, M.C., and Serrano, M.C. (2015). Subacute Tissue Response to 3D Graphene Oxide Scaffolds Implanted in the Injured Rat Spinal Cord. Adv. Healthc. Mater. *4*, 1861–1868.

López-Dolado, E., González-Mayorga, A., Gutiérrez, M.C., and Serrano, M.C. (2016). Immunomodulatory and angiogenic responses induced by graphene oxide scaffolds in chronic spinal hemisected rats. Biomaterials *99*, 72–81.

Lu, J., Cheng, C., He, Y.-S., Lyu, C., Wang, Y., Yu, J., Qiu, L., Zou, D., and Li, D. (2016). Multilayered Graphene Hydrogel Membranes for Guided Bone Regeneration. Adv. Mater. *28*, 4025–4031.

Lu, X., Feng, L., Akasaka, T., and Nagase, S. (2012). Current status and future developments of endohedral metallofullerenes. Chem. Soc. Rev. *41*, 7723.

Luo, J., Cote, L.J., Tung, V.C., Tan, A.T.L., Goins, P.E., Wu, J., and Huang, J. (2010). Graphene Oxide Nanocolloids. J. Am. Chem. Soc. *132*, 17667–17669.

Lv, M., Zhang, Y., Liang, L., Wei, M., Hu, W., Li, X., and Huang, Q. (2012). Effect of graphene oxide on undifferentiated and retinoic acid-differentiated SH-SY5Y cells line. Nanoscale *4*, 3861.

Maeda-Mamiya, R., Noiri, E., Isobe, H., Nakanishi, W., Okamoto, K., Doi, K., Sugaya, T., Izumi, T., Homma, T., and Nakamura, E. (2010). In vivo gene delivery by cationic tetraamino fullerene. Proc. Natl. Acad. Sci. *107*, 5339–5344.

Mahmoudifard, M., Soleimani, M., Hatamie, S., Zamanlui, S., Ranjbarvan, P., Vossoughi, M., and Hosseinzadeh, S. (2016). The different fate of satellite cells on conductive composite electrospun nanofibers with graphene and graphene oxide nanosheets. Biomed. Mater. *11*, 025006.

Maurer, N., Fenske, D.B., and Cullis, P.R. (2001). Developments in liposomal drug delivery systems. Expert Opin. Biol. Ther. *1*, 923–947.

McCool, B.A., and Farroni, J.S. (2001). A_1 adenosine receptors inhibit multiple voltage-gated Ca^{2+} channel subtypes in acutely isolated rat basolateral amygdala neurons. Br. J. Pharmacol. *132*, 879–888.

McCool, B.A., Frye, G.D., Pulido, M.D., and Botting, S.K. (2003). Effects of chronic ethanol consumption on rat GABAA and strychnine-sensitive glycine receptors expressed by lateral/basolateral amygdala neurons. Brain Res. *963*, 165–177.

McDonald, A.J. (1998). Cortical pathways to the mammalian amygdala. Prog. Neurobiol. *55*, 257–332.

Medina-Sánchez, M., Miserere, S., and Merkoçi, A. (2012). Nanomaterials and lab-on-a-chip technologies. Lab. Chip *12*, 1932.

Meis, S., and Pape, H.-C. (1997). Properties of a Ca^{2+} -Activated K^{+} Conductance in Acutely Isolated Pyramidal-Like Neurons From the Rat Basolateral Amygdaloid Complex. J. Neurophysiol. *78*, 1256–1262.

Menaa, F., Abdelghani, A., and Menaa, B. (2015). Graphene nanomaterials as biocompatible and conductive scaffolds for stem cells: impact for tissue engineering and regenerative medicine: The G point in stem cell research? J. Tissue Eng. Regen. Med. *9*, 1321–1338.

Mendonça, M.C.P., Soares, E.S., de Jesus, M.B., Ceragioli, H.J., Irazusta, S.P., Batista, Â.G., Vinolo, M.A.R., Maróstica Júnior, M.R., and da Cruz-Höfling, M.A. (2016a). Reduced graphene oxide: nanotoxicological profile in rats. J. Nanobiotechnology *14*.

Mendonça, M.C.P., Soares, E.S., de Jesus, M.B., Ceragioli, H.J., Batista, Â.G., Nyúl-Tóth, Á., Molnár, J., Wilhelm, I., Maróstica, M.R., Krizbai, I., et al. (2016b). PEGylation of Reduced Graphene Oxide Induces Toxicity in Cells of the Blood–Brain Barrier: An *in Vitro* and *in Vivo* Study. Mol. Pharm. *13*, 3913–3924.

Meyvantsson, I., and Beebe, D.J. (2008). Cell Culture Models in Microfluidic Systems. Annu. Rev. Anal. Chem. *1*, 423–449.

Mittal, S., Kumar, V., Dhiman, N., Chauhan, L.K.S., Pasricha, R., and Pandey, A.K. (2016). Physico-chemical properties based differential toxicity of graphene oxide/reduced graphene oxide in human lung cells mediated through oxidative stress. Sci. Rep. *6*.

Mochalin, V.N., Shenderova, O., Ho, D., and Gogotsi, Y. (2012). The properties and applications of nanodiamonds. Nat. Nanotechnol. *7*, 11–23.

Morris, J.S., Öhman, A., and Dolan, R.J. (1998). Conscious and unconscious emotional learning in the human amygdala. Nature *393*, 467–470.

Mundra, R.V., Wu, X., Sauer, J., Dordick, J.S., and Kane, R.S. (2014). Nanotubes in biological applications. Curr. Opin. Biotechnol. *28*, 25–32.

Navarro, X., Torres-Espín, A., Allodi, I., Santos, D., González-Pérez, F., Udina, E., del Valle, J., and Navarro, X. (2016). Analysis of axonal growth in organotypic neural cultures. Protoc. Exch.

Nel, A.E., Mädler, L., Velegol, D., Xia, T., Hoek, E.M.V., Somasundaran, P., Klaessig, F., Castranova, V., and Thompson, M. (2009). Understanding biophysicochemical interactions at the nano–bio interface. Nat. Mater. *8*, 543–557.

Nieto, A., Dua, R., Zhang, C., Boesl, B., Ramaswamy, S., and Agarwal, A. (2015). Three Dimensional Graphene Foam/Polymer Hybrid as a High Strength Biocompatible Scaffold. Adv. Funct. Mater. *25*, 3916–3924.

Novoselov, K.S. (2004). Electric Field Effect in Atomically Thin Carbon Films. Science *306*, 666–669.

Ou, L., Song, B., Liang, H., Liu, J., Feng, X., Deng, B., Sun, T., and Shao, L. (2016). Toxicity of graphene-family nanoparticles: a general review of the origins and mechanisms. Part. Fibre Toxicol. *13*.

Oyefusi, A., Olanipekun, O., Neelgund, G.M., Peterson, D., Stone, J.M., Williams, E., Carson, L., Regisford, G., and Oki, A. (2014). Hydroxyapatite grafted carbon nanotubes and graphene nanosheets: Promising bone implant materials. Spectrochim. Acta. A. Mol. Biomol. Spectrosc. *132*, 410–416.

Paek, S.-M., Yoo, E., and Honma, I. (2009). Enhanced Cyclic Performance and Lithium Storage Capacity of SnO_2 /Graphene Nanoporous Electrodes with Three-Dimensionally Delaminated Flexible Structure. Nano Lett. *9*, 72–75.

Pan, Y., Wang, L., Kang, S., Lu, Y., Yang, Z., Huynh, T., Chen, C., Zhou, R., Guo, M., and Zhao, Y. (2015). Gd–Metallofullerenol Nanomaterial Suppresses Pancreatic Cancer Metastasis by Inhibiting the Interaction of Histone Deacetylase 1 and Metastasis-Associated Protein 1. ACS Nano *9*, 6826–6836.

Pardo, B., and Honegger, P. (2000). Differentiation of rat striatal embryonic stem cells in vitro: monolayer culture vs. three-dimensional coculture with differentiated brain cells. J. Neurosci. Res. *59*, 504–512.

Paredes, J.I., Villar-Rodil, S., Martínez-Alonso, A., and Tascón, J.M.D. (2008). Graphene Oxide Dispersions in Organic Solvents. Langmuir *24*, 10560–10564.

Park, S., and Ruoff, R.S. (2009). Chemical methods for the production of graphenes. Nat. Nanotechnol. *4*, 217–224.

Patil, S., George, T., and Mahadik, K. (2015). Green synthesized nanosilver loaded silk fibroin gel for enhanced wound healing. J. Drug Deliv. Sci. Technol. *30*, 30–36.

Patra, N., Wang, B., and Král, P. (2009). Nanodroplet Activated and Guided Folding of Graphene Nanostructures. Nano Lett. *9*, 3766–3771.

Pelin, M., Fusco, L., León, V., Martín, C., Criado, A., Sosa, S., Vázquez, E., Tubaro, A., and Prato, M. (2017). Differential cytotoxic effects of graphene and graphene oxide on skin keratinocytes. Sci. Rep. *7*.

Perlmutter, J.S., and Mink, J.W. (2006). DEEP BRAIN STIMULATION. Annu. Rev. Neurosci. *29*, 229–257.

Pescatori, M., Bedognetti, D., Venturelli, E., Ménard-Moyon, C., Bernardini, C., Muresu, E., Piana, A., Maida, G., Manetti, R., Sgarrella, F., et al. (2013). Functionalized carbon nanotubes as immunomodulator systems. Biomaterials *34*, 4395–4403.

Plenz, D., and Kitai, S.T. (1996). Organotypic cortex-striatum-mesencephalon cultures: the nigrostriatal pathway. Neurosci. Lett. *209*, 177–180.

Qu, Y., He, F., Yu, C., Liang, X., Liang, D., Ma, L., Zhang, Q., Lv, J., and Wu, J. (2018). Advances on graphene-based nanomaterials for biomedical applications. Mater. Sci. Eng. C *90*, 764–780.

Rauti, R., Lozano, N., León, V., Scaini, D., Musto, M., Rago, I., Ulloa Severino, F.P., Fabbro, A., Casalis, L., Vázquez, E., et al. (2016). Graphene Oxide Nanosheets Reshape Synaptic Function in Cultured Brain Networks. ACS Nano *10*, 4459–4471.

Rauti, R., Medelin, M., Newman, L., Vranic, S., Reina, G., Bianco, A., Prato, M., Kostarelos, K., and Ballerini, L. (2019). Graphene Oxide Flakes Tune Excitatory Neurotransmission in Vivo by Targeting Hippocampal Synapses. Nano Lett. *19*, 2858–2870.

Ravikumar, M., Jain, S., Miller, R.H., Capadona, J.R., and Selkirk, S.M. (2012). An organotypic spinal cord slice culture model to quantify neurodegeneration. J. Neurosci. Methods *211*, 280–288.

Regehr, K.J., Domenech, M., Koepsel, J.T., Carver, K.C., Ellison-Zelski, S.J., Murphy, W.L., Schuler, L.A., Alarid, E.T., and Beebe, D.J. (2009). Biological implications of polydimethylsiloxane-based microfluidic cell culture. Lab. Chip *9*, 2132.

Reina, G., González-Domínguez, J.M., Criado, A., Vázquez, E., Bianco, A., and Prato, M. (2017). Promises, facts and challenges for graphene in biomedical applications. Chem. Soc. Rev. *46*, 4400–4416.

Rogan, M.T., and LeDoux, J.E. (1996). Emotion: Systems, Cells, Synaptic Plasticity. Cell *85*, 469–475.

Ruoff, R. (2008). Calling all chemists: Graphene. Nat. Nanotechnol. *3*, 10–11.

Ruoff, R.S., and Ruoff, A.L. (1991). The bulk modulus of C_{60} molecules and crystals: A molecular mechanics approach. Appl. Phys. Lett. *59*, 1553–1555.

Russell-Jones, G. (1999). Vitamin B12-mediated transport of nanoparticles across Caco-2 cells. Int. J. Pharm. *179*, 247–255.

Sacchetti, C., Liu-Bryan, R., Magrini, A., Rosato, N., Bottini, N., and Bottini, M. (2014). Polyethylene-Glycol-Modified Single-Walled Carbon Nanotubes for Intra-Articular Delivery to Chondrocytes. ACS Nano *8*, 12280–12291.

Sah, P., Faber, E.S.L., Lopez De Armentia, M., and Power, J. (2003). The Amygdaloid Complex: Anatomy and Physiology. Physiol. Rev. *83*, 803–834.

Sanchez, V.C., Jachak, A., Hurt, R.H., and Kane, A.B. (2012). Biological Interactions of Graphene-Family Nanomaterials: An Interdisciplinary Review. Chem. Res. Toxicol. *25*, 15–34.

Sayyar, S., Bjorninen, M., Haimi, S., Miettinen, S., Gilmore, K., Grijpma, D., and Wallace, G. (2016). UV Cross-Linkable Graphene/Poly(trimethylene Carbonate) Composites for 3D Printing of Electrically Conductive Scaffolds. ACS Appl. Mater. Interfaces *8*, 31916–31925.

Scott, S.K., Young, A.W., Calder, A.J., Hellawell, D.J., Aggleton, J.P., and Johnsons, M. (1997). Impaired auditory recognition of fear and anger following bilateral amygdala lesions. Nature *385*, 254–257.

Seabra, A.B., Paula, A.J., de Lima, R., Alves, O.L., and Durán, N. (2014). Nanotoxicity of Graphene and Graphene Oxide. Chem. Res. Toxicol. *27*, 159–168.

Serrano, M.C., Patiño, J., García-Rama, C., Ferrer, M.L., Fierro, J.L.G., Tamayo, A., Collazos-Castro, J.E., del Monte, F., and Gutiérrez, M.C. (2014). 3D free-standing porous scaffolds made of graphene oxide as substrates for neural cell growth. J. Mater. Chem. B *2*, 5698.

Shao, W.Z., Ivanov, V.V., Zhen, L., Cui, Y.S., and Wang, Y. (2004). A study on graphitization of diamond in copper–diamond composite materials. Mater. Lett. *58*, 146–149.

Shi, J., Wang, L., Gao, J., Liu, Y., Zhang, J., Ma, R., Liu, R., and Zhang, Z. (2014). A fullerene-based multi-functional nanoplatform for cancer theranostic applications. Biomaterials *35*, 5771–5784.

Shin, H., Jo, S., and Mikos, A.G. (2003). Biomimetic materials for tissue engineering. Biomaterials *24*, 4353–4364.

Si, Y., and Samulski, E.T. (2008). Synthesis of Water Soluble Graphene. Nano Lett. *8*, 1679–1682.

Silva, G.A. (2006). Neuroscience nanotechnology: progress, opportunities and challenges. Nat. Rev. Neurosci. *7*, 65–74.

Simões, M.C.F., Sousa, J.J.S., and Pais, A.A.C.C. (2015). Skin cancer and new treatment perspectives: A review. Cancer Lett. *357*, 8–42.

Sinitskii, A., and Tour, J.M. (2010). Graphene Electronics, Unzipped. IEEE Spectr. *47*, 28–33.

Solanki, A., Chueng, S.-T.D., Yin, P.T., Kappera, R., Chhowalla, M., and Lee, K.-B. (2013). Axonal Alignment and Enhanced Neuronal Differentiation of Neural Stem Cells on Graphene-Nanoparticle Hybrid Structures. Adv. Mater. *25*, 5477–5482.

Spelman, F.A. (2006). Cochlear Electrode Arrays: Past, Present and Future. Audiol. Neurotol. *11*, 77–85.

Stankovich, S., Dikin, D.A., Dommett, G.H.B., Kohlhaas, K.M., Zimney, E.J., Stach, E.A., Piner, R.D., Nguyen, S.T., and Ruoff, R.S. (2006). Graphene-based composite materials. Nature *442*, 282–286.

Stankovich, S., Dikin, D.A., Piner, R.D., Kohlhaas, K.A., Kleinhammes, A., Jia, Y., Wu, Y., Nguyen, S.T., and Ruoff, R.S. (2007). Synthesis of graphene-based nanosheets via chemical reduction of exfoliated graphite oxide. Carbon *45*, 1558–1565.

Strauss, V., Margraf, J.T., Dolle, C., Butz, B., Nacken, T.J., Walter, J., Bauer, W., Peukert, W., Spiecker, E., Clark, T., et al. (2014). Carbon Nanodots: Toward a Comprehensive Understanding of Their Photoluminescence. J. Am. Chem. Soc. *136*, 17308–17316.

Su, F.-Y., You, C., He, Y.-B., Lv, W., Cui, W., Jin, F., Li, B., Yang, Q.-H., and Kang, F. (2010). Flexible and planar graphene conductive additives for lithium-ion batteries. J. Mater. Chem. *20*, 9644.

Sun, X., Liu, Z., Welsher, K., Robinson, J.T., Goodwin, A., Zaric, S., and Dai, H. (2008). Nano-graphene oxide for cellular imaging and drug delivery. Nano Res. *1*, 203–212.

Thalhammer, A., Edgington, R.J., Cingolani, L.A., Schoepfer, R., and Jackman, R.B. (2010). The use of nanodiamond monolayer coatings to promote the formation of functional neuronal networks. Biomaterials *31*, 2097–2104.

Thompson, B.C., and Fréchet, J.M.J. (2008). Polymer–Fullerene Composite Solar Cells. Angew. Chem. Int. Ed. *47*, 58–77.

Thostenson, E.T., Ren, Z., and Chou, T.-W. (2001). Advances in the science and technology of carbon nanotubes and their composites: a review. Compos. Sci. Technol. *61*, 1899–1912.

Tonelli, F.M., Goulart, V.A., Gomes, K.N., Ladeira, M.S., Santos, A.K., Lorençon, E., Ladeira, L.O., and Resende, R.R. (2015). Graphene-based nanomaterials: biological and medical applications and toxicity. Nanomed. *10*, 2423–2450.

Tovote, P., Fadok, J.P., and Lüthi, A. (2015). Neuronal circuits for fear and anxiety. Nat. Rev. Neurosci. *16*, 317–331.

Tu, Q., Pang, L., Chen, Y., Zhang, Y., Zhang, R., Lu, B., and Wang, J. (2014). Effects of surface charges of graphene oxide on neuronal outgrowth and branching. The Analyst *139*, 105–115.

Ulloa Severino, F.P., Ban, J., Song, Q., Tang, M., Bianconi, G., Cheng, G., and Torre, V. (2016). The role of dimensionality in neuronal network dynamics. Sci. Rep. *6*.

Usmani, S., Aurand, E.R., Medelin, M., Fabbro, A., Scaini, D., Laishram, J., Rosselli, F.B., Ansuini, A., Zoccolan, D., Scarselli, M., et al. (2016). 3D meshes of carbon nanotubes guide functional reconnection of segregated spinal explants. Sci. Adv. *2*, e1600087.

Veloz-Castillo, M., West, R., Cordero-Arreola, J., Arias-Carrión, O., and Méndez-Rojas, M. (2016). Nanomaterials for Neurology: State-of-the-Art. CNS Neurol. Disord. - Drug Targets *15*, 1306–1324.

Vinogradov, S.V., Batrakova, E.V., and Kabanov, A.V. (2004). Nanogels for Oligonucleotide Delivery to the Brain. Bioconjug. Chem. *15*, 50–60.

Wang, Z., and Dai, Z. (2015). Carbon nanomaterial-based electrochemical biosensors: an overview. Nanoscale *7*, 6420–6431.

Wang, S., Ang, P.K., Wang, Z., Tang, A.L.L., Thong, J.T.L., and Loh, K.P. (2010). High Mobility, Printable, and Solution-Processed Graphene Electronics. Nano Lett. *10*, 92–98.

Wang, Z., Li, P., Chen, Y., He, J., Zhang, W., Schmidt, O.G., and Li, Y. (2014). Pure thiophene–sulfur doped reduced graphene oxide: synthesis, structure, and electrical properties. Nanoscale *6*, 7281.

Whitener, K.E., and Sheehan, P.E. (2014). Graphene synthesis. Diam. Relat. Mater. *46*, 25–34.

Wierońska, J., Stachowicz, K., Nowak, G., and Pilc, A. (2011). The Loss of Glutamate-GABA Harmony in Anxiety Disorders. In Anxiety Disorders, V. Kalinin, ed. (InTech), p.

Xu, X., Ray, R., Gu, Y., Ploehn, H.J., Gearheart, L., Raker, K., and Scrivens, W.A. (2004). Electrophoretic Analysis and Purification of Fluorescent Single-Walled Carbon Nanotube Fragments. J. Am. Chem. Soc. *126*, 12736–12737.

Xu, X., Wang, J., Wang, Y., Zhao, L., Li, Y., and Liu, C. (2018). Formation of graphene oxide-hybridized nanogels for combinative anticancer therapy. Nanomedicine Nanotechnol. Biol. Med. *14*, 2387–2395.

Yang, H.-W., Huang, C.-Y., Lin, C.-W., Liu, H.-L., Huang, C.-W., Liao, S.-S., Chen, P.-Y., Lu, Y.-J., Wei, K.-C., and Ma, C.-C.M. (2014). Gadolinium-functionalized nanographene oxide for combined drug and microRNA delivery and magnetic resonance imaging. Biomaterials *35*, 6534–6542.

Yang, K., Feng, L., Shi, X., and Liu, Z. (2013a). Nano-graphene in biomedicine: theranostic applications. Chem Soc Rev *42*, 530–547.

Yang, M., Flavin, K., Kopf, I., Radics, G., Hearnden, C.H.A., McManus, G.J., Moran, B., Villalta-Cerdas, A., Echegoyen, L.A., Giordani, S., et al. (2013b). Functionalization of Carbon Nanoparticles Modulates Inflammatory Cell Recruitment and NLRP3 Inflammasome Activation. Small *9*, 4194–4206.

Yano, S., Miwa, S., Mii, S., Hiroshima, Y., Uehara, F., Kishimoto, H., Tazawa, H., Zhao, M., Bouvet, M., Fujiwara, T., et al. (2015). Cancer cells mimic *in vivo* spatial-temporal cell-cycle phase distribution and chemosensitivity in 3-dimensional Gelfoam® histoculture but not 2-dimensional culture as visualized with real-time FUCCI imaging. Cell Cycle *14*, 808–819.

Yeap, W.S., Tan, Y.Y., and Loh, K.P. (2008). Using Detonation Nanodiamond for the Specific Capture of Glycoproteins. Anal. Chem. *80*, 4659–4665.

Yeon, J.H., and Park, J.-K. (2007). Microfluidic Cell Culture Systems for Cellular Analysis. BIOCHIP J. *1*, 17–27.

Zhang, H., Li, J., and Zhang, B. (2007). Microstructure and electrical properties of porous PZT ceramics derived from different pore-forming agents. Acta Mater. *55*, 171–181.

Zhang, H., Grüner, G., and Zhao, Y. (2013). Recent advancements of graphene in biomedicine. J. Mater. Chem. B *1*, 2542.

Zhang, J., Yang, H., Shen, G., Cheng, P., Zhang, J., and Guo, S. (2010). Reduction of graphene oxide via L -ascorbic acid. Chem Commun *46*, 1112–1114.

Zhang, Y., Rhee, K.Y., Hui, D., and Park, S.-J. (2018). A critical review of nanodiamond based nanocomposites: Synthesis, properties and applications. Compos. Part B Eng. *143*, 19–27.

Zhao, A., Chen, Z., Zhao, C., Gao, N., Ren, J., and Qu, X. (2015). Recent advances in bioapplications of C-dots. Carbon *85*, 309–327.

Zhou, J., Khodakov, D.A., Ellis, A.V., and Voelcker, N.H. (2012). Surface modification for PDMS-based microfluidic devices. ELECTROPHORESIS *33*, 89–104.